Synthesis of biphasic Al/Al_2O_3 nanostructures under microgravity and laser structuring on Al/Al_2O_3 surfaces for selective cell guidance

Dissertation

zur Erlangung des Grades des Doktors der Ingenieurwissenschaften
der Naturwissenschaftlich-Technischen Fakultät III
Chemie, Pharmazie, Bio-und Werkstoffwissenschaften
der Universität des Saarlandes

von

Juseok Lee

Saarbrücken, Germany

2013

Tag des Kolloquiums:	30. 07. 2013
Dekan:	Prof. Dr. Volkhard Helms
Vorsitz:	Prof. Dr. Guido Kickelbick
Berichterstatter:	Prof. Dr. Dr. h.c. Michael Veith
	Prof. Dr. Albrecht Ott
Akad. Mitarbeiter:	Dr. Isabella Gallino-Busch

Abstract

The first part of this thesis is dealing with gravity effect on the synthesis of biphasic core/shell Al/Al_2O_3 composites. By chemical vapor deposition of the precursor $[^tBuOAlH_2]_2$ at 400°C, only spherical nanoparticles were observed on the substrate surface. The formation of nanowires was observed at 600°C. It is a good agreement with our previous results on earth condition and there is no gravity impact on the chemical reaction. At increased gravity levels, the nanoparticles formed large clusters and the nanowires showed bundle formation while the nanowires at microgravity have predominantly linear structures. It is proposed that the chaotic nature of nanowires and cluster formation of nanoparticles were caused by a dominance of gravity over the thermal creep.

In the second part the use of Al/Al_2O_3 nanowire layers for bio applications is considered. Contact cell guidance and alignment were studied to understand how cells recognize and respond to certain surface patterns. Linear micro channels were created on Al/Al_2O_3 layer by direct laser writing and laser interference patterning. Although surface topography was altered, the surface chemistry was always identical (Al_2O_3) due to the unique core/shell nature of Al/Al_2O_3 nanowires. Human osteoblast, normal human dermal fibroblast and neuronal cells were cultured and investigated. The results indicate that different cell types show diverse responses to the topography independent from the surface chemistry of the material.

Zusammenfassung

Der erste Teil dieser Dissertation behandelt die Wirkung der Schwerkraft auf die Herstellung biphasischer Kern-Hülle Al/Al_2O_3 Verbundwerkstoffen. Bei der chemischen Gasphasenabscheidung des Präkursor $[^tBuOAlH_2]_2$ wurden bei 400° C nur sphärische Nanopartikel auf der Substratoberfläche beobachtet. Bei 600° C wurde die Bildung von Nanodrähten beobachtet. Dies bestätigt unsere früheren Ergebnisse. Bei erhöhter Schwerkraft bildeten die Nanopartikel große Cluster und die Nanodrähte formten Bündel. In Schwerelosigkeit wiesen die Nanodrähte meist lineare Strukturen auf. Eine mögliche Erklärung für das chaotische Verhalten der Nanodrähte und das Formen der Cluster könnte eine Dominanz der Schwerkraft gegenüber dem thermischen Kriechen sein.

Der zweite Teil behandelt die Verwendung der Al/Al_2O_3- Nanodrähte als Beschichtungen für Bioanwendungen. Das gerichtete Wachstum von Zellen wurde untersucht um zu verstehen wie Zellen verschiedene Strukturen erkennen und darauf reagieren. Dazu wurden Kanäle auf den Beschichtungen durch direktes Laserschreiben und Laserinterferenzstrukturieren erzeugt. Dabei wurde nur die Topografie verändert. Die Oberflächenchemie (Al_2O_3) blieb durch den einzigartigen Kern-Hülle Charakter der Beschichtung immer identisch. Menschliche Osteoblast-, Fibroblast- und Nervenzellen wurden kultiviert und untersucht. Die Ergebnisse zeigen, dass bei gleichbleibender Oberflächenchemie die Zellantwort verschiedener Zelltypen unterschiedlich von der Topografie abhängig ist.

Acknowledgements

Firstly, my deep and sincere gratitude go to my supervisor, Professor Dr. Dr. h. c. Michael Veith, Scientific Director of Leibniz-Institute for New Materials, Professor of Inorganic and General Chemistry of Saarland University, for his unlimited supports and for offering me the opportunities in his group for special projects.

My sincere appreciations go to Professor Dr. med. Karl-Herbert Schäfer and Lukas K. Schwarz who are in the Biotechnology department of University of Applied Sciences in Zweibrücken. I would like also to thank to Dr. Wolfgang Metzger and Prof. Dr. Tim Pohlemann in the department of Trauma-, Hand- and Reconstructive Surgery of the University Hospital of Saarland. Their extensive discussions, fruitful advice and kind help in biological experiments around my work have been especially supportive for this study.

I wish to extend my warmest thanks to Dr. Vladimir Zaporojtchenko, Department of Multicomponentmaterials, Kiel University, for the XPS analysis in this study. He passed away before our publication appears. I will remember our collaboration.

I have received many support and help during my stay in the CVD/Biosurfaces group of INM. Dr. Cenk Aktas, head of the group, has assisted me in numerous ways giving many industrial and academic projects. I would like to thank to Dr. Marina Martinez Miró, Cagri Kaan Akkan, Alexander May, Ayman Haidar, Dr. Karin Löw, Dr. Tatjana Kirs, Dieter Anschütz, Stefan Brück, Fadime Sahin and other colleagues in the institute.

My special thanks go to my family in Korea.

To my wife, Hyeyoung Han and my daughter, Hanna Lee.

Table of contents

Abbreviation

1D	one dimensional
AFM	atomic force microscopy
Al/Al_2O_3	aluminium-aluminium oxide composite
CVD	chemical vapor deposition
CW	continuous wave
DRG	dorsal root ganglia
ECM	extra cellular matrix
FIB	focused ion beam
HAZ	heat affected zone
HOB	human osteoblast
IR	infrared
LASER	light amplification by stimulated emission of radiation
LIP	laser interference patterning
MOCVD	metal-organic chemical vapor deposition
Nd:YAG	neodymium-doped yttrium aluminum garnet
NHDF	normal human dermal fibroblast
NIR	near infrared
OAG	oxide assisted growth
PACVD	plasma assisted chemical vapor deposition
PBS	phosphate buffered saline
PECVD	plasma enhanced chemical vapor deposition
PVD	physical vapor deposition
SEM	scanning electron microscopy
SHG	second harmonic generation

SSP	single source precursor
TEM	transmission electron microscopy
THG	third harmonic generation
UV	ultraviolet
VIS	visible
VLS	vapor-liquid-solid
XPS	X-ray photoelectron spectroscopy
XRD	X-ray diffraction

Introduction

Nanowires formed by vapor-liquid-solid (VLS) mechanism have become promising building components for nanodevice applications due to their extraordinary physical properties. The VLS process is one of the growth methods to fabricate various one dimensional (1D) nanostructures from vapor phase [1]. In a typical VLS process, the whole growth process can be described by three steps. First, nanoparticles act as catalysts which absorb reactants from gas phase precursor and then eutectic alloy droplets are formed. Finally 1D structures such nanowires or whiskers can grow through the liquid droplets due to supersaturation [1-3]. Such method allows controlling the length of the wires by varying the growth duration while the nanowire diameter can be controlled by the size of the catalyst droplet and the growth rate can be measured as a function of a driving force and supersaturation [4].

There are also attempts to synthesize nanowires without using any external catalyst particle which is a challenge for coating of large area substrates and for precise controlling of the impurity level [5]. In such an approach, first the gaseous source condensates on the heated substrate and forms nanoscale droplets. Then these droplets act as seeds itself for the one-dimensional growth. In contrast to VLS, the control of the size and morphology is more complicated in catalyst-free synthesis method. In addition to surface properties of the substrate, also the transport process itself becomes a critical parameter in the growth mechanism. Beside of conventional parameters such as temperature and pressure, the effect of the gravitation on the gas transport in a classical chemical vapor deposition (CVD) process has been already addressed [6, 7]. A final issue concerns the use of microgravity experiments to enhance understanding of CVD processes. Experiments of under microgravity conditions can be used to test the predictions of models [7].

Since CVD of single source precursor (SSP) "$[^{t}BuOAlH_2]_2$" has been developed by Prof. Michael Veith [8], many detailed studies have been carried out to be applied in various fields. Especially, the synthesis of Al/Al_2O_3 core-shell nanowires without the use of any additional catalyst was presented [9]. This approach is based on the formation of a globular seed particle prior to a subsequent 1D growth of wires similar to VLS mechanism. By using so called single source precursors (SSPs), the generation of such materials can be simplified in such a way that the desired material

is forming as the sole product in a chemical cascade reaction. This has the advantage, besides others, to occur within short lapses of time (generally seconds) as the process is related to a fast molecular reaction. In addition, the unique ease and remarkable speed of the reaction of $[^{t}BuOAlH_2]_2$ seemed an excellent prerequisite to conduct microgravity experiments. Here the direct effect of the gravity on catalyst-free synthesis of nanostructures under microgravity environment is reported for the first time using a new experimental set-up.

The uses of nanowires are not limited to use only electronic device applications. For example, TiO_2 nanowires improved adhesion of muscle tissue while it does not adhere well to bulk titanium surfaces because the tissue can anchor itself to the TiO_2 nanowires coated implant [10]. It can reduce the failure and risk of implants such as stents and orthopedic implants. Furthermore Si nanowires affect the stem cell differentiation by a stimulation of electric current [11]. Those researches give an idea to use of nanowires in the field of biological applications. However, so far only a few materials were introduced for use of implant materials, because implant material in the living systems should be biocompatible or non-toxic. In this regard, Alumina is a good candidate as an implant material because of its excellent biocompatibility and inertness. Thus high corrosion resistance, strength and wear resistance of alumina allow it to be used in cardiovascular, orthopedic, dental and maxillofacial prosthetics implants as a bulk form or a coating for tissue ingrowths [12]. In other words, the design of surfaces of biomaterials is important for tissue engineering because surface modification provide direct interactions between living systems and implanted materials.

There were extensive research efforts to investigate the topographic effect of biomaterials with various micro- and nano-structures on cell-material interactions [13-15]. The fabrication of nanostructures on biomaterials improves their biocompatibility effectively with well-defined morphologies [16-19]. As reported that linear groove patterns led to an increase in endothelial cell and osteoblast adhesions and fibroblasts exhibited enhanced contact guidance and filopodia extension on grooved nanostructures [13, 20]. Despite several top-down and bottom-up methods have been used to fabricate various surface patterns, structuring of surfaces by lasers is one of the most preferred methods to pattern biomaterials because of its versatility and a non-contact processing nature. Especially nanogrooves and nanogratings are commonly employed nanotopographical elements for exploring cell surface

interactions. Simply a laser beam can be focused on any substrate to create lines or holes directly onto the surface so called direct laser writing. On the other hand, laser interference patterning (LIP) is another straightforward and efficient method to prepare nano- and micro-scale patterns. This method is based on the selective modification of surfaces by mixing two or more laser beams to superimpose and form an interference pattern [21-23]. Although, cell guidance on laser structured surfaces is not a new finding, it is still an open question whether the cell behavior is influenced by the surface chemistry or topography or both.

Given that alumina is well established material for dental and orthopedic implant due to its biocompatibility, it can be good approaches to control the different morphologies of these materials to study the behavior of various cell types. First cell studies on Al/Al_2O_3 nanowires were carried out by Petersen [24, 25] and later on by Aktas [26, 27] who studied cell surface interaction by altering the surface topography using pulsed laser in the research group of Prof. Veith, following studies which have been introduced mostly concerning the surface topography change while keeping the surface chemistry [25, 27-32]. In addition Al_2O_3 is known as a biocompatible material and has been used in many implant applications. Previously Veith et al. [25] showed that the fibroblast adhesion is reduced on Al/Al_2O_3 composite nanowires, while osteoblast adhesion increases on the same surface. This indicates clearly that different cell types show diverse responses to the topography independent from the surface chemistry. Conversely pulsed laser treated Al/Al_2O_3 nanowires showed better adhesion of fibroblasts [27]. As shown there the effect of the topography (with the constant surface chemistry) was predominant for the cell adhesion and proliferation. On the other hand in some applications such as targeted reinnervation, a directional growth of cells is also desired in addition to improved adhesion and proliferation even cell differentiation. For instance studying neuron cell guidance on nanostructured alumina surfaces can be interesting since up to date mostly fibroblast (tissue cells) and osteoblast (bone cells) adhesion on nanostructured alumina surfaces have been reported.

Applications of these works could influence investigations of neural regeneration, where cellular and matrix alignment is important. Given that cell-material interactions are very important factors to be considered for the tissue engineering. In this context, methods for creating nano/micro structures by direct laser writing (DLW) and laser interference patterning (LIP) and applications related to cell contact guidance and

control of cell alignment are introduced with a wide range of cell types because cell alignment and cell migration are direct indicators of cell-topography interaction [33]. Human Osteoblast (HOB), Normal Human Dermal Fibroblast (NHDF), neuronal cells (Dorsal root ganglion and PC12) are cultured and investigated for cell behavior upon the surface properties.

PART 1: Synthesis of Al/Al_2O_3 nanostructures under microgravity

Parabolic flight was originally started mostly to train pilots for military purposes in zero gravity. Today, the technique is mainly used to carry out experiments in weightless conditions and to test space technologies. Time and place limitations in parabolic flights prevented until now to perform gas phase deposition experiments in microgravity environment. Although some studies showed the effect of the gravity on deposition dynamics these models are mostly based on unjustified assumptions as a consequence of insufficient fundamental knowledge about the complex physicochemical interactions involved within a CVD process [7, 34, 35]. This complexity increases especially in the case of nanomaterial synthesis by CVD. The object of this present work is to understand the formation of Al/Al_2O_3 nanocomposite under gravity variation for the first time. The nanostructures of Al/Al_2O_3 were synthesized by the chemical vapor deposition (CVD) using the single source precursor, $[^tBuOAlH_2]_2$ in a newly designed CVD system. This work was successfully carried out by collaboration with **Leibniz-Institute for New Materials** (*CVD/Biosurfaces group and workshop*), **the research group of Prof. Michael Veith** (*Inorganic chemistry, University of Saarland*), **DLR** (*Deutsches Zentrum für Luft- und Raumfahrt / German Aerospace Agency*) and **NoveSpace** (*French Microgravity Aviation Company*).

1. State of the art

One dimensional (1D) nanostructures has high aspect ratio with different forms of its morphologies, such as wires, rods, fibers, tubes and belts in nanoscale [36]. For the use of those products, they should have a stable dispersion of the units or structures with controlled size and physico-chemical properties [37]. So far various innovative top-down and bottom-up fabrication methods are introduced to synthesize various nanostructures such as thin film deposition and self-assembly processes, electrospinning, phase separation, nano-imprinting, photolithography, and electron beam etc. [37, 38]. Among them CVD is mostly used method to product thin films and 1D nanostructures of various materials.

1D nanostructures can be grown by self-assembling of nanotubes or nanofibers mimicking some natural entities similar to collagen fibers [39]. Of course 1D nanostructures also can be directly fabricated by advanced nanolithography processes as physical patterning techniques with well ordered features however gas phase techniques are more efficient and adaptable for the synthesis of 1D nanostructures in large quantities. The CVD process is one of the basic production method in the semiconductor industry for the production of functional thin films to be used for various applications of nanoelectronic devices including integrated circuits, solar cells, liquid crystal displays etc. [40]. The majority of CVD applications involve applying solid thin film coatings on the surfaces, but it is used also to produce high purity bulk materials and powders, as well as to fabricate composites. CVD coatings can be applied to elaborately shaped pieces, including the insides and undersides of features, and high aspect ratio holes and other features can be completely filled with relatively high deposition rates.

Indeed the basic concept of CVD is quite simple as shown the mechanism of a CVD process and reaction steps in Figure 1-1. CVD involves volatile precursor which forms a gas phase at room temperature in a common CVD process. The source species of the precursor are transported into the reaction chamber under vacuum. They pass over or come to the hot surfaces by diffusion and convection while they are simultaneously heated. The source species will react or decompose forming solid phase on the heated substrates. Usually both gas and surface chemical reactions occur, depending on the prevailing heat and mass transport and on the chemical kinetic parameters during operation. Thus the substrate temperature is significant

and highly influence to the reactions between precursor gases and substrate surface. The substrate can be exposed not only to single precursor but also more volatile precursors in order to produce multi-component materials. Finally, volatile by-products from the chemical reactions are removed from the reaction chamber following the gas flow induced by a vacuum pump.

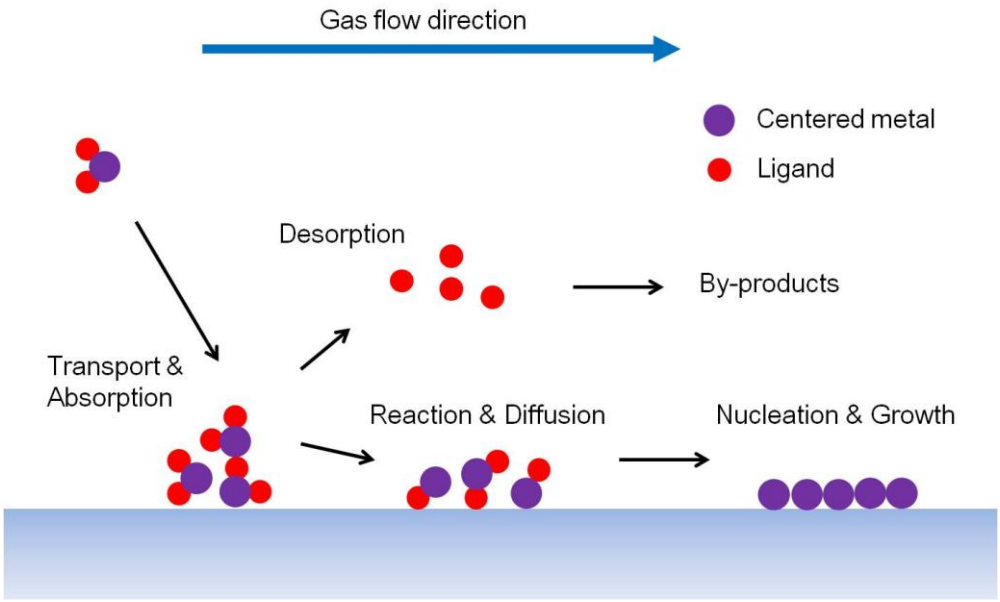

Figure 1-1. Schematic diagram of CVD mechanism

Although the basic concept of CVD is quite simple, it is a quite complex process which has many factors affecting the deposition of coatings for instance type, shape, and size of reaction chamber, precursor gas flow rate, temperature and arrangement of the substrate. Therefore in order to satisfy the desired coatings, a number of forms of CVD are in wide used and frequently referenced in the literature [41]. These processes differ in the means by which chemical reactions are initiated and process conditions such as: Atmospheric pressure chemical vapor deposition (APCVD), Low pressure chemical vapor deposition (LPCVD), Ultrahigh vacuum chemical vapor deposition (UHVCVD), Plasma assisted or enhanced chemical vapor deposition (PACVD, PECVD), Direct liquid injection chemical vapor deposition (DLICVD), Laser assisted chemical vapor deposition (LACVD), Aerosol assisted chemical vapor deposition (AACVD) and Metal-organic chemical vapor deposition (MOCVD).

1.1 Synthetical methods for the production of nanowires by CVD

Among the many of synthetic methods to fabricate functional nanowires, CVD is accepted as one of the proper bottom-up approaches. The syntheses of nanowires from CVD process are based on the processes where solids form out of catalyst seeds so called vapor-liquid-solid (VLS) mechanism which was introduced in 1964 by Wagner et al. [1]. They applied gold nanoparticles as catalyst seeds to grow one dimensional (1D) Si structures. In a typical VLS process, a liquid catalyst (generally novel materials) acts as a preferential adsorption site of the gaseous precursor and the nanowire is formed by precipitation from the catalyst droplet due to supersaturation [2]. Thus the synthesis of 1D nanostructures is depend on the formation of catalyst droplets and the existence of a eutectic point between the vapor source and the catalyst in the corresponding phase diagram. Such methods allow controlling the length of the wires by varying the growth duration while the nanowire diameter can be controlled by the size of the catalyst droplet [4]. However, it is difficult to grow nanowires in bulk-quantity and catalyst particles stay as impurities in catalyst assisted VLS processes [5]. Thus catalyst-free method may be considered as a more useful method to produce high purity 1D nanostructures.

Previously, a synthesis of Si nanowires was introduced by using powder of Si and its oxide as vapor sources [42] and simillary alumina nanowires were synthesized on a large area silicon substrate by thermal evaporation of mixture of Al and Al_2O_3 powders [43]. In both cases, no additional external catalyst was applied and these approaches are similar to the oxide assisted growth mechanism [42]. In contrast to their reports, Sow [44], in the research group of Prof. Veith, fabricated Al/Al_2O_3 nanowires using a single source molecular precursor concept without any foreign external catalyst. Different from the classical VLS methods, Al/Al_2O_3 nanowires were grown as catalyst free mechanism while the molecular precursor $[^tBuOAlH_2]_2$ was decomposed on heated substrates. In this process, Al particle may form as a seed during the first absorption of the precursor molecule on the heated substrate because the deposition temperature was lower than the melting point of Al_2O_3 but near to the melting temperature of Al. Thus only the Al particle may stay as a molten form. Sow [44] suggested that Al nanoparticles may work as a self catalyst which can be a driving force to the directional growth of Al/Al_2O_3 core/shell nanowires similar to conventional

VLS process. After the observation of branched nanowires formation by Aktas [26], this proposed concept was accepted. He explained that Al in the Al/Al_2O_3 core/shell nanowires may act as an active catalyst for the new nanowires formation. Although the CVD of the molecular precursor $[^tBuOAlH_2]_2$ is an effective method to synthesize of Al/Al_2O_3 nanostructures and it provides always reproducible results, the growth mechanism is still unclear.

1.2 A single source precursor: $[^tBuOAlH_2]_2$

A single source precursor (SSP) is usually a molecular compound which contains all the necessary elements of the final product in a well defined molecule. Disproportionations of metastable oxidation states of metallic elements may lead to metal/metal oxide composites or thermodynamics may be used to create a composite of two different metal oxide phases [45, 46]. Also intermediates formed in the thermal decomposition processes of precursors may reenter the cascades of reactions leading to alloys in metal oxide matrices. Although the compound tert-butoxyalane $[^tBuOAlH_2]_2$ was synthesized in 1968 [47] the crystal structure was discovered in 1996 by Veith et al. [8]. Almost 2 decades the investigations of precursor $[^tBuAlOH_2]_2$ have been made through the CVD process and further studies have been carried out by Prof. M. Veith and his co-workers. The molecular structure of $[^tBuOAlH_2]_2$ is illustrated in Figure 1-2.

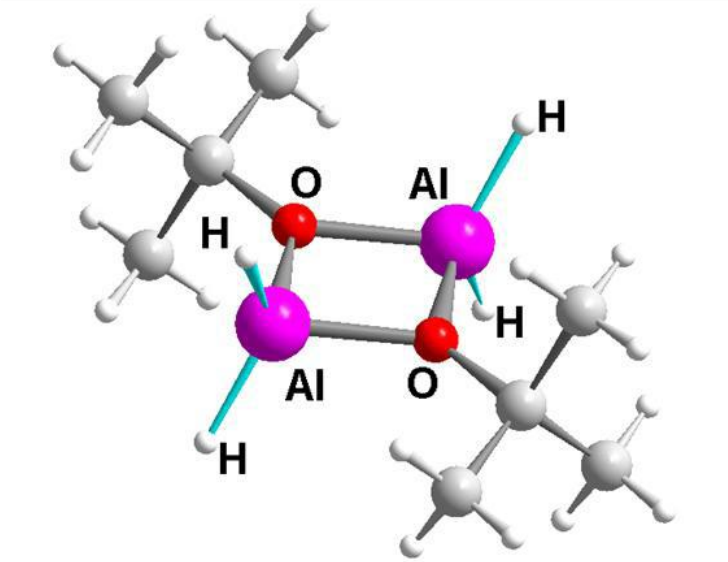

Figure 1-2. The molecule structure of $[^{t}BuOAlH_2]_2$.

As described previously, the precursor is highly volatile and thermodynamically stable in gas phase. The molecule bonding has predetermined breaking and recombination points thus the decomposition takes place via intra-molecule cascade reaction, because both gas phase byproducts isobutene and hydrogen are directly dependent from one another [8, 48]. Depending on the temperature, two different composites are deposited on the substrate. At a substrate temperature above 350 °C the gray-black coating appears and below that temperature the metastable aluminumoxidehydride (HAlO)n is deposited. According to the mass spectra, the decomposition process of $[^{t}BuOAlH_2]_2$ is described in following equations (eq. (1), (2) and (3)). In the equation (1), Al/Al_2O_3 is the product which have a shape of nanoballs around 450 °C and nanowires above 550 °C, respectively [9, 44, 46]. HAlO layer can be transformed to biphasic aluminium/aluminumoxide composite with tempering in a furnace under vacuum or laser treatment in air [49-51]. During those processes, hydrogen is eliminated (degassing) from HAlO layer at high temperatures and {AlO} (with formal Al^{2+}) intermediately disproportionate to Al^0 and Al^{3+}, forming Al/Al_2O_3 as described in the equation (3-1 and 3-2).

Depending on the substrate temperature, thermal decomposition of $[^tBuOAlH_2]_2$ is described in below [9, 49, 50] :

At 370~600°C:

$[^tBuOAlH_2]_2 \rightarrow 2(CH_3)_2C=CH_2 + 3H_2 + 2/3\ Al/Al_2O_3$ (1)

At 290~330°C:

$[^tBuOAlH_2]_2 \rightarrow 2H_2 + 2H_2C=C(CH_3)_2 + 2HAlO$ (2)

And annealing the HAlO layer above 500°C [49]:

$HAlO \rightarrow 1/2\ H_2 + \{AlO\}$ (3-1)

$\{AlO\} \rightarrow 1/3\ Al + 1/3\ Al_2O_3$ (3-2)

1.3 Synthesis of Al/Al_2O_3 nanowires by CVD of SSP $[^tBuOAlH_2]_2$

In general, substrates are cleaned carefully with isopropyl alcohol and dried at 150 °C to remove any residue. Following the cleaning procedure the substrates are placed on a sample holder within a vertical vacuum chamber. CVD system is shown in Figure 1-3. Sample holder (susceptor) was made of graphite (80 mm in diameter). Before the CVD process, reaction chamber is evacuated more than 30 minutes until the vacuum reaches $1x10^{-3}$ mbar, then flushed with N_2 gas and evacuated again. Afterwards the substrates are heated up to the required temperature in a range of 600-630 °C. High frequency generator is used to heat the graphite susceptor. The gas phase precursor is flowed into the reaction chamber after the substrate temperature is stable and constant. The precursor flow is controlled manually by a hand-valve while keeping the eye on the sensitive pressure sensor. The pressure of the chamber is kept at $8x10^{-2}$ mbar during the deposition by gradually opening the hand-valve. After the deposition process, firstly precursor flow is ended by closing the valve and heating of substrates is stopped. Then substrates are cooled down to room temperature in the reaction chamber under vacuum to avoid thermal shock which might occur due to the difference of thermal conductivity between substrate and surface layer. After cooling the deposited substrates are retrieved.

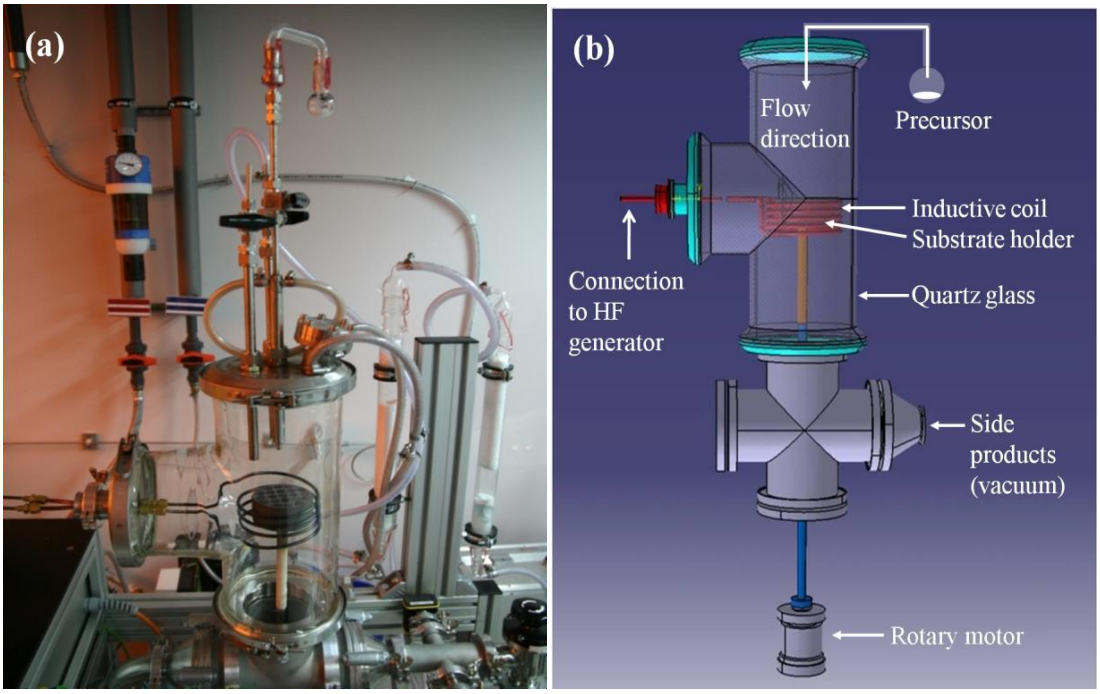

Figure 1-3. Conventional vertical cold wall CVD apparatus; (a) over view and (b) illustration of set up [28]

1.4 One-dimensional (1D) growth by self catalyst process

Contrast to Au assisted Si nanowires [52], as-deposited Al/Al_2O_3 nanowires show chaotic nature (Figure 1-4). A possible growing mechanism was proposed by Sow [44] in her thesis as shown in Figure 1-5. She estimated that aluminium particles form on the heated substrate during the absorption of the precursor molecule and they work as a catalyst. First aluminium nanoclusters form on the surface as the seeds then {AlO} accumulate in the Al droplets and Al-Al-O alloy is formed. Subsequently {AlO} nanowires are grown by precipitation of supersaturated {AlO} like in VLS process. Finally Al segregates inside of the nanowires while the Al_2O_3 shell is formed. However, the formation of aluminium clsturs was not deeply discussed.

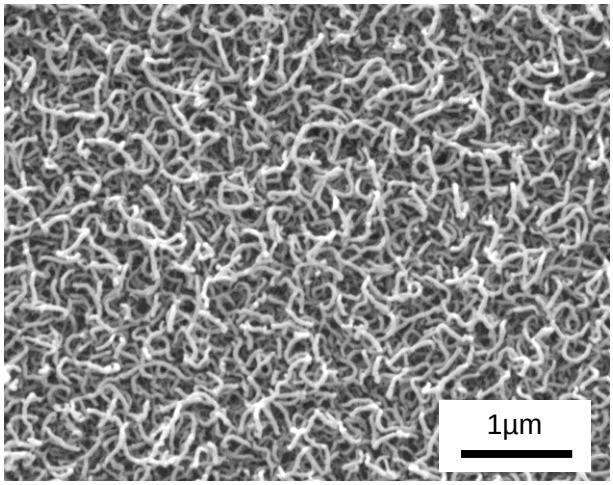

Figure 1-4. SEM image of deposited Al/Al_2O_3 nanowires on a glass substrate.

Veith et al. [9] described a mechanism for the transformation of biphasic Al/Al_2O_3 nanoparticles into nanowires. This mechanism is applicable for the deposition temperatures around 610 ± 50 °C where {AlO} is the driving force of Al/Al_2O_3 biphasic features by disproportionational process similar to a formation of Si/SiO_2 nanowires from SiO vapor [42, 53-55]. Veith and his co-workers [9, 26] proposed that the decomposition reaction of $[^tBuOAlH_2]_2$ resulting HAlO (eq. 2 in chapter 2.2) may work as an intermediate progress at higher deposition temperatures. This provides intermediate metastable {AlO} vapor by a subsequent degassing of hydrogen (eq. 3-1 in chapter 2.2). During the deposition process, the {AlO} molecules are combined into nano clusters (fractal ball-like particles) on the substrate by Ostwald ripening where diffusion from smaller crystals to bigger ones to reduce the free energy of the entire system [56]. Subsequently the precipitation of Al nanoparticles starts as a phase separation in condensed {AlO} clusters. As shown in eq.3-2 in chapter 2.2, the formal Al^{2+} of {AlO} disproportionate into Al^0 and Al^{3+} with a stoichiometric molecular ratio of 1:2 [9]. At a higher temperature (near to the melting point of pure Al) the precipitated Al could be a molten form because the surface melting temperature of nanoparticles can be much lower than that of their bulk materials [57]. Thus metallic Al could act a catalyst as preferred nucleation sites similar to typical VLS process. But it is different to the conventional VLS process since the catalyst is not a noble metal. The metallic aluminium itself serves as a catalyst (self catalyst) and remains at the tip of the deposited nanowires. The intermediate metastable {AlO} vapor is generated constantly thus Al nanowires surrounded by oxide shells form continue during the deposition process.

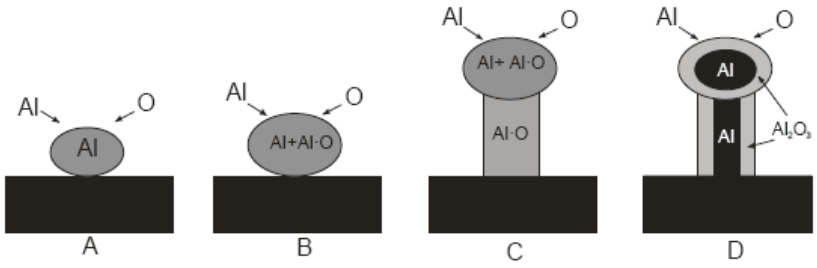

Figure 1-5. Schematic illustration of the self catalytic growth mechanism for the synthesis of Al/Al_2O_3 core shell nanowires [44].

Figure 1-6 shows TEM image of Al/Al_2O_3 nanowires deposited on a glass substrate at 630°C. The size of the nanowires is approximately 30-40 nm in diameter. The diameter of nanowire is depending on the Al core at the tip. It can be seen clearly Al core at the tip in the TEM image of the deposited nanowires (Figure 1-6 A). Figure 1-6 B shows Al metallic core encapsulated by Al_2O_3. The spherical particles at the tips of the deposited nanowires remind of a catalyst supported VLS growth mechanism. In this case it is possible evidence that Al/Al_2O_3 nanowires were grown by a self catalyst VLS mechanism.

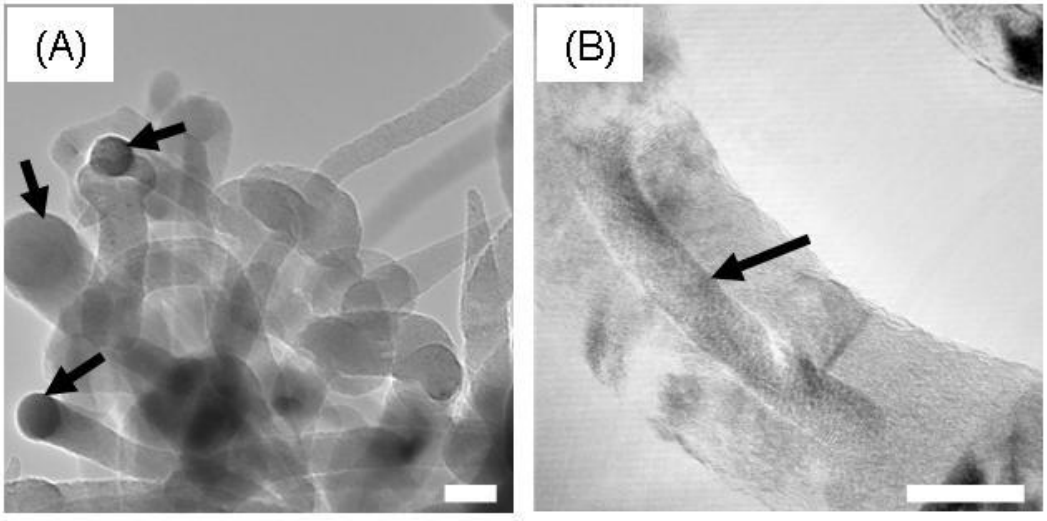

Figure 1-6. TEM images of nanowires at (A) low magnification for overview and (B) at higher magnification of single nanowire. Scale bars represent 20 nm and arrows indicate metallic Al core.

2. Applications of 1D Al/Al_2O_3 nanostructures

The Al/Al_2O_3 composites can be used in different ways. In the following section, some applications are introduced that have been studied in the last few years and applied for 2 patents [WO 2012/007401, WO 2011/147569]. The part of this works was published in recent [32].

2.1 Surfaces for adhesion

One-dimensional, wire-like Al/Al_2O_3 nanostructures exhibit adherence to various surfaces depending on their aspect ratio, their degree of interpenetration and entangling. The formed composite film may be used for permanent bonding of metals or ceramics. For example, thin films composed of chaotic Al/Al_2O_3 nanowires can be used as sort of glue between metal or ceramic surfaces. In this application the metallic or ceramic surface, which should be planar, is coated with Al/Al_2O_3 nanowires. The coated face is now placed on a planar metal or ceramic substrate, and the whole system is heated up to 650 °C (either by induction or in an oven). After few minutes the two materials stick together in such a way that even under forces up to 130 N the two materials cannot be easily separated. The preliminary test was performed 4 times and as shown in Figure 2-1. The used substrates were round shape copper plates. Apparently the composite has penetrated also into the uncoated surface and serves as a connecting film between the two substrates.

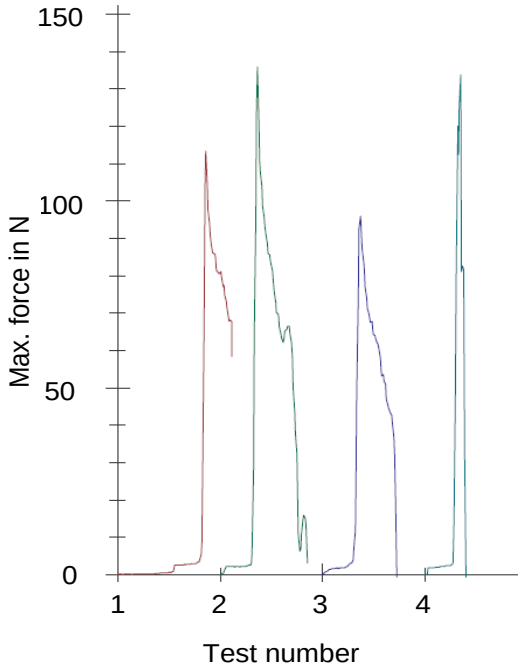

Figure 2-1. The results from a tensile test of two copper plates bonded with Al/Al_2O_3 nanowires.

The Al/Al_2O_3 coated surfaces can also be used as adhesion promoters for organic layers. By applying a standard peel-off test (ASTM D 3330), the adhesion between the Al/Al_2O_3 composite film and the substrate was estimated then again a very interesting result was observed which shows a strong adhesion between the pressure sensitive tape (3M Electrical Tape 92, Polyimide Film with Thermosetting Silicone Adhesive) and the one-dimensional composite nanostructure. The gain in adherence is due to the possibility of entangling between the metal/ceramic nanowires and the polymer based adhesive layer of the tape as may be deduced from inspection of Figure 2-2. The peel off test was applied on different surfaces and definitely the nanowire coated surfaces exhibit an enhanced adhesion on every type of coated substrate (glass, aluminium and copper with Al/Al_2O_3 wire-like composite) as shown in Figure 2-3.

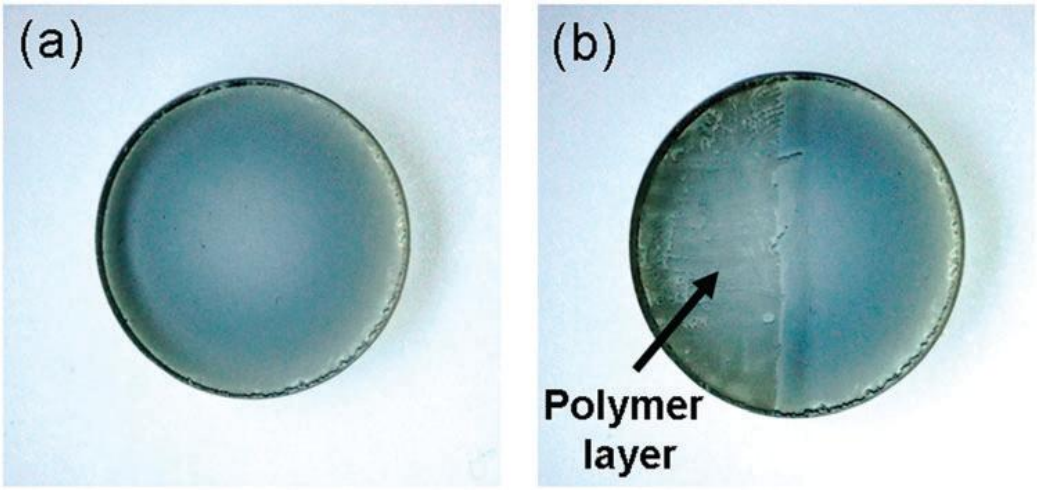

Figure 2-2. (a) Al/Al_2O_3 composite nanowire coated glass before sticking the adherence tape and (b) Al/Al_2O_3 composite nanowire coated glass after sticking and peeling-off the tape. The arrow shows the accumulated adhesive left on the surface of the coated glass after peel-off.

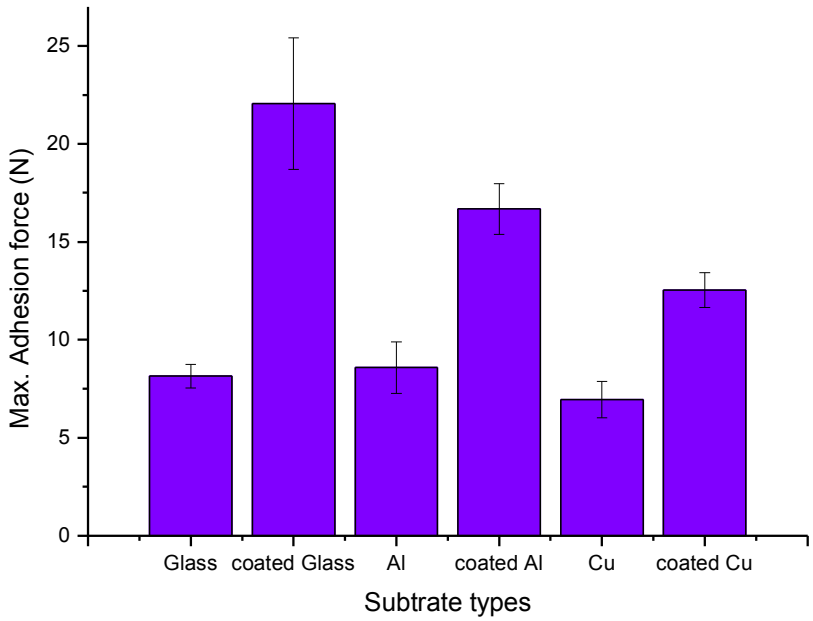

Figure 2-3. Comparison of adhesion behavior for adhesive tape of non-coated and Al/Al_2O_3 composite nanowires coated substrates of glass, aluminium and copper.

2.2 Optical property for solar absorber

Since the Al/Al_2O_3 core/shell nanowires layer is black, the absorption of light by such films is a characteristic property. The UV-VIS-NIR spectrum of the deposited layer is

plotted in Figure 2-4. As shown in the spectrum, It is possible to see a broadband absorption affect in the NIR region between 800 nm and 1200 nm wavelengths which can be interesting for ultra-thin solar absorbers.

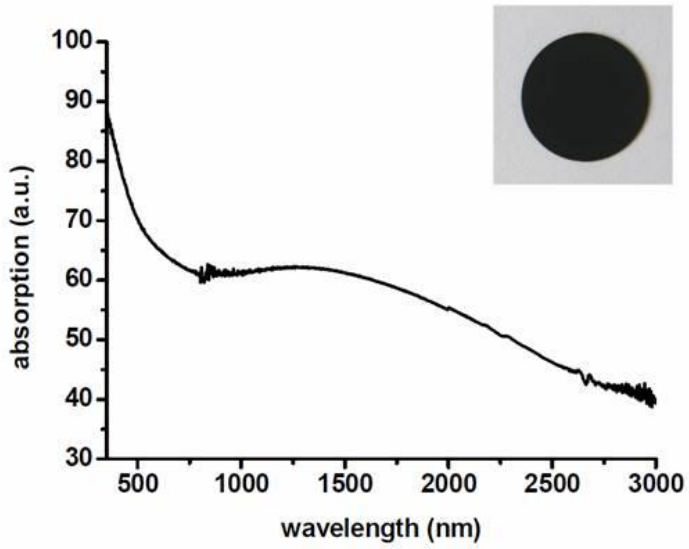

Figure 2-4. Optical absorption spectrum of Al/Al_2O_3 composite nanowires coated on glass substrates. Inset shows the Al/Al_2O_3 nanowires coated substrate [32].

As shown by Ekinci et al. [58], Al nanoparticles with 40nm in diameter exhibit two enhanced absorption peaks in the UV region due to the bulk plasma resonance of Al. One peak is at about 250 nm and the other is at about 190 nm due to the dipolar and quadrupolar mode, respectively. Similarly, the optical spectra given in Figure 2-5 show a sharp and narrow peak at about 250 nm thus it could be confirmed as the dipolar mode of the surface plasmon resonance from Al cores of Al/Al_2O_3 composite nanowires. Although increased absorption peak was observed near to 200 nm, the measurement could not be carried out below 200 nm because the UV-VIS-NIR spectroscopy used for analyzing of Al/Al_2O_3 layers did not cover the whole UV range which is needed for the characterization of the Al core.

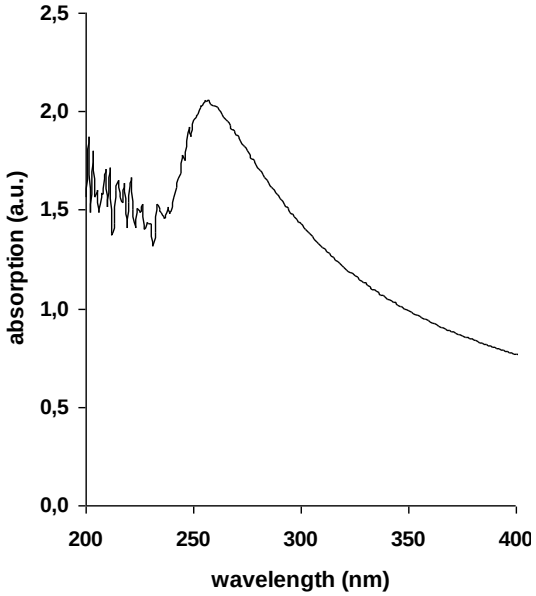

Figure 2-5. UV absorption spectrum of Al/Al_2O_3 composite nanowires coated on glass substrates.

On the other hand when IR light is applied to these nano structures, they absorb also the IR light. As can be seen in the Figure 2-6, coated and bare stainless steel substrate were exposed to IR light from a fast IR annealing system, the substrate temperature was measured from the backside. At the same time the coated sample shows the temperature rise higher than the bare substrate. It reveals clearly that, the Al/Al_2O_3 nanowire coated samples enhance the absorption of IR light more than bare substrate.

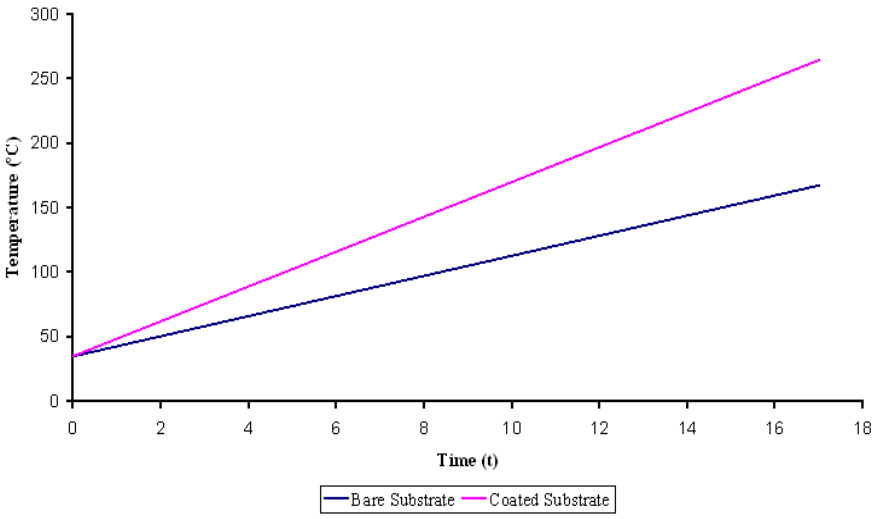

Figure 2-6. IR induced temperature incensement of Al/Al_2O_3 nanowires coated and bare stainless steel. Time scale is second.

3. The concept of the parabolic flight

Parabolic Flights are an essential way of achieving weightlessness and exclusively used for training astronauts and pilots for military achievements. Only few accesses of the parabolic flights are dedicated to scientific experiments and technological tests of space systems and hardware. Simplicity of preparation and of operations, reduced costs, repeated weightlessness phases and opportunity for researchers present on board to directly work on their experiment are key points not offered by any other available means. The Airbus A300 ZERO-G aircraft is used exclusively for test flights and experimental flights. The technically challenging parabola campaign is performed by experienced French test pilots, while a team that has been specially trained in zero-gravity environments assists the scientists and takes care of safety on board. Worldwide, three aircraft are used for parabolic flights: a DC-9 in the USA, an Iljushin 76 MDK in Russia and the Airbus A300 ZERO-G in Europe. Following information was given by DLR (*Deutsches Zentrum für Luft- und Raumfahrt / German Aerospace Agency*) and NOVESPACE (*French Microgravity Aviation Company*) [59].

For the Parabolic Flights, four specially trained test pilots and flight test engineers are together to fly for these unique maneuvers, three of them are responsible for each spatial direction. Their goal is to be achieved by fine adjustment of the position and heading of the aircraft and of the engine thrust to the longest possible period of weightlessness with minimal residual accelerations. Parabolic flights are performed onboard aircrafts following a flight pattern which alternates ascents and descents with short level flight breaks. Each of those maneuvers, called parabolas, provide up to 22 seconds of reduced gravity or weightlessness as shown in Figure 3-1. During those reduced gravity phases, researchers fly onboard the aircraft perform experiments and collect data with conditions impossible to simulate on Earth.

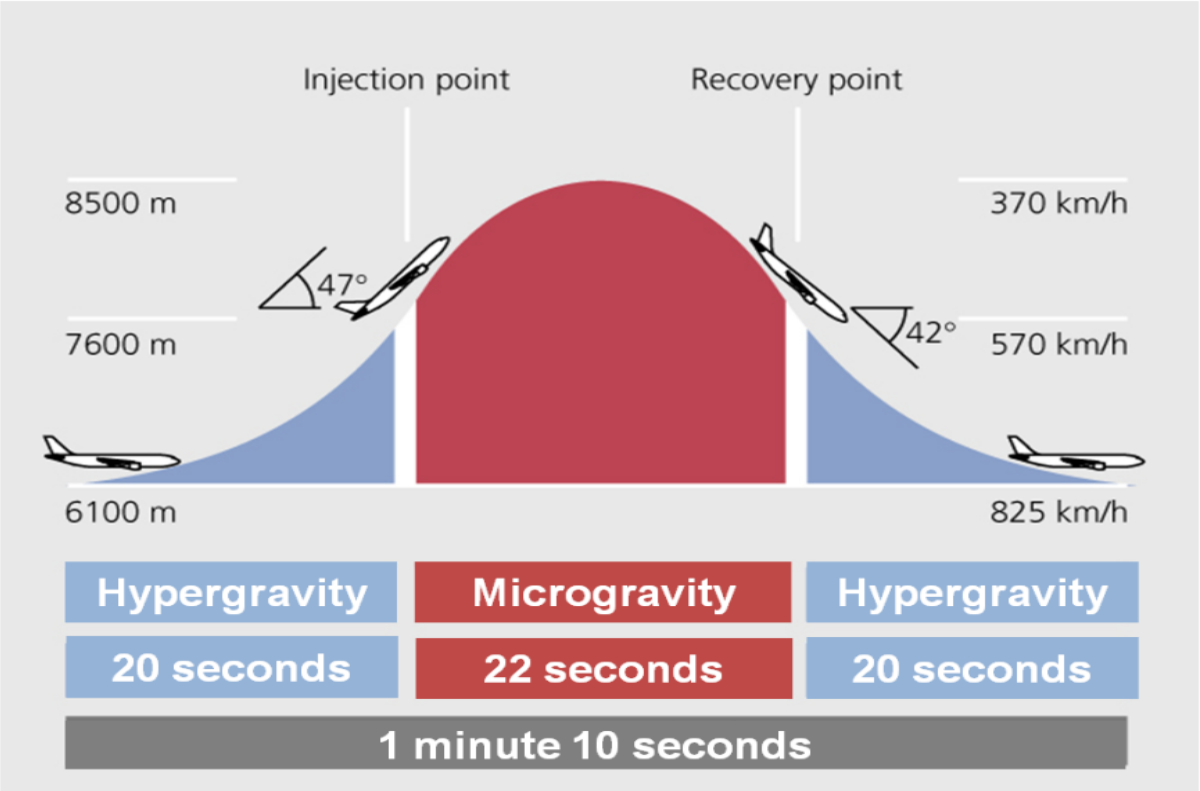

Figure 3-1. Illustration of the parabolic trajectory flown by the parabolic research aircraft. Approximately 20-25 seconds of microgravity are achieved during each parabola [60].

During parabolic flight manoeuvres, from horizontal flight, the aircraft flies straight up with its full thrust momentum to achieve a vertical acceleration of 1.5-1.8 g, nearly twice the normal force of gravity prevails. After the plane climbs at an angle of 47 degrees, the pilot throttles the engines back and approximately 22 seconds of weightlessness occurs as the plane arcs over into a dive. After the interception of the aircraft in a steep downward for 20 seconds at which an increased acceleration of about 1.8 g prevails then the gravity level is normalized to 1 g during horizontal flight. By default, the parabolic flights from Bordeaux-Merignac airport in France or from the airport Cologne / Bonn on behalf of DLR are performed. For its parabolic flights the DLR uses the Airbus A300 ZERO-G. The European Space Agency (ESA) and the French space agency CNES also use the aircraft, courtesy of French company NoveSpace. NoveSpace has been performing Parabolic Flights with the Airbus A300 ZERO-G since 1996. The technical information is given by NoveSpace and can be expressed as follows.

Airbus A300 ZERO-G:

- Experimental aircraft capable of performing parabolic flights
- Maiden flight: 28 June 1973
- First commercial parabolic flight: 1997
- Managed and owned by: Novespace
- Serviced by: EADS-Sogerma
- Sponsors: CNES and ESA
- Flight operations and safety: French test flight centre CEV

Technical data of the Airbus A300:

- Length: 53.62 meters
- Wingspan: 44.84 meters
- Height: 16.90 meters
- Turbines: General Electric CF6-50
- Number of seats: 40 for scientists, 10 for flight team
- Experimental area: 20 meters x 5 meters

3.1 The CVD apparatus for parabolic flight

The chemical vapor deposition experiments of single source precursor $[^{t}BuOAlH_2]_2$ are usually performed in a vertical tubular quartz reactor operating in a cold wall configuration (see Figure 1-3 (a) and (b)). However, this system does not fulfill the stringent safety conditions in the airbus especially due to the stability of the apparatus. In this context, as shown in Figure 3-2, a newly designed CVD apparatus was constructed for parabolic flight.

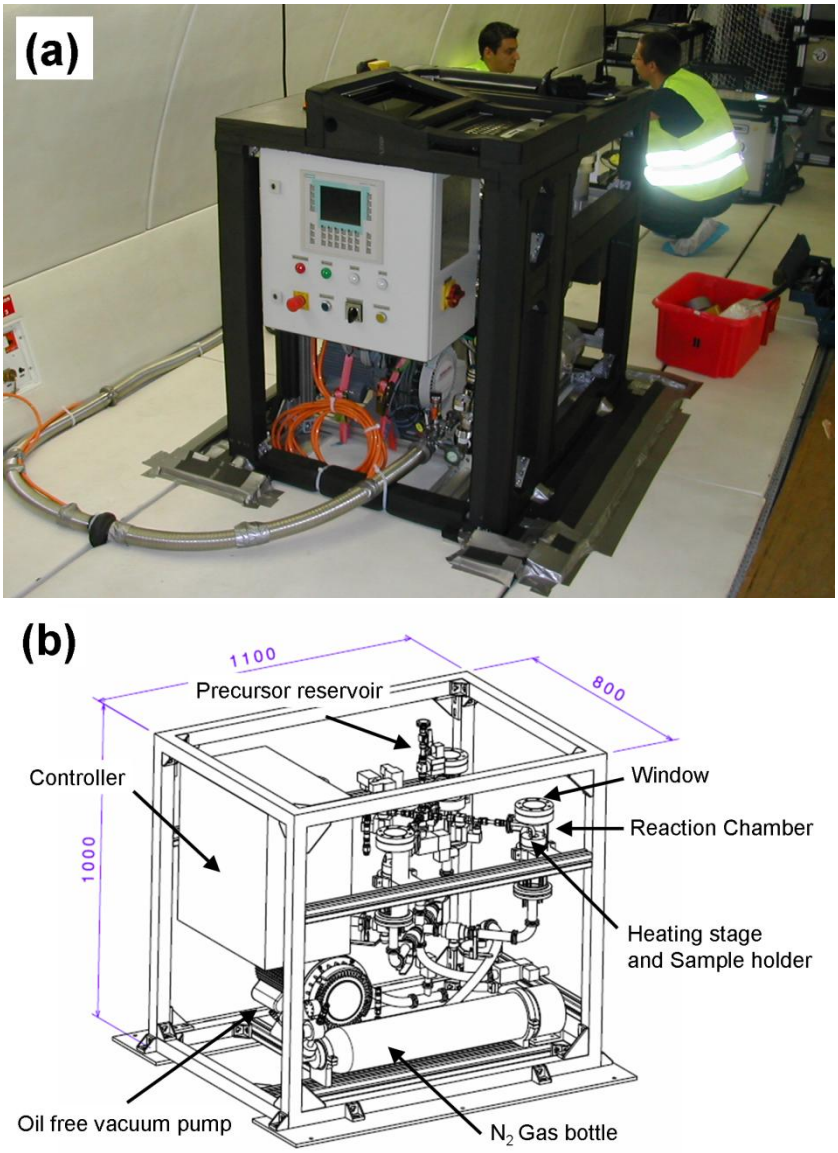

Figure 3-2. (a) CVD apparatus settled in the air bus for parabolic flight and (b) schematic drawing of the CVD apparatus. Dimension unit is mm.

In the CVD apparatus for parabolic flight, 4 different reaction chambers (each charged by 5 substrates) were installed. Instead of glass, stainless steel is used for the reaction chambers, the precursor reservoir, the cold trap and the pipelines. The windows to observe the inside of the chambers were made of polycarbonate. Figures 3-2 and 3-3 show the CVD apparatus for parabolic flight. The reaction chambers are located in the corner of the CVD apparatus with polycarbonate windows at the top of the reaction chamber (see Figure 3-4). A cold trap filled with dry ice is used to cool down decomposition by-products. The byproducts are either condensed in the cold trap and removed after the flight on the ground or ventilated outside through the vent line of the airbus.

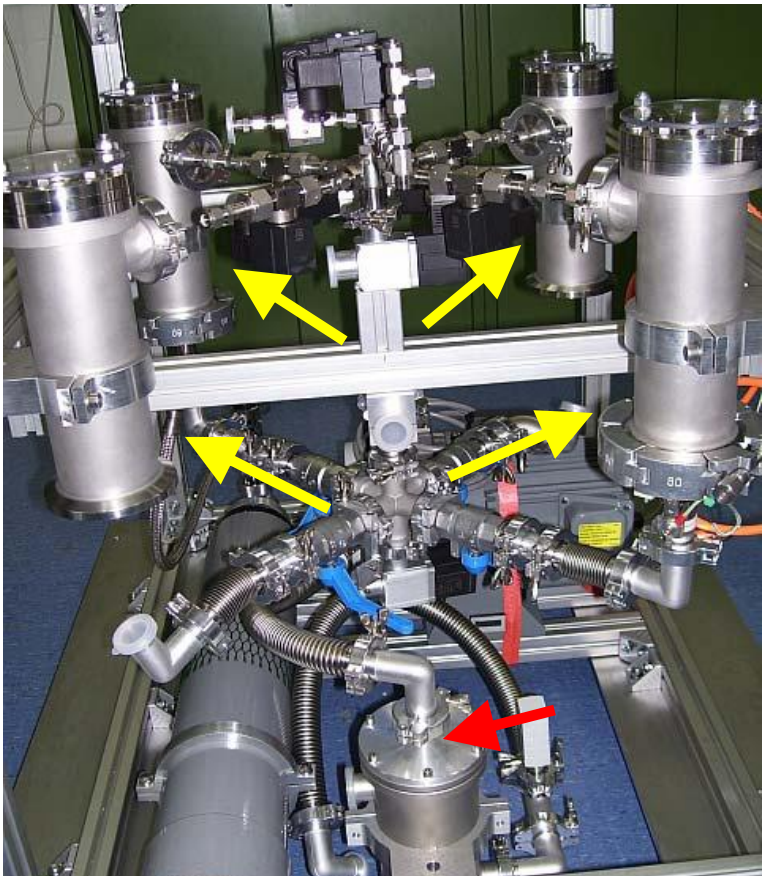

Figure 3-3. The installation of the reaction chambers. Yellow arrows indicate 4 reaction chambers and red arrow indicates the cold trap.

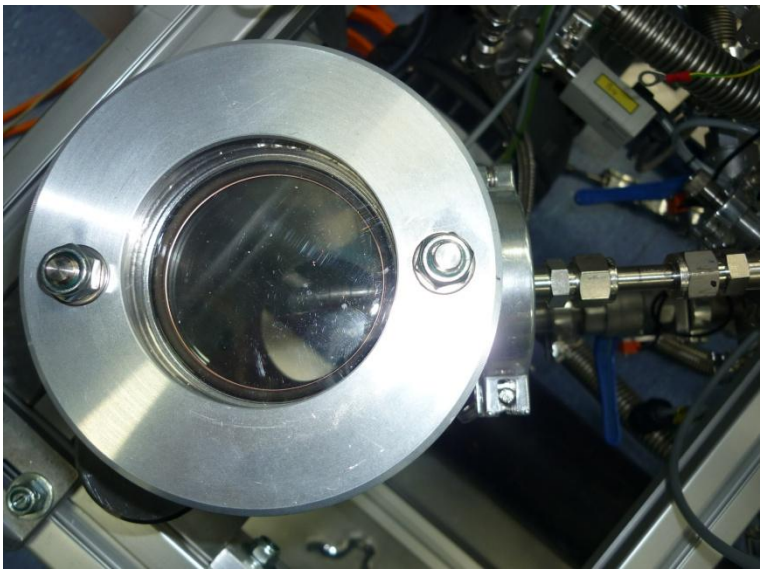

Figure 3-4. A polycarbonate window of a single reaction chamber.

Main control unit at the front of the CVD apparatus contains a Programmable Logic Controller (PLC) with a monitor (Figure 3-5.) and as shown in Figure 3-6, each reaction chamber is controlled by a PLC individually. CVD parameters such as temperature, pressure and deposition time for parabolic flight were chosen and

controlled for each chamber according to the preliminary test on the ground. In addition, there will also be an alarm message on the monitor of the control unit to avoid unwanted programming of a heating temperature more than 700°C and pressure over 1400mbar. In case of emergency, the PLC will close the valves and turn off the heaters automatically.

Figure 3-5. Control box of CVD apparatus.

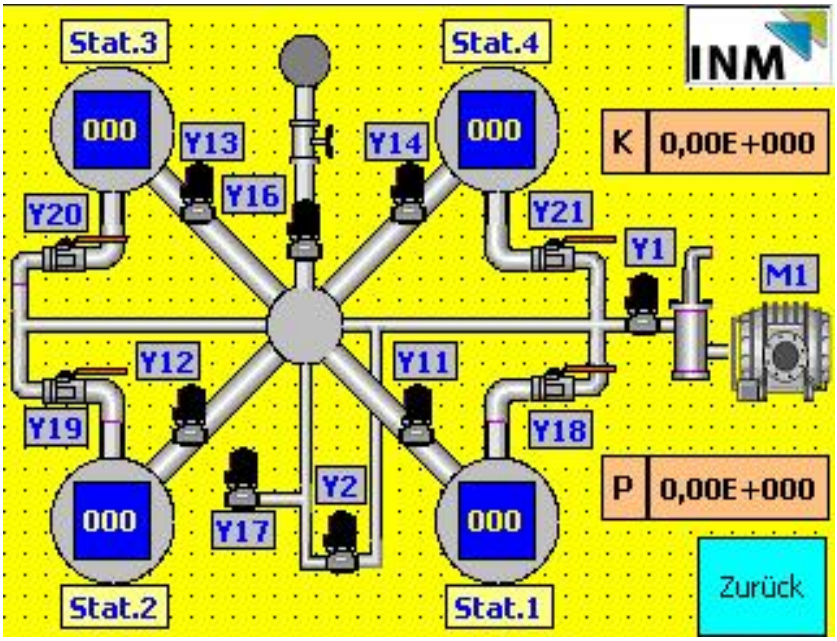

Figure 3-6. Reaction chamber controller by a Programmable Logic Controller (PLC).

4. Experimental procedure

Prior to the deposition the whole CVD system was held at a low pressure about 10^{-3} mbar via an oil free vacuum pump. The precursor is exposed at low pressure of 10^{-2} mbar through a stainless steel pipe and to the reaction chamber, where the precursor reacts on the surface of heated substrates. The substrate temperature and the precursor flux are controlled using a thermocouple and the feedback of the pressure measurement in the reactor during the process.

4.1 Synthesis of precursor $[^tBuOAlH_2]_2$

In order to carry out CVD experiment in parabolic flight, the precursor $[^tBuOAlH_2]_2$ was synthesized following the established routes [8, 47]. As described in the literatures, 120 mmol (4.554 g) lithium aluminium hydride ($LiAlH_4$) are dissolved in 80 ml diethyl ether in a flask including a reflux cooler. Afterwards 40 mmol (5.334 g) of aluminium trichloride ($AlCl_3$) are dissolved in 80 ml diethyl ether under cooling and added to the $LiAlH_4$ solution at room temperature with a steady flow, which is followed by the precipitation of lithium chloride (LiCl). To this suspension which is left, 160 mmol (11.859 g) tert-butanole is added to produce hydrogen and the procedure is done between 4 to 5 hours of stirring at ambient temperature. LiCl is separated from the mixture by filtration and the solvent is evaporated in vacuo subsequently. The remaining solid phase was sublimated at a pressure of 1 mbar and ambient temperature to achieve 15.2 g bis(tert-butoxy aluminium dihydride) $[tBuOAlH_2]_2$ (93% yield); decomposition temperature > 120 °C, melting point 71 °C, sublimation point: 20°C / 1 mbar and calculated molecular mass 204.22 g/mol. NMR analysis has been performed for the synthesized product and values are given by Veith et. al. [8]; ^{1}HNMR (δ, i-TMS): 1.22 p.p.m. (s, 18H, $-C(CH_3)_3$, 4.43 p.p.m. (s, $-AlH_2$), ^{13}CNMR (δ, i-TMS); 30.36 p.p.m. ($-CH_3$), 76.43p.p.m. ($-C(CH_3)_3$)

The chemical reactions of synthesis process are given according to the literature [8]:

$AlCl_3 + 3LiAlH_4 \rightarrow 4\{AlH_3\} + 3LiCl$ (1)

$2\{AlH_3\} + 2^tBuOH \rightarrow [^tBuOAlH_2]_2 + 2H_2$ (2)

4.2 CVD of $[^tBuOAlH_2]_2$ in parabolic flight

The precursor is introduced into the reaction chamber by opening the valve and is decomposed on the surface of the substrates which are heated up to a temperature range of 400-600°C. The precursor flow was maintained generally 15-20 seconds. The numbers (1), (2), and (3) in Figure 4-1 indicate the precursor path during the CVD process. The CVD apparatus was primarily controlled by a PLC during the parabolic flight. The substrates are heated through conductive micro ovens while in a conventional CVD system, a high frequency inductive coupling is used to heat the substrates by placing on a graphite substrate holder.

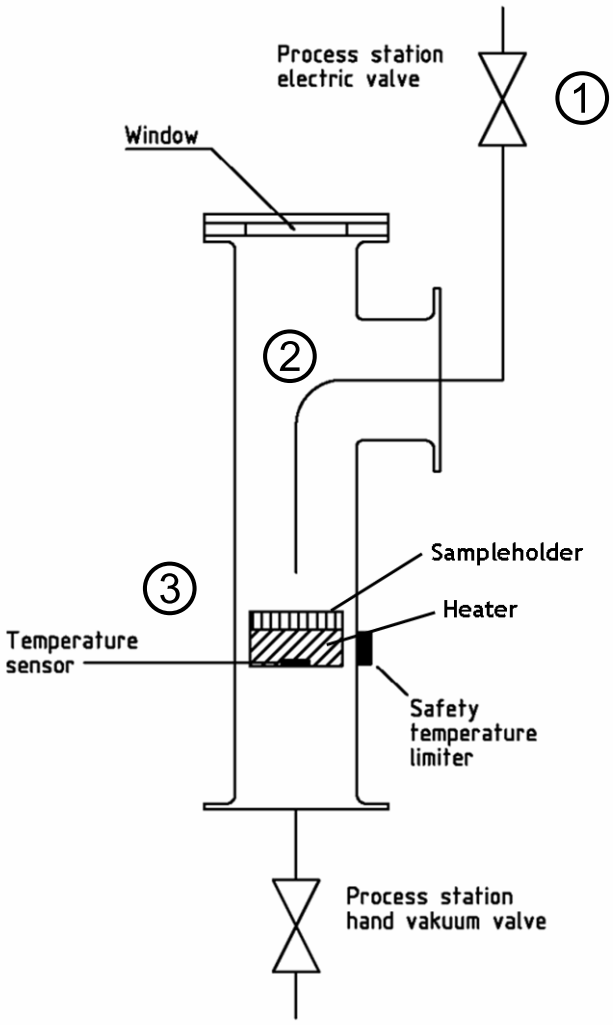

Figure 4-1. Synoptic diagram of the single reaction chamber. Numbers represent: (1) magnetic valve, (2) metal tube and (3) heating stage.

Figure 4-2 shows the inside feature of a single reaction chamber of the CVD apparatus. In the middle of the chamber an electrically driven resistor heating stage is located (red colored) and 5 copper substrates are placed on the heater with a fixing plate to prevent any movement of the substrates during the parabolic flight. All those parts were made of copper which transfers the heat efficiently and settled in a MARCO (ceramic insulator) block which prevents heating up the outer wall of the chamber during the CVD process.

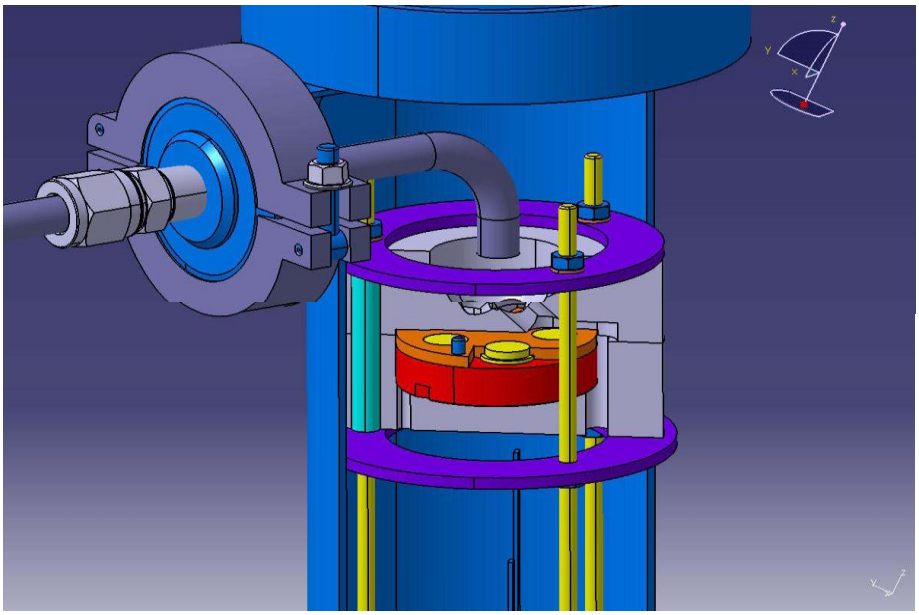

Figure 4-2. Illustration of the single reaction chamber.

As mentioned, in order to control unintended temperature or pressure increase the temperature and the pressure inside of the CVD apparatus were monitored by thermo couple combined with the heater and pressure sensors located inside the reaction chambers, respectively. The heating rate of the heating stage was 3.5°C per second and no interruption among the reaction chambers was observed.

Afterwards the precursor was introduced into the reaction chambers by opening manual and magnetic valves between the precursor reservoir and the reaction chambers. The pressure level of the reaction chambers was kept stable prior to the deposition process. The precursor reservoir was specially designed for the parabolic flight. As shown in Figure 4-3, the precursor reservoir was an assembly of a metal reservoir, labyrinth seals and a hand valve. By using labyrinth seals the powder formed precursor $[^{t}BuOAlH_2]_2$ was prevented traveling into the reaction chambers.

Only the gas formed precursor under low pressure was able to travel into the reaction chamber.

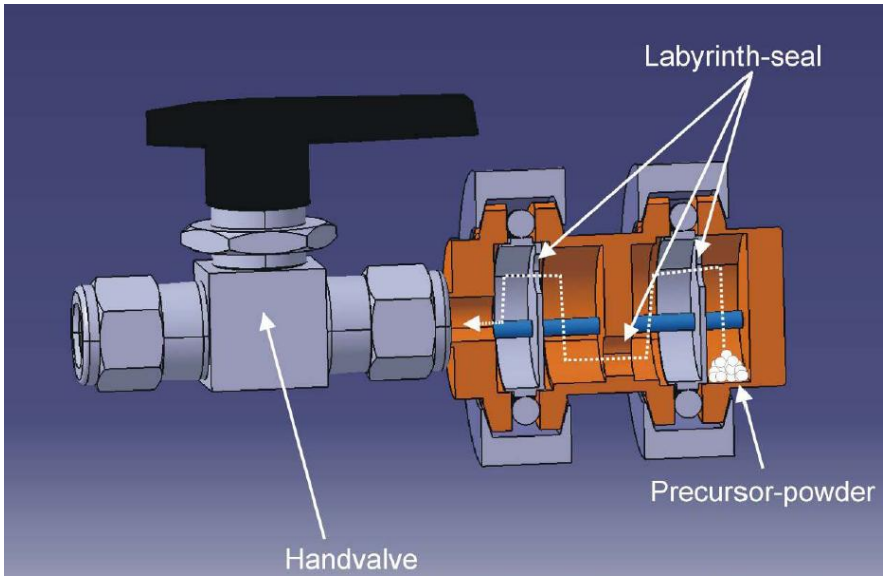

Figure 4-3. Illustration of the precursor reservoir.

The precursor flow was regulated following the feedback of the pressure sensors in the reaction chambers during the processes by manipulation of the valves via PLC. Prior to opening the valve, each chamber was kept at pressure level below $3*10^{-3}$ mbar. As shown above (see Figure 3-1) the gravity condition remains 20-22 seconds in hyper and micro level, respectively. Due to that limitation the flow of SSP need to be introduced in the reaction chamber within 20 ± 5 seconds in order to prohibit further reactions at unintended gravity condition. The pressure level of the reaction chamber did not exceed more than 10^{-2} mbar. After many initial CVD tests on the ground, parabolic experiments were carried out for 5 days; each with 31 parabolas (more 150 parabolas) therefore a total of 50-55 minutes of weightlessness or hypergravity were available.

5. Result and discussion

Figure 5-1 shows the variable gravitational acceleration (G) in a parabola given by Novespace after the experiment. There are 3 types of G value; Gx and Gy reveal the transverse acceleration of the airbus thus they do not change when airbus flies straightforward and Gz indicates vertical gravitational acceleration that reveals hyper and microgravity level in the airbus. The altitude (Alt) was varied approximately from 65000 to 95000 meters. It means freefall of the airbus was ca. 3000 meters. A relatively stable microgravity phase is observed in the time laps between 25-45 seconds followed by longer-duration of hypergravity phase.

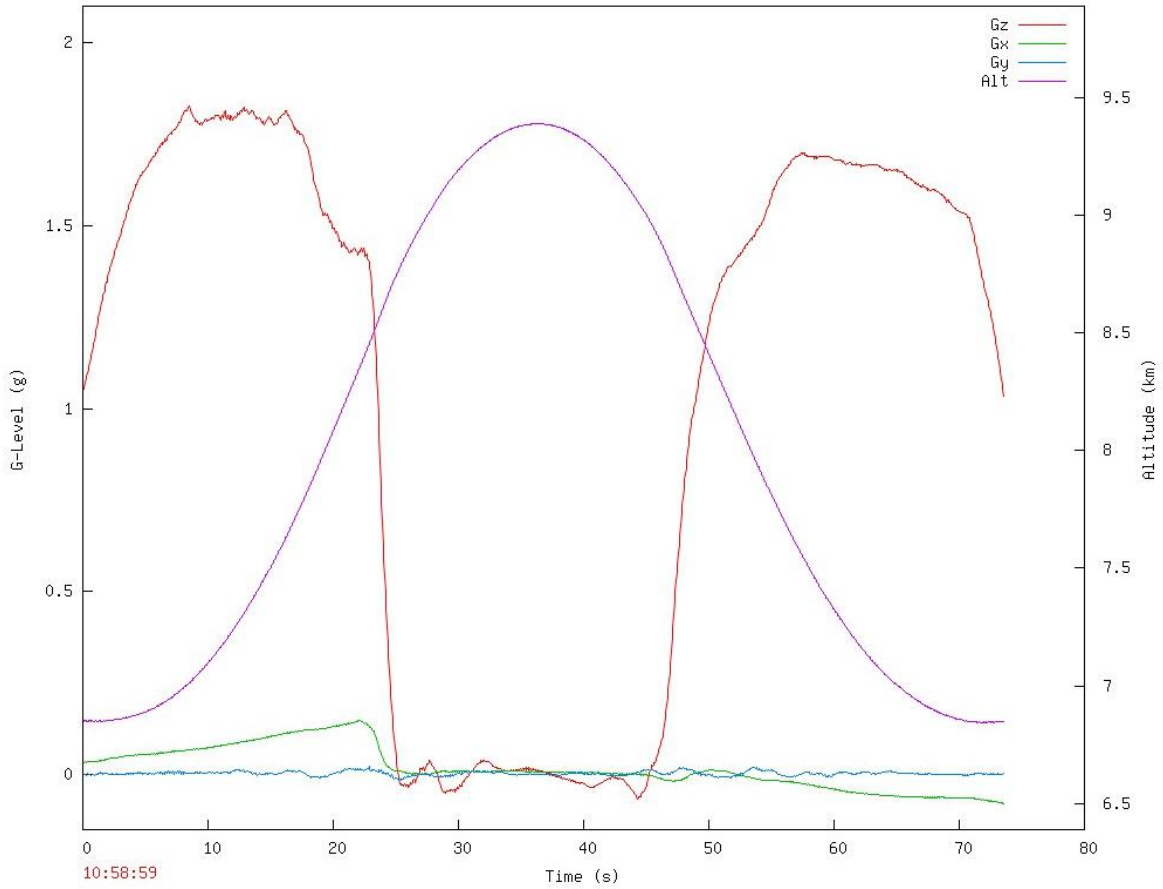

Figure 5-1. Example of the gravitational acceleration obtained during a parabola.

A detailed profile of the accelerometer data at microgravity is shown in Figure 5-2. Parabolic trajectory flown by the specially designed Airbus A300 produced brief periods of microgravity (Ca. 0.04 G) lasting for approximately 20-25 seconds. The initial transition into the microgravity phase lasted 1-2 seconds.

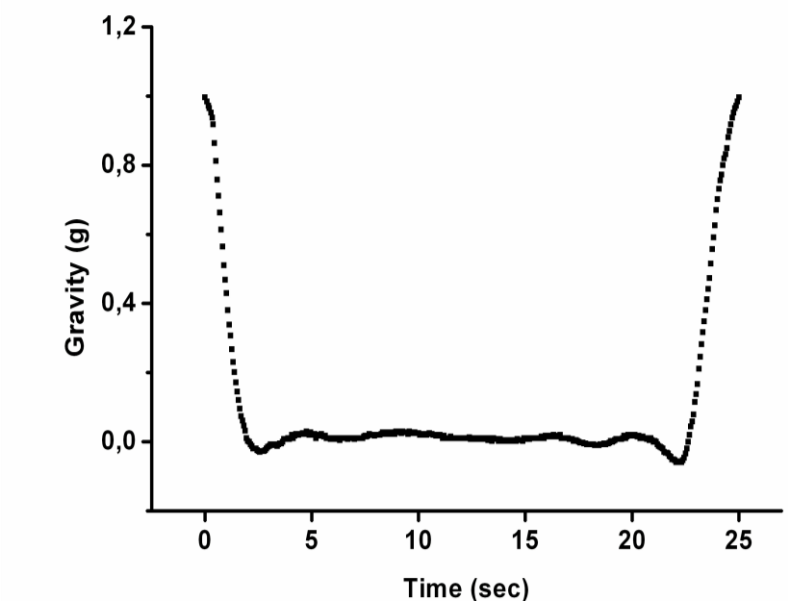

Figure 5-2. Example of the gravitational acceleration during a micro gravity.

As shown in chapter 2.4, Veith et al. [9] proposed that at elevated temperatures (near to the melting point of Al) the formed in Al_2O_3 embedded Al particles may stay in liquid phase similar to catalyst particles used in a typical VLS process and they act as seeds for the growth of Al/Al_2O_3 nanowires. More than a decade, the research group of Veith indicates that the density and the shape of Al/Al_2O_3 nanowires highly depend on the first stage where the Al/Al_2O_3 particles form after the decomposition of the precursor. The method has been addressed also for the synthesis of other metal/metal oxide biphasic systems such Ge/GeO_2, Sn/SnO_2, Pb/PbO_2 where Ge, Sn and Pb are metals [61]. Indeed the temperature is the key factor in the growth of Al/Al_2O_3 nanowires because the temperature of the substrate determines whether nucleated Al seeds are in the solid or liquid phase. This current work aimed to explore the gravity (at terrestrial, micro- and hypergravity) effect on the nanoparticle (which at higher temperatures becomes a seed droplet) and nanowire growth by decomposition at low and elevated temperatures, respectively.

Basically two sets of experiments (deposition of Al/Al_2O_3 material at (a) 400°C and (b) 600°C) were carried out to investigate the growth mechanism of nanostructures within 120 parabolas. As shown in Figure 5-3, at 400°C only solid spherical particles were observed on the substrate surface. There is a clear difference in size and morphology of those spherical particles obtained at 0.04 G, 1 G and 1.8 G although

all other parameters such as time, pressure and temperature were constant. In Figure 5-3 (a), similarly to a self-organization manner, the nano-particles with a diameter of 8-10 nm are regularly distributed under 0.04 G (microgravity). At 1 G (terrestrial gravity) the deposited ball shaped particles formed large clusters in a fractal manner rather than separately distributed fine structures (Figure 5-3 (b)). The mean diameter of these clusters is around 80 nm. The smallest primary particles which form the cluster have a diameter of approximately 8 nm. At a gravity level of 1.8 G (hypergravity), the similar primary particles on the clusters surface are observed and the mean diameter of the clusters is raised up approximately to 120 nm. In addition, these clusters were stick together forming globular entities which have a diameter of around 300 nm (Figure 5-3 (c)).

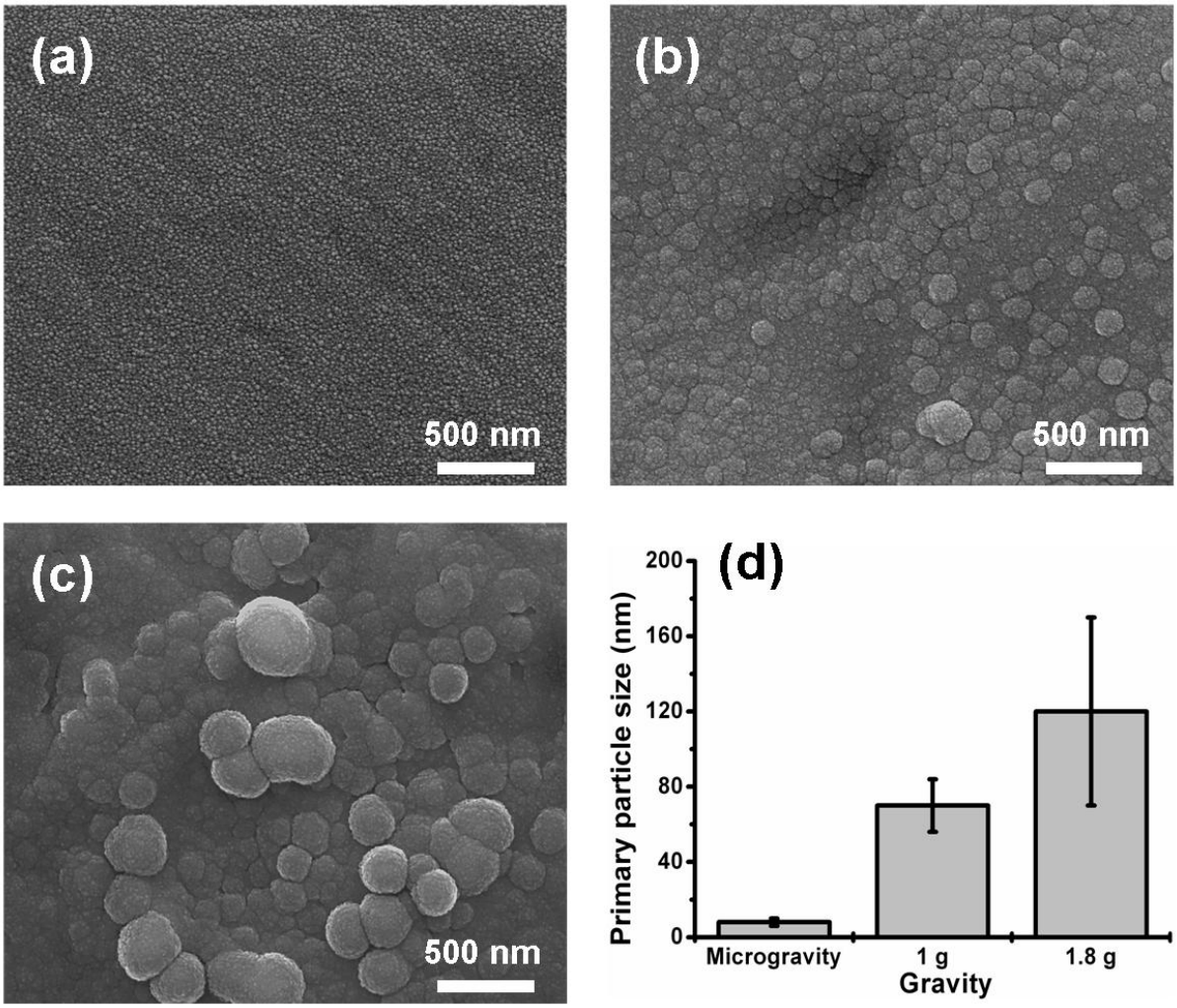

Figure 5-3. SEM Images of Al/Al_2O_3 nanoparticles obtained at (a) 0.04 G, (b) 1 G and (c) 1.8 G. (d) particle size at different gravity condition.

In order to understand such agglomeration phenomena, the effects of gas phase and their interaction with gravitational induced free convection have been focused. A candle experiment under microgravity by National Aeronautics and Space Administration, USA (NASA), showed that the absence of buoyancy-driven convection leads to a spherical form of the candle flame [62]. In a microgravity condition, the supply of oxygen and fuel vapor to the flame is controlled by the molecular diffusion where there is no upward and downward convection as shown in Figure 5-4.

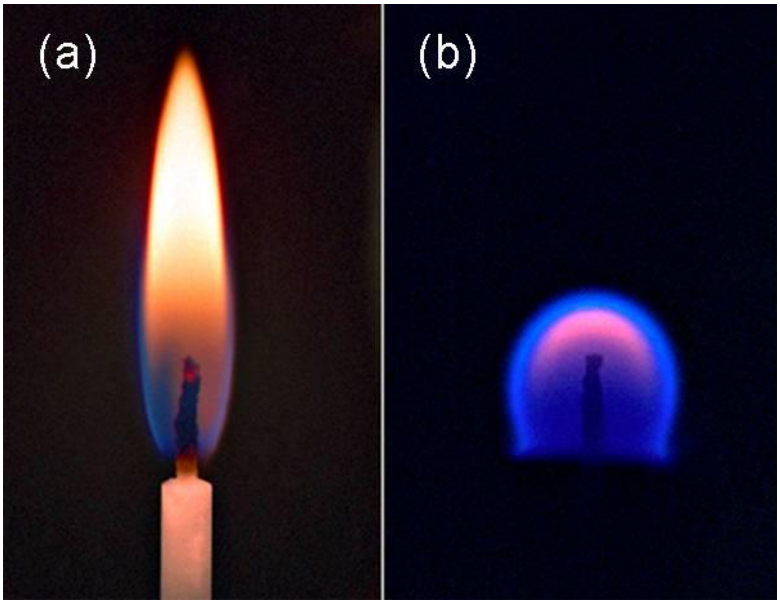

Figure 5-4. The shape of candle flame at (a) normal and (b) micro gravity [62].

Thus in normal (atmospheric) pressure CVD, the dominant gravitational effect which must be counted for is free convective or buoyancy driven transport. This transport process is generally induced by a combination of three factors: temperature gradients, variable gas properties, and the gravity body force. Since at microgravity condition there is no difference for either horizontal or perpendicular reactors, the flow pattern in a cylindrical reactor is truly two dimensional and always diffusion/advection dominated [63]. In many of numerical analyses under the reduction of gravity, flow simulation showed laminar flow without vortex and turbulence [6, 7]. Conversely, in the presence of a vertical (downward) gravitational field at ambient condition, this is an energetically unstable situation which is eliminated by the downward convection of cooler, denser gas and a corresponding upward displacement of the hotter, less dense gas. The superposition of this gravitationally induced free convection on the forced convection of the carrier gas and precursor species is termed mixed flow.

However, at low pressures, the conduction is the main heat transfer mechanism. Thus the classical convection is not valid because the CVD experiment in this current work was carried out at low pressures [64]. In such systems, thermal creep may strongly influence the whole system [65]. Thermal creep basically refers to the motion of fluid opposite to the temperature gradient along the gas-particle surface [66]. Recently, Schwabe et al. presented thermal creep convection using a particle tracing method in a plasma chamber in which vertical temperature gradient is present. The particles move downwards along the vertical walls of the chamber due to thermal creep. When they reach the bottom of the chamber, they move into the middle of the chamber and back upwards in the region outside of the creep zone close to the walls. This leads to convective vortex motion so called creep induced gas convection [67]. At ambient pressures, free convection occurs and the gas motion spreads into the whole of the vacuum chamber.

In our case, gravity and thermal creep are counteracting on the substrate where the lateral temperature gradients exist. Additionally at terrestrial conditions, gravity acceleration is the dominant force inducing the motion of gaseous species downwards to the substrate as similar study of gas flow in CVD system under gravity acceleration [68]. It is believed that this triggers excessive interaction of hotter species (moving with higher momentum) with the surface and this leads to agglomeration of primary spherical particles. At hypergravity this effect becomes more pronounced since larger clusters were observed than those at terrestrial condition. On the other hand under microgravity, thermal creep seems to be the dominant driving force of the whole system and this leads to a net upwards motion from the substrate surface. Thermal creep would be present even in the complete absence of gravity [65]. It can be suggested that the contact angle of the particle on the substrate affect their surface melting temperature and less interaction of liquid particle with surface decreases the nucleation density [69, 70]. Comparable to this observation, Nagai et al. showed that spherical form of the molten metal droplet at a microgravity condition while the shape of the molten metal droplet under normal gravity is ellipsoidal as shown in Figure 5-5 [71]. The contact surfaces under microgravity were smaller than those at normal gravity and constant during the microgravity condition. Therefore microgravity decreases the particle interaction with the surface reducing the contact area.

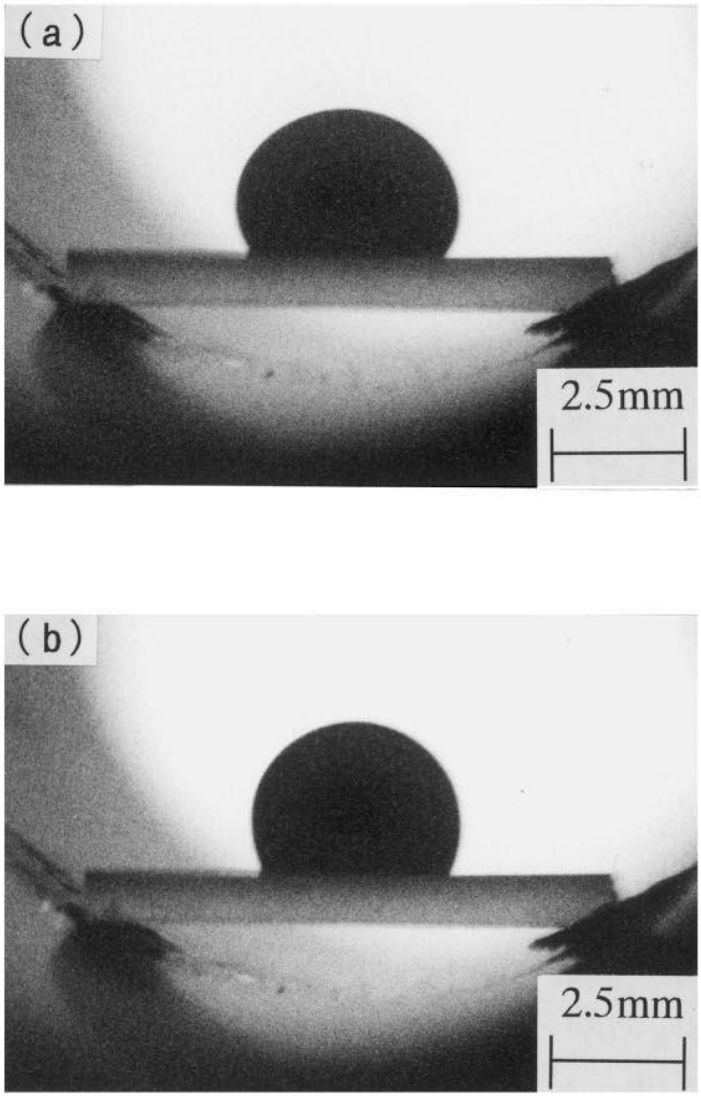

Figure 5-5. The shape of a molten metal drop on a substrate (a) under normal gravity, and (b) under micro gravity [71].

As shown in chapter 1.3 and 1.4, the decomposition of $[^{t}BuOAlH_2]_2$ produces core/shell Al/Al_2O_3 nanowires on the substrate at elevated temperatures. As shown in Figure 5-6, the formation of nanowires is also observed at 600°C. It reveals that there is no apparent effect of gravity on the growing of nanowires. On the other hand, the chaos degree of the nanowires was significantly changed when the gravity level varies from 0.04 G to 1 G and 1.8 G as shown in Figure 5-6 (a), (b) and (c), respectively.

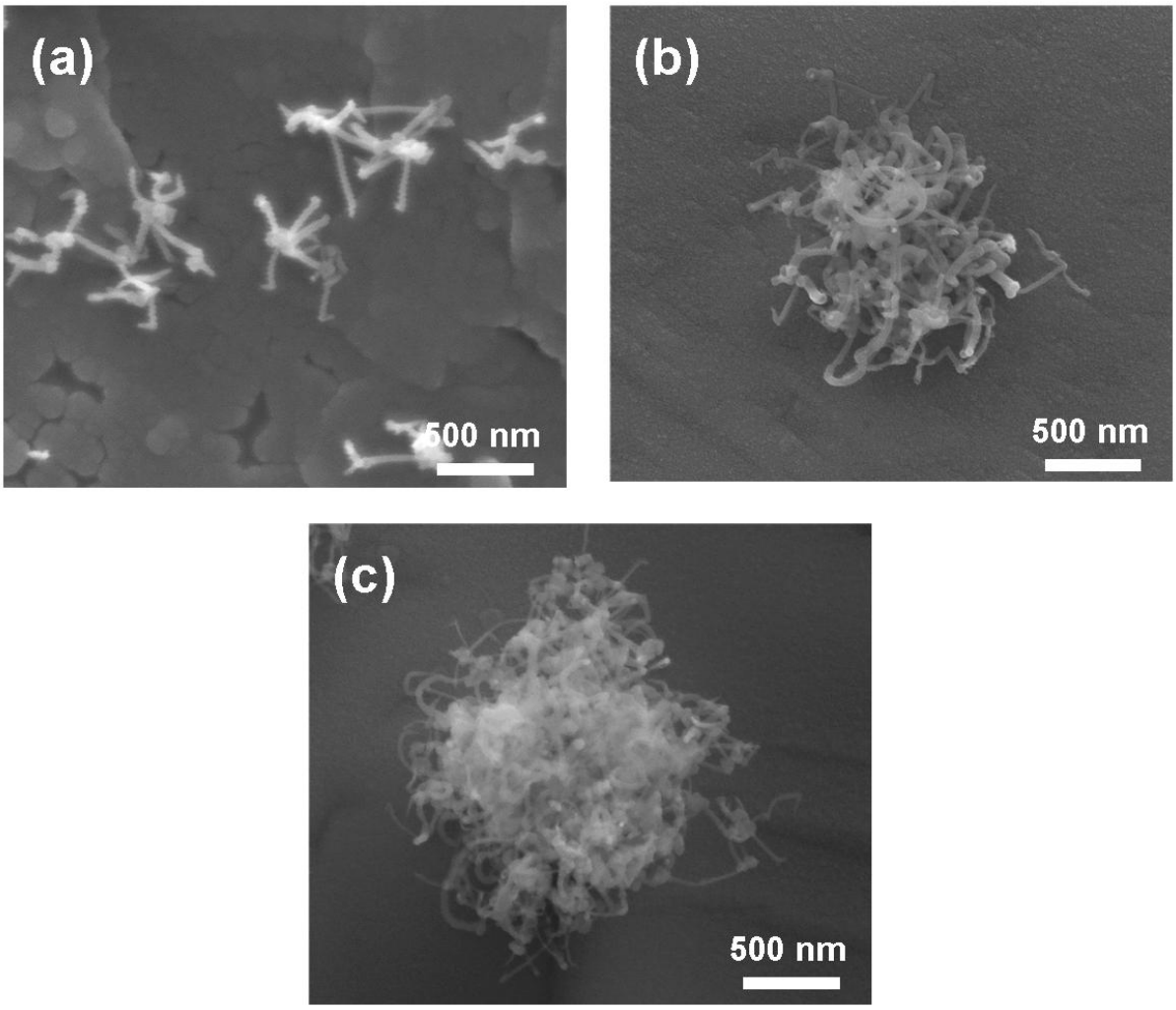

Figure 5-6. SEM Images of Al/Al_2O_3 core/shell nanowires obtained at a) 0.04 G, b) 1G and c) 1.8 G.

As shown in Figure 5-6 (a), the deposited nanowires at microgravity have almost linear structures. TEM image (Figure 5-7 (a)) of the nanowire grown at microgravity shows clearly core-shell nature. Electron Energy Loss Spectroscopy (EELS) indicates that the core is Al and the shell is Al_2O_3 as shown in Figure 5-7 (b). Moreover, the spherical particle on the tip of the nanowire was observed which composed of Al and Al_2O_3 from EELS analysis. This result indicates that gravity does not affect the chemical process since biphasic nature of nanowires was introduced already under normal gravity conditions as shown in chapter 1.4. It can be assumed that a dominance of gravity over the thermal creep increased the chaotic nature of nanowires at terrestrial and hyper gravity conditions since classical convection theory is not valid at low pressure.

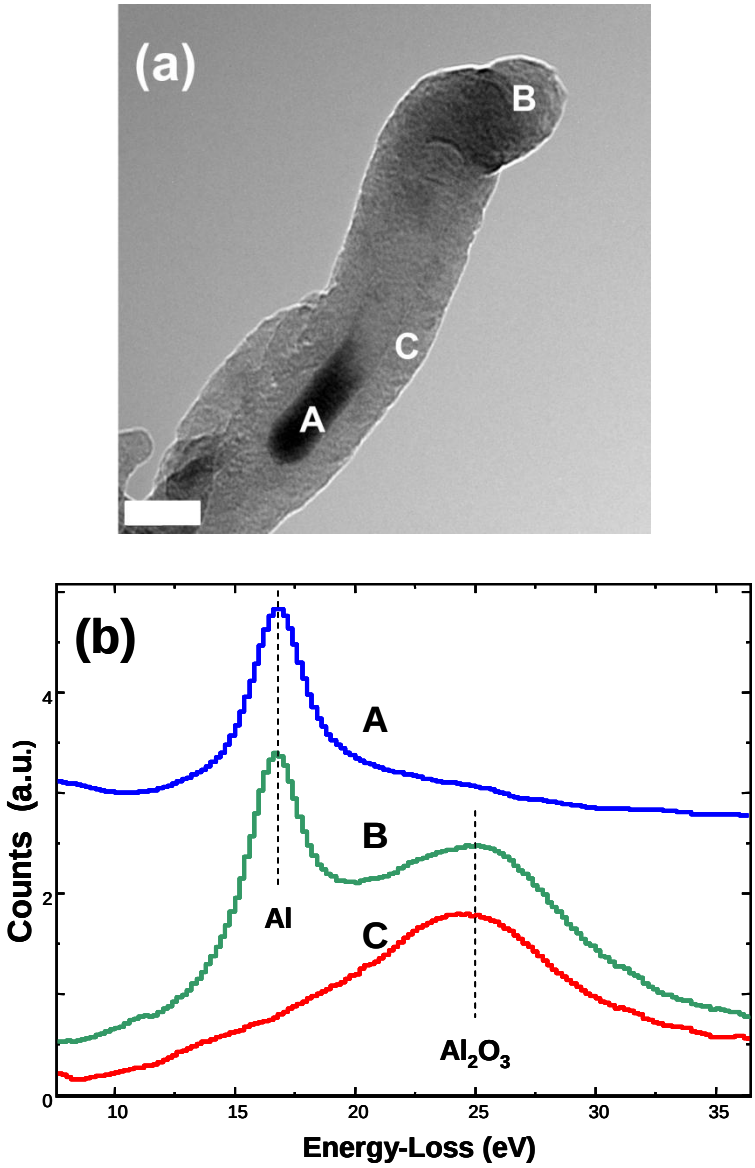

Figure 5-7. (a) TEM image of Al/Al_2O_3 core-shell nanowire and (b) EELS spectra taken from different regions of a nanowire deposited at 0.04 G (shown with A, B and C in Figure a). Scale bar represents 10 nm.

In conclusion, the growth of both spherical particles and nanowires from micro- to hyper gravity showed clearly different morphologies. The spherical particles showed regular distribution and nanowires were grown linearly without bundle formation at micro gravity level. The symmetry of the nanoparticles and nanowires at micro gravity level is caused by the absence of the convection. This is in agreement with observations of crystal growth which is more ideal under weightless conditions. The linear growth of the Al/Al_2O_3 nanowires was observed at micro gravity condition which was not reported at normal gravity experiment. The Al/Al_2O_3 nanowires grown under microgravity have biphasic nature as same as grown under terrestrial gravity. Although all experiment parameters were kept constant, the nanowires obtained at

terrestrial and hyper gravity were no more linear and highly entangled contrast to under micro gravity condition. It is believed that the chaotic nature of nanowires is caused by a dominance of gravity over the thermal creep.

PART 2: Surface structuring on Al/Al_2O_3 surfaces for bio applications

As reported previously, biphasic Al/Al_2O_3 composite transformed to Al_2O_2 by laser treatment thus surface chemistry was always identical. In this context, methods for creating nano/micro structures by direct laser writing (DLW) and laser interference patterning (LIP) of biphasic Al/Al_2O_3 are addressed and Human Osteoblast (HOB), Normal Human Dermal Fibroblast (NHDF), neuronal cells (Dorsal root ganglion and PC12) are cultured to investigate cell behavior upon the surface topography independent from the surface chemistry. The laser process was supported by **Mr. Cagri k. Akkan** and **Mr. Alexander May** (CVD/Biosurfaces group, Leibniz-Institut für Neue Materialien, Saarbrücken, Germany). The cell experiment for Human Osteoblast (HOB) and Normal Human Dermal Fibroblast (NHDF) was carried out by **Dr. Wolfgang Metzger** (Department of Trauma, Hand and Reconstructive Surgery, Saarland University, Germany) and for neuronal cells (Dorsal root ganglion and PC12) by **Mr. Lukas K. Schwarz** (University of Applied Sciences Kaiserslautern, Informatics and Micro-systems-technology, Campus Zweibrücken, Germany)

1. Laser structuring

Despite the principle of the laser was first addressed in 1917 by Albert Einstein who described the theory and concept of stimulated light emission, the first working LASER was invented by Theodore Maiman in 1960 at Hughes Research Laboratories. So far, thousands of lasers have been introduced, but only a few of them are found practical applications in our life fields for the purpose of scientific and/or commercial applications. The term "LASER" originated as an acronym for Light Amplification by Stimulated Emission of Radiation [72].

Laser is a device that produces intense light (monochromatic, coherent and highly collimated) through a process of optical amplification based on the stimulated emission of photons from active medium (solid or gas state) which is excited by a pumping source (flash lamp or other laser) to the amplifying state hence the wavelength of a laser is determined by the medium which emits by electron excitation. The wavelength produced by laser sources determines the color of laser light. Visible light has a wavelength in the range of about 400 nm to about 700 nm. The wavelength of the infrared (IR) is in between 700 nm to 1 mm. In contrary, 10nm to 400 nm of the wavelength is called ultraviolet light (UV). In general, light from a laser has very low divergence thus it can travel very long distances or can be focused by optical lenses with a high energy.

Last two decades the preferred laser in materials science was the carbon dioxide (CO_2) laser with the wavelength at 10.6 µm in the infrared (IR) region, mostly used in automobile industries because IR laser is absorbed by ferrous metals more effectively compared to the non ferrous metals as shown in Figure 1-1. Au, Ag and Cu exhibit sharp absorption edges in visible wavelengths while Al exhibits a low absorption below 100 nm in a wavelength. In this regard, the choice of laser for material processing is basically dependent of the target materials. Beside of the CO_2 laser, the wavelength of the most conventionally used neodymium-doped yttrium aluminum garnet (Nd-YAG) laser is represented. The fundamental wavelength of the Nd:YAG laser has 1064 nm and the series of the wavelengths at second harmonic generation (SHG) and third harmonic generation (THG) are 532 nm and 355 nm, respectively [73].

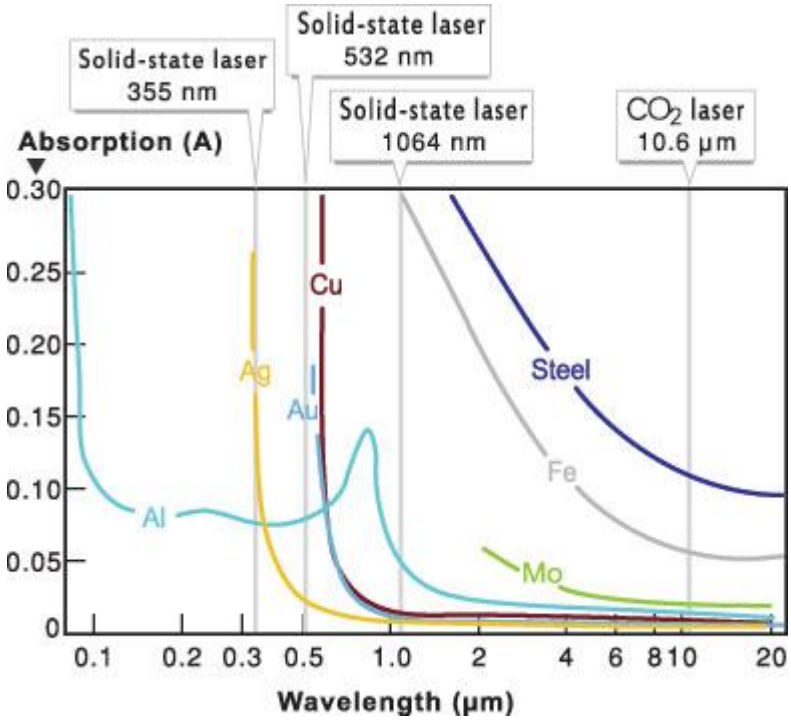

Figure 1-1. Absorption rate of metals as a function of laser radiation wavelength [74].

Basically lasers can be run in two types by operation mode; one is the continuous wave (CW) where the power output is basically continuous and the other is pulsed mode where its output is the form of pulses of light [73].

In contrast to CW, pulsed laser emits light in the form of optical pulses in some duration at some repetition rate (nanoseconds to picoseconds) as simply shown in Figure 1-2. The pulse width is determined at half of maximum amplitude of the pulse [73]. By using focus lenses the laser beam is focused on the target surface and due to the very short pulse duration only the surface of the target material can be evaporated in a small volume of the material by reduced thermal diffusion [75-77]. That allows the using of pulsed laser as a cutting tool not only for micro-machining but also for surgeries in clinical uses. The most widely used pulsed laser system is a Q-switched laser which allows the extremely high power of light pulses than the same laser operating in a CW mode. A Q-switch is an optoelectric or an acousto-optic shutter between the active medium and total reflect mirror in a system that allows the energy to build up in the cavity while lasing action is inhibited in a controlled way and when the shutter is open rapidly, a high peak power is obtained in a short pulse.

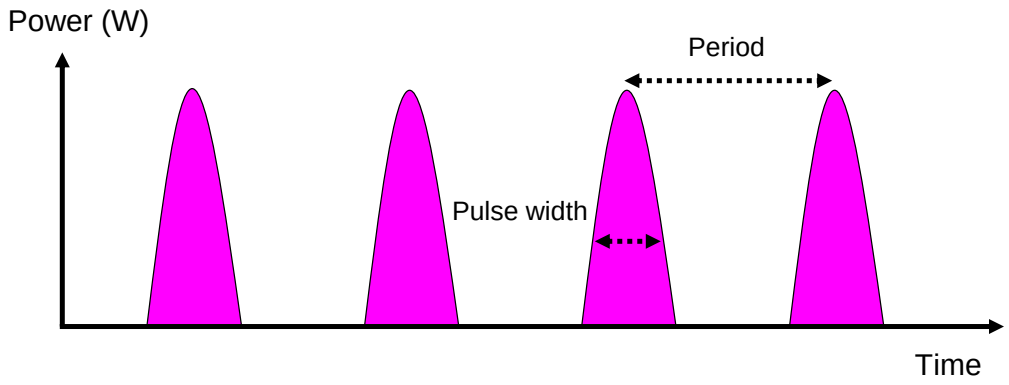

Figure 1-2. A principle of a pulsed mode.

Similar to the pulsed mode, CW laser can be manipulated in accordance to an input signal to be run as a pulsed laser [78, 79]. For example laser operating with a period signal (frequency), simply on and off state, gives an output energy periodically; maximum at on state and minimum at off state, respectively (Figure 1-3). It is called modulated mode and the modulation is generated by a digital signal [79].

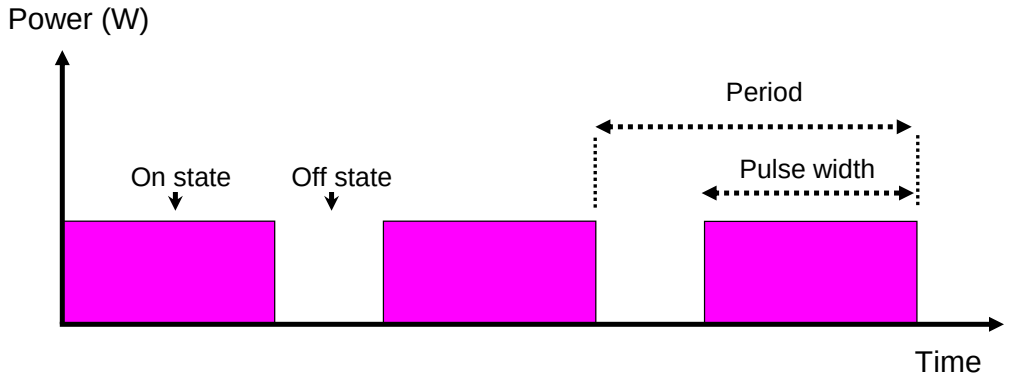

Figure 1-3. A principle of a modulated mode.

2. Experimental approach

In this study, the molecular precursor $[^tBuOAlH_2]_2$ was decomposed and Al/Al_2O_3 nanowires were grown on the heated substrates up to 630°C. Substrates used for the CVD process were borosilicate glasses and stainless steel plates (STS316L). The substrate temperature and the deposition pressure were fixed and always the same precursor $[^tBuOAlH_2]_2$ was used. The precursor flow was regulated by the relative pressure measurement during the CVD process. The substrate temperature was controlled using a thermocouple, which has been calibrated by an optical pyrometer. The gaseous by-products of the thermolysis reactions and any unreacted precursor were removed through the vacuum pump.

2.1 Direct laser writing (DLW)

Direct laser writing (DLW) process is one of the fundamental techniques that focused laser beam irradiating to the target materials where photothermal and/or photochemical reaction occurs. During photo-thermal interaction with metals, light energy is first absorbed by electrons on the metal surface. The excited electrons then move into the deeper parts of the metal, which dissipate the absorbed energy as thermal lattice vibrations, leading to local heated zones. The increased temperatures is easily achieved up to several thousand degree which exceeds the melting or evaporating temperature of the materials [77, 80, 81]. Additionally moving the focal point of laser or materials by a control stage operated with computer aided software cutting, welding, and drilling can be carried out precisely for the metallic and ceramic materials.

The basic set-up of DLW system used in this study is shown in Figure 2-1. A commercially available Ytterbium (Yb) fiber laser (JK100FL: JK Fiber Lasers, United Kingdom) is used with modulated mode (50 kHz). The wavelength of this laser is 1080nm. In this installation, the sample is scanned using a control stage while the position of the laser beam is fixed The laser beam is focused on the deposited Al/Al_2O_3 layer on stainless steel substrate (STS316L, Good Fellow, Germany) which is moveable to X-axis and Y-axis by a control stage. The scanning speed of the stage is 4 mm per second and the moving resolution is 1 µm. The laser beam is focused by a laser head system (company GSI, United Kingdom). The laser head is equipped

with a 76 mm focal length convex lens, which gives a spot diameter of 19 µm at focus. The focused spot is kept on the substrates and the pulse width of the laser is 16µs with energy of 2 W.

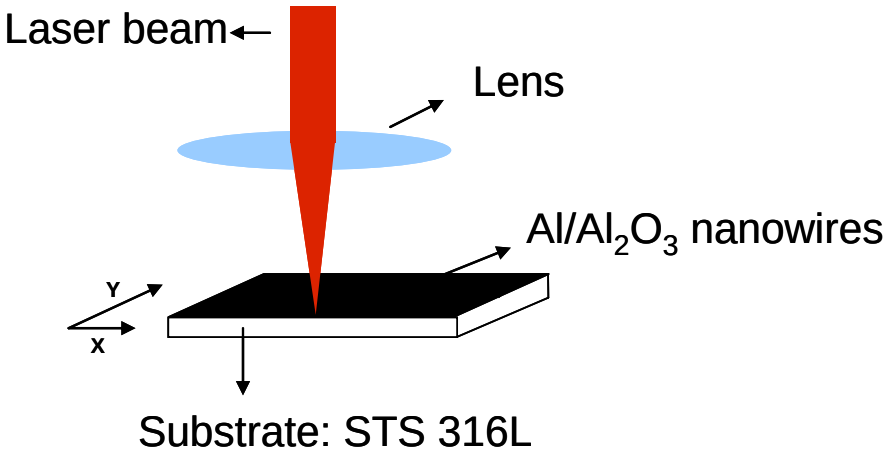

Figure 2-1. Schematic illustration of direct laser writing system.

2.2 Laser interference patterning (LIP)

Laser interference patterning is concerned with the use of interference patterns generated from two or more coherent beams of laser radiation for structuring of materials. Typically, one laser beam is split into two or more beams that are subsequently directed to the target material and the dimensionality of the interference patterns depends on the number of beams (N) which involve in the process. interference among N $\leq$4 produces an N-1 dimensional pattern thus two beam interference patterning provides one dimensional (linear) periodic structures [23, 82]. Figure 2-2 shows the principle of a two beam laser interference technique and the path of laser beams. The laser beam is split through a beam splitter into two equal parts, which are then guided by mirrors and superimposed on the material surface to create linear periodic patterns. The pattern period is basically governed by $\lambda / 2\sin\theta$ derived from Bragg' law, where λ is the wavelength and θ is the incidence angle of the laser beam [23, 83].

In order to create interference patterns with high energy at one pulse, a commercial Q-switched Nd:YAG laser (Quanta-Ray 290: Spectra Physics, USA) operating at

second harmonic (λ=532 nm) with a frequency of 10 Hz and pulse width of 10 ns is used. The beam diameter is 8 mm without focus lens which allows a large area treatment with periodic patterns. All the samples were irradiated at normal atmospheric conditions in air using one single laser pulse.

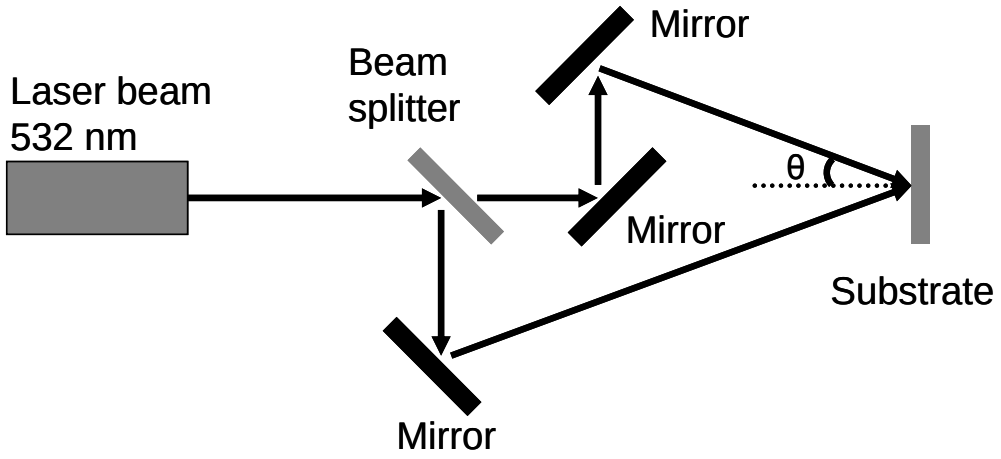

Figure 2-2. Experimental setup of a two-beam based LIP system.

Figure 2-3 shows the basic mechanism of the interference patterning that reveals an intensity distribution oriented by two interfering plane waves. The dotted line represents the fixed threshold (Φ_0), which is the key factor of material process of laser interference corresponds to the ablation of the materials known as the damage threshold [84]. If the fluence (radiative flux integrated over time: $I(r)\Delta t$) is smaller than the Φ_0, the material is not modified (Figure 2-3 (A)) while the material is modified with the greater fluence than Φ_0 as represented in Figure 2-3 (B-D).

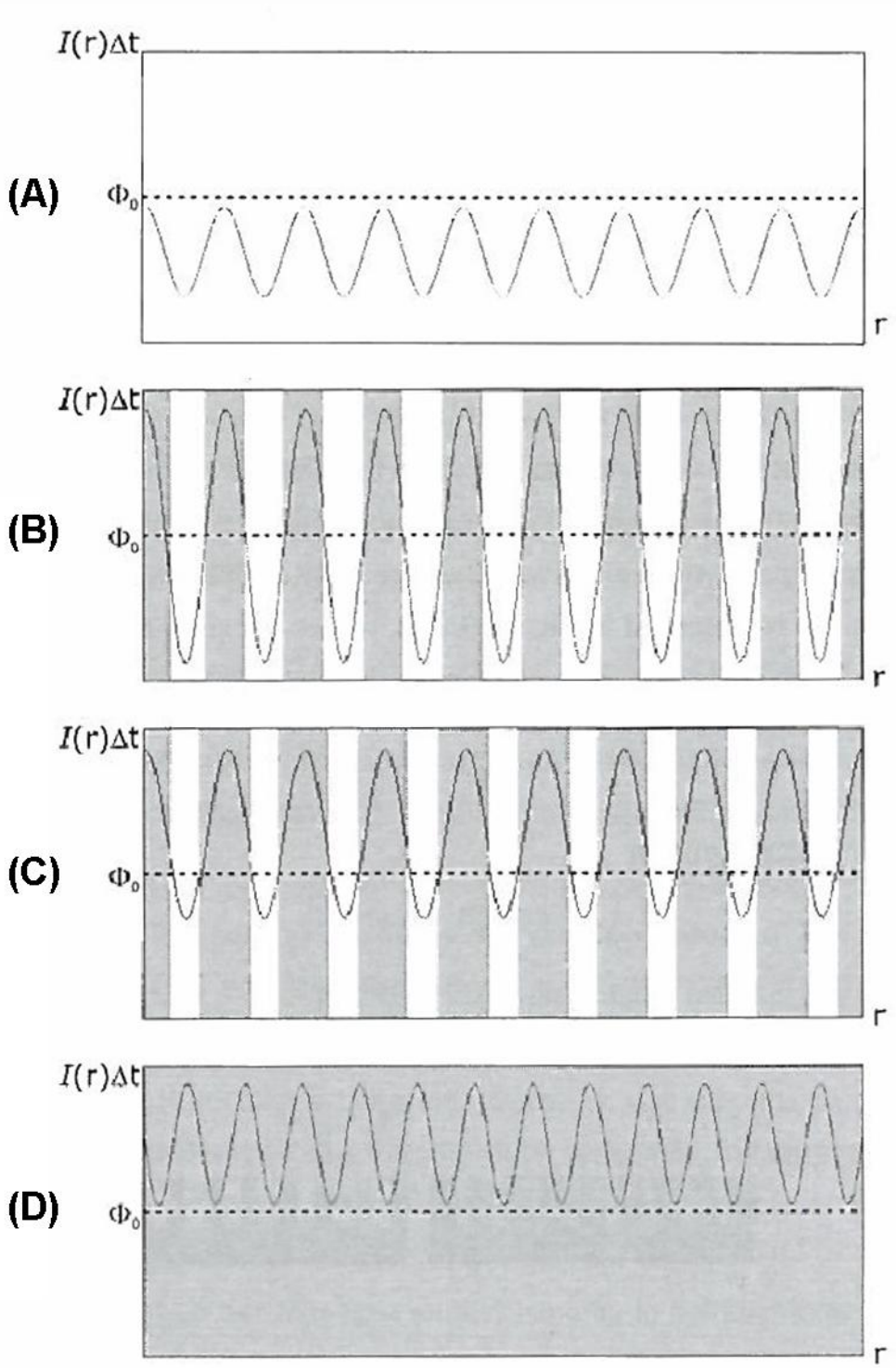

Figure 2-3 Representation of the interference patterns on target material. (A) the fluence is smaller than for any point of the surface, (B-C) the fluence is greater than the required threshold in the grey fringes and the material will be modified in those areas. (D) the fluence is greater than the required threshold of all area of material surfaces thus full surface will be modified [23].

To summarize the laser structuring process with direct writing and interference techniques for this study, the parameters used are given in Table 1.

The changes in surface topography and morphology were analyzed by scanning electron microscopy (SEM, JEOL-JSM-6400F) and an atomic force microscopy (AFM, Nanowizard 3, JPK instruments). Surface chemistry and phase transformation was investigated using an X-ray photoelectron spectroscopy by Mg Kα x-ray radiation (XPS, Omicron) and an X-ray diffractometer (XRD, D-5000, Siemens). Static water contact angle analysis was carried out using a semi-automated and video equipped device (Kruess G2).

Table 1.Laser parameters

	Direct laser writing	Laser interference patterning
Laser system	Yb fiber laser	Nd:YAG laser
Operating mode	Modulated	Q-switched (pulsed)
Wave length	1080 nm	532 nm
Beam diameter	19 µm at focus	8 mm
Pulse width	15 µs	10 ns
Pulse repetition rate	50 kHz	10 Hz
Laser scan speed	4 mm per second	-
Laser power	2 W	0.2 J

3. Results and discussions

3.1 Characterization of structures produced by Direct Laser Writing (DLW)

Prior to create regular lines on the substrates, the pulse rate of the Yb fiber laser was optimized while the speed of the moving stage fixed at 4 mm per second. Figure 3-1 shows the patterns on the deposited Al/Al_2O_3 nanowires layer according to the variation of pulse rate control of 250 Hz, 500 Hz and 50 kHz.

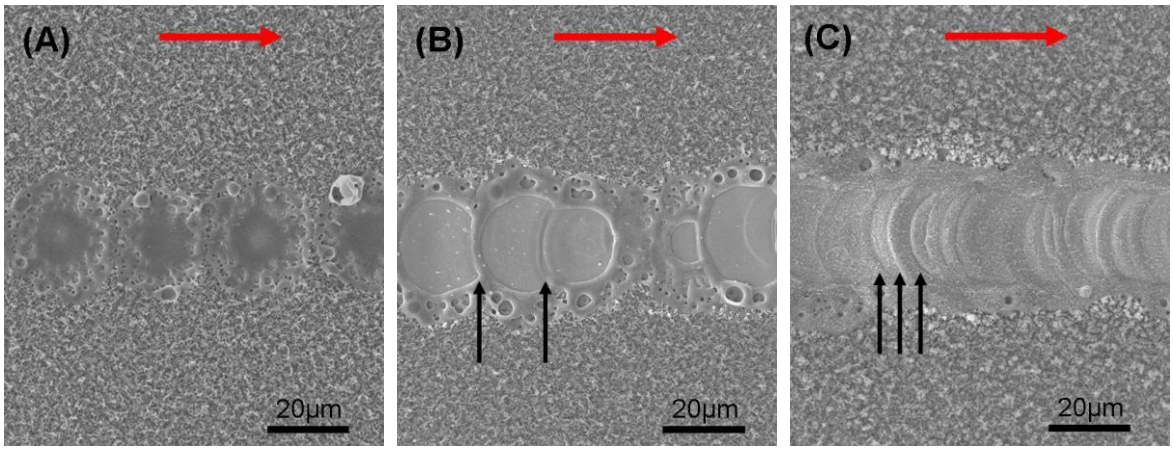

Figure 3-1. SEM images of the laser treated zone with one direction scanning at different pulse rate; at (A) 250Hz, (B) 500Hz and, (C) 50 kHz. The red arrows represent the scanning direction and the black arrows indicate the crescent-like trace marks.

As it can be seen in Figure 3-1 (A), at a low frequency (250 Hz), the treated zone shows separated circular shape as a spot. The diameter of those spots is a good agreement with the laser beam diameter (19 µm at focus). Since laser beam has a Gaussian profile, in the middle of those spots have more flat structure (fully melt and solidify with higher intensity) than the outer of the spots. When the pulse rate was increased double (500 Hz), the spots were started to duplicating and due to this phenomena the trace marks were shown in pre-treated zone as indicated by black arrows in Figure 3-1 (B and C). It is more dominant as shown in Figure 3-1 (C) and treated zone is continuously making a linear channel on the surface resulting in a smooth surface. At a high frequency (50 kHz) crescent like traces were narrow each other even below sub micrometer which reminds of a melt flow, furthermore the width of the treated area was enlarged (Ca. 25 µm) by increased absorbed energy at the surface.

Basically, by use of a modulate laser, a periodical signal (on and off state of laser) so called pulse rate is created. While the pulse rate is increasing, pulse repetition is also increasing. It makes more spots by laser beam on a target material at a same time period. Hence, by using a moving stage with same scan speed in one direction, more spots are created on the surfaces in the same scanning path and if the pulse repetition is high enough, the spots are overlapping. The summary of this mechanism is illustrated in Figure 3-2.

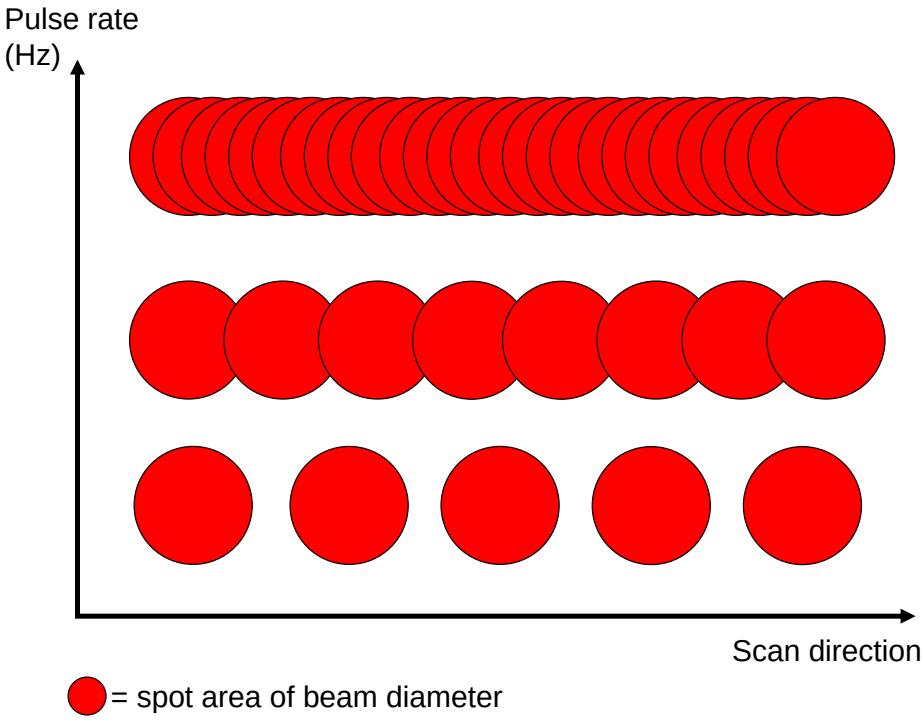

Figure 3-2. Laser spot overlapping step by the variation of the pulse rate at fixed scan speed. The upper, middle and lower red spots represent Figure 3-1 (a), (b) and (c), respectively.

In addition protrusion structures were observed at the boundary of treated region to non treated region. It is due to the convection flow of molten form of Al/Al_2O_3 nanowires by increased temperature gradient. When laser beam is irradiated on the surface the surface temperature increases with an increase in energy density. Thus the temperature of Al/Al_2O_3 nanowires might be easily reached to its melting temperature forming a molten layer, in which lateral temperature gradient exists (higher temperature in the center of molten layer and lower temperature at the border). This temperature gradient induces a vertical convection flow in a liquid state as called thermo-capillary or Marangoni effect [85-88]. Dahotre et al. [89] demonstrated this mechanism sequentially as shown in Figure 3-3. The induced lateral temperature

gradient leads to the formation of a surface tension gradient towards the border of the molten layer and the molten material is thus pulled towards the border of the molten layer where it contacts with the solid phase. Then the material is to pile up at the edge of the pool and cooled down rapidly due to the contact with cold material. Therefore pile up material is accumulated by solidification process and remains at the border.

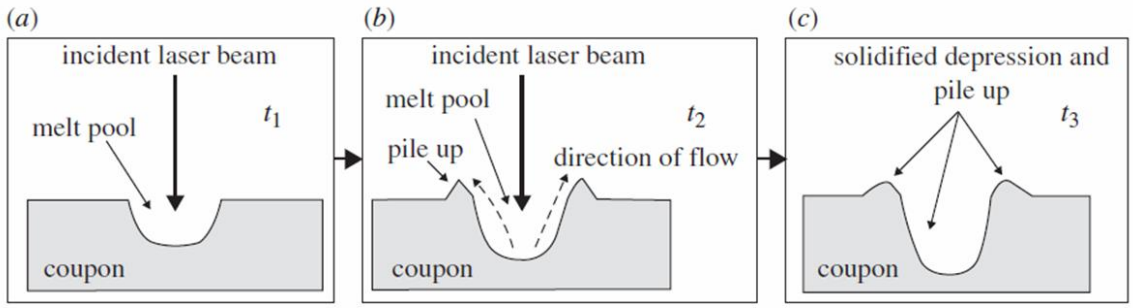

Figure 3-3. The evolution steps of the surface morphology at various times (t1<t2<t3) by a single laser beam [89].

Figure 3-4 shows high resolution SEM images of a channel induced by the DLW process of the modulated Yb laser with a frequency of 50 kHz as shown above in Figure 3-3 (C). Figure 3-4 (B), (C) and (D) are correspond to Figure 3-4 (A) indicating B, C and D, respectively. At a closer look in high magnified SEM image there are at least three different regions where diverse morphologies are observed (Figure 3-4 (A)). In the region of the channel created by laser (Figure 3-4 (B)), the formation of crescent like traces is clearly visible and there are thermal cracks due to the thermal shock caused by periodic laser irradiation inducing rapid heating and cooling rates during the process. Those cracks are formed near to the border and the middle of the channel indicated by red arrows. It is due to the difference in the thermal expansion coefficients of re-solidified layer and the underlying layer. Additionally very small debris (a few nm) are observed on the surface contrast to continuous wave laser treatment of Al/Al_2O_3 nanowires that creates flat surfaces [26]. The debris was caused by a re-deposition effect that is typically created by use of pulse laser systems which is consequence of cyclic ultra-fast heating, ablation and solidification [90]. The profile of the channel is shown in inset of Figure 3-4 (B). As aforementioned, pile-up structures are clearly seen near to the border and the depth of the channel was approximately 1 µm. The width was narrow in the middle of the channel (Ca. 10 µm) compare to the

upper region (Ca. 25 µm). Figure 3-4 (C) shows sub-micron spherical particles near the borders of the channel so called heat affected zone (HAZ). The image was obtained from substrate tilted at 30°. It gives more detailed sub structures which look like micro cracks as indicated red arrow in Figure (A) and (C). However un-deformed Al/Al_2O_3 nanowires can still be seen in beneath. These cracks were formed by densification of Al/Al_2O_3 nanowires forming surface tension induced spherical particles due to the heat conduction from the channel that affect Al/Al_2O_3 nanowires near the borders to be melt and agglomerate via rapid heat transfer from laser irradiated area. Figure 3-4 (D) shows as deposited Al/Al_2O_3 nanowires which were 5 µm far from the channel. It seems that HAZ is not exceeding more than 3 µm (see Figure (A)). One may assume that heat transfer was diminished due to the chaotic nature of Al/Al_2O_3 nanowires which are highly porous and surrounded alumina shell acting itself as an insulator compare to laser treatment of bulk materials [73, 91, 92] and also due to the short laser irradiation time (15 µs) contrast to the result of CW laser treatment on Al/Al_2O_3 nanowires in the thesis of Aktas [26]. In this context a local heat treatment of modulated Yb-laser may lead to the deformation of Al/Al_2O_3 nanowires without destroying or deforming of underlying substrate by an excessive heat transfer.

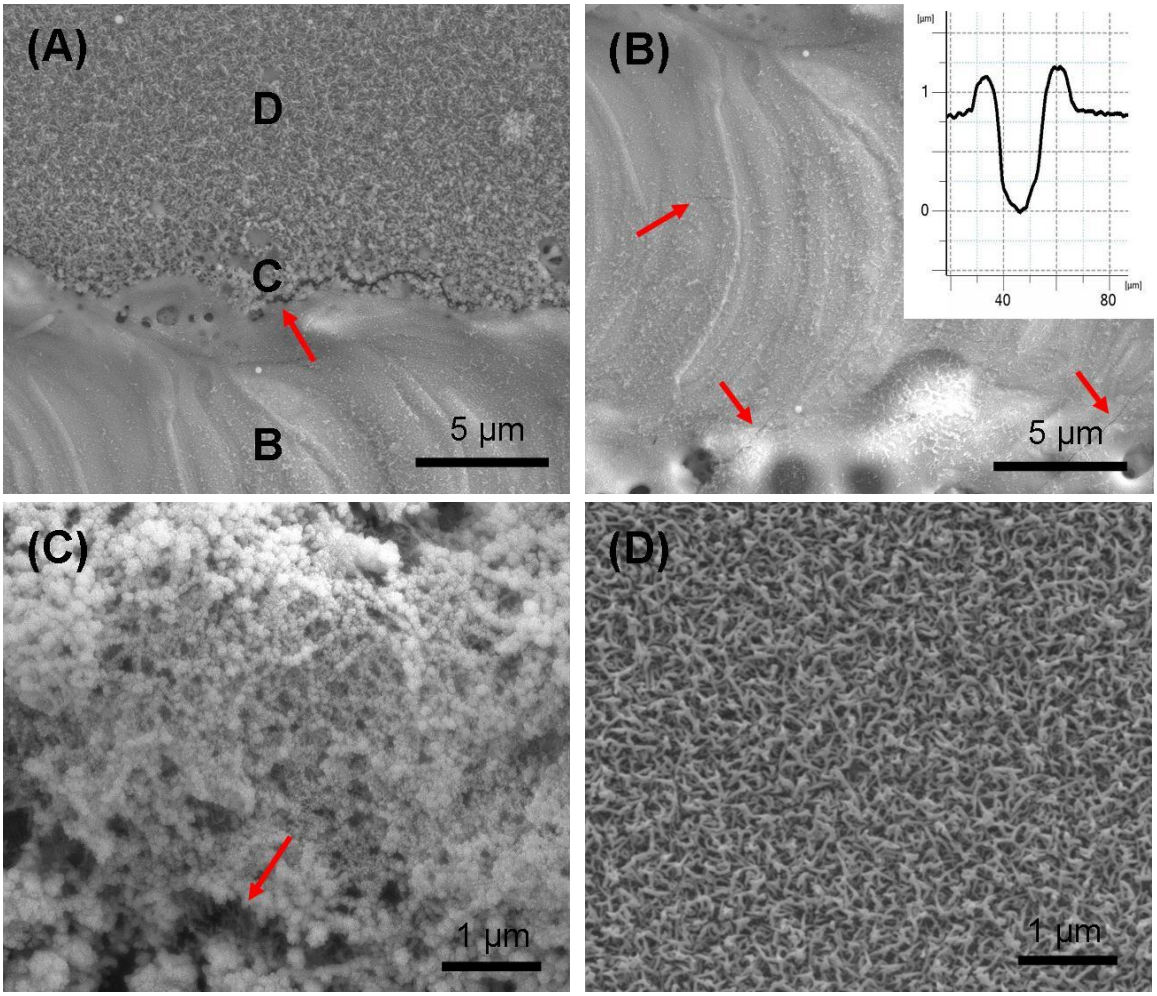

Figure 3-4. SEM images at higher magnification; (A) overview of the region of interest, (B) treated zone (inset is the profile), (C) Heat affected zone (HAZ) tilt at 30°, and (D) untreated zone. Red arrows indicate cracks

Since the laser treatment on Al/Al_2O_3 nanowires induced re-solidification process, it is obvious that the laser beam induces local changes especially near surfaces which can be attributed to the oxidation of Al cores and oxide phase transformations of Al/Al_2O_3 nanowires. Thus the phase transformation of Al/Al_2O_3 nanowires is investigated by XRD. Prior to the measurement substrate was partially treated by laser. Figure 3-5 (A) shows as deposited Al/Al_2O_3 nanowires on STS316 and Figure 3-5 (B) shows laser treated substrate and treated area is 4 mm^2, as indicated by the red arrow.

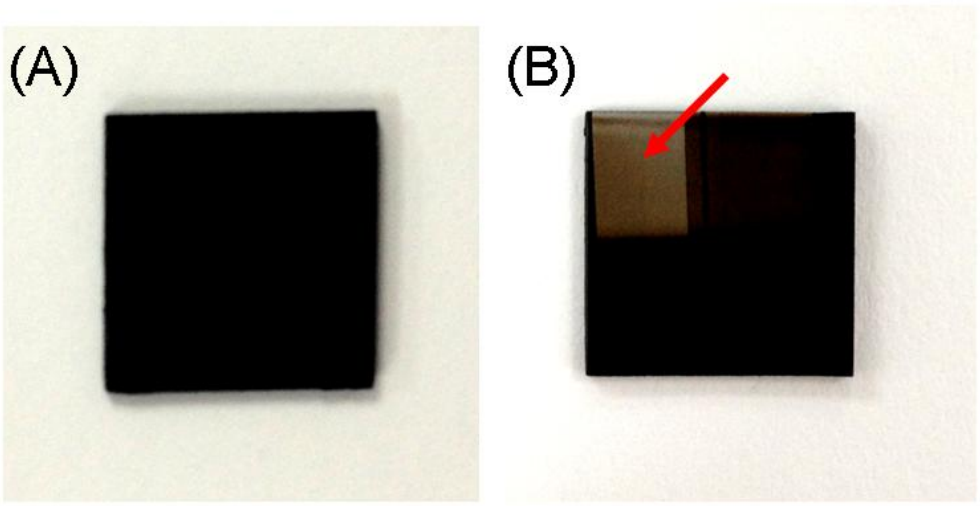

Figure 3-5. (A) Al/Al_2O_3 nanowires on STS316 and (B) Laser treated substrate. The red arrow indicates treated region having a color of brown from black.

Figure 3-6 shows XRD diagrams of laser treated Al/Al_2O_3 nanowires on STS316L substrate. As it is shown that after laser treatment, Al/Al_2O_3 nanowires were transformed to alpha alumina (α-Al_2O_3). The corresponding peaks of α-Al_2O_3 are given in Table 2.

Table 2.The peaks of alpha alumina defined by XRD

2θ (°)	25.58	35.15	37.78	43.36	52.55	57.5	61.3	66.21	68.21	76.87	77.22
hkl	012	104	110	113	024	116	018	214	300	1010	119

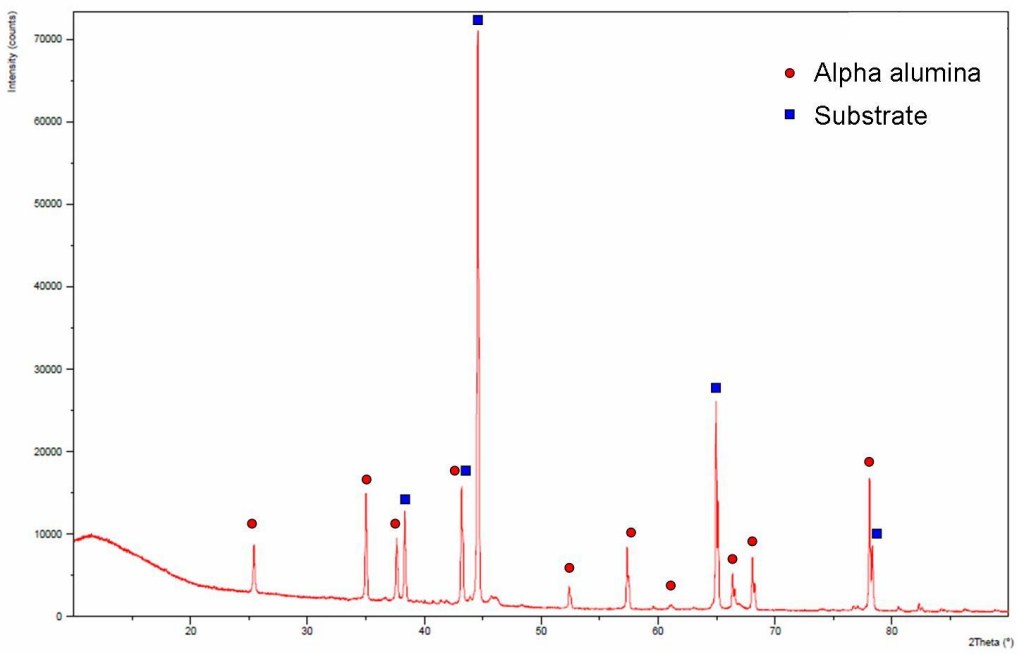

Figure 3-6. XRD spectrum of laser treated surface.

Previously Veith showed first the α-Al_2O_3 transformation of Al/Al_2O_3 nanowires by CO_2 laser treatment [93] and later on crack free α-Al_2O_3 from Al/Al_2O_3 nanowires by use of argon laser have been introduced. [94]. As shown there, the mechanism of the transformation of Al/Al_2O_3 composite to α-Al_2O_3 is due to the combination of the heating by laser and the combustion of Al core by oxidation. According to the literatures, the reaction progress is also described as

$$Al/Al_2O_3 + 3/4\ O_2 \xrightarrow{Laser} 3/2\ \alpha\text{-}Al_2O_3$$ [26, 32]

In fact, laser treatments induce heating of those core/shell nanowires. When the temperature reaches over the melting point of Al, metallic Al core will melt and the volume is increased up to 6% due to the density changes from 2.7 g/cm^3 at solid phase to 2.4 g/cm^3 at liquid phase. This induces an internal pressure which is a driving force to destroy the Al_2O_3 shell then Al core will contact with oxygen since the laser treatment is performed at ambient condition. This reaction is highly exothermic (enthalpy ΔH is -1675 kJ/mol [95]). The reaction coordinate was schematically given by Veith [93] as shown in Figure 3-7 where E_A is the activation energy needed to destroy the Al_2O_3 shell and -ΔH is the enthalpy of the oxidation reaction of Al core.

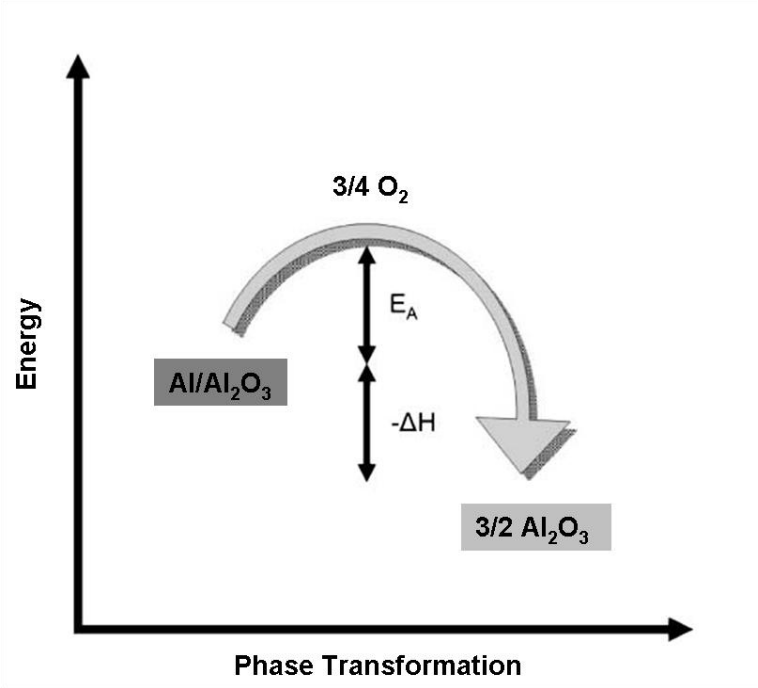

Figure 3-7. Reaction coordinate of the transformation of Al/Al_2O_3 composite to Al_2O_3 [93].

Subsequently continuous channels were produced by altering the distance of each other while laser parameters were kept constant. Figure 3-8 shows the substrates having the channels created with an interval (distance between a channel and another) of 50 µm (A), 100 µm (B) and 200 µm (C), respectively. In addition to the primary micro-scale channels, between two parallel channels the surface is composed of Al/Al_2O_3 nanowires which are few tens of nm in diameter. Although the channels by laser are accounted as microstructures, the non treated areas are still remaining as nano-scale structures.

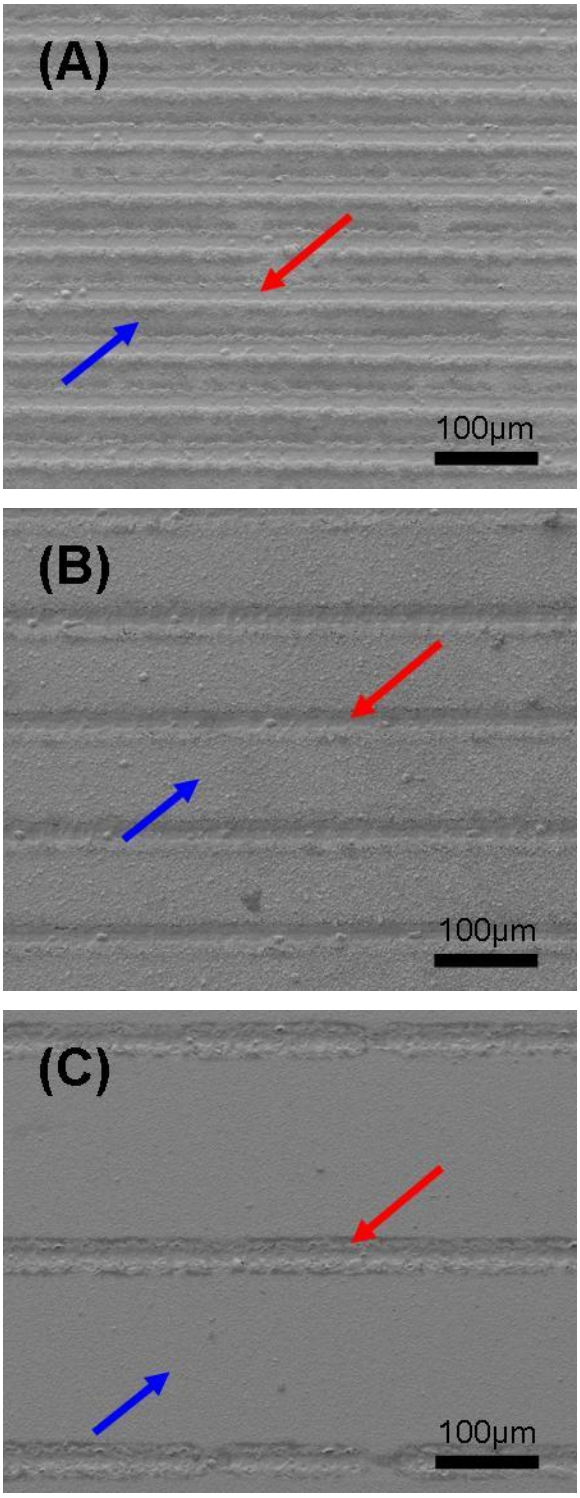

Figure 3-8. SEM images of DLW patterned substrates with different interval of (A) 50 μm, (B) 100 μm, and (C) 200 μm. Red arrows indicate laser treated region and blue arrows indicate non treated Al/Al_2O_3 nanowires.

3.2 Contact angle measurement of sessile drop

The measurement of contact angle using distilled water drop was carried out using Contact Angle Measuring System G2 (Krues GmbH, Germany) combined with by Drop Shape Analysis software at room temperature. Especially, when substrates have channels, anisotropic wetting behavior was observed as shown in Figure 3-9. Water drop has spread parallel to the channels more than orthogonal direction thus contact angles were measured both in orthogonal and in parallel direction to the channels as illustrated in Figure 3-10.

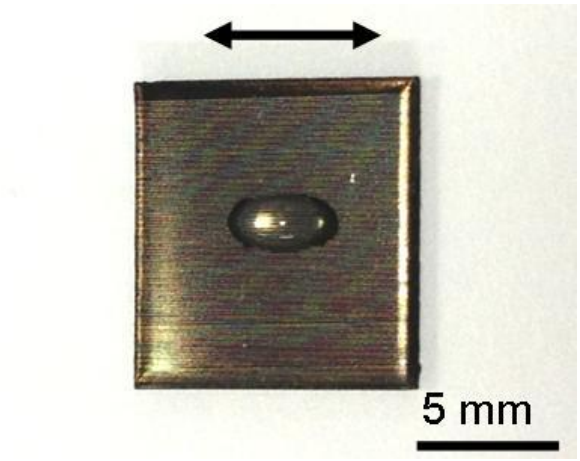

Figure 3-9. Anisotropic water contact on patterned surface at top view. The arrow indicates parallel direction to the channels.

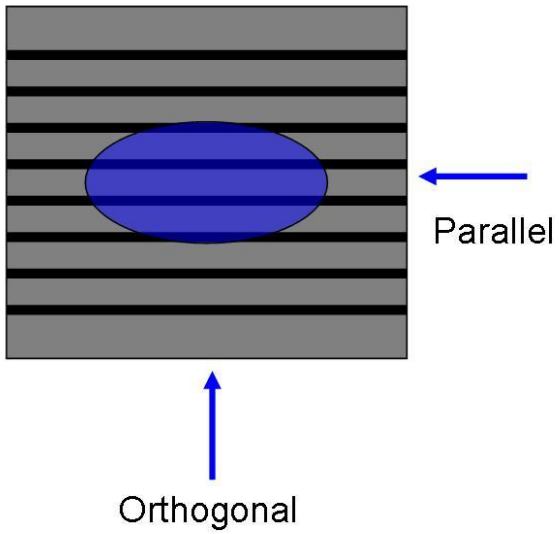

Figure 3-10. The direction denoted as orthogonal and parallel to the patterns are indicated by arrows.

The contact angle is the angle at which a liquid/vapor interface meets the solid surface. The contact angle is specific for any given system and is determined by the interactions across the three interfaces. The shape of the droplet is determined by the Young relation [96] which assumes a perfectly flat and rigid surface. Most often used concept is illustrated with a small liquid droplet resting on a flat horizontal solid surface as shown in Figure 3-11. Consider a drop of liquid on a solid substrate which can be characterized by: $\gamma GS = \gamma SL + \gamma LG \cdot \cos\theta$. Here γGS, γSL, and γLG are the surface tensions (or surface energy) of gas-solid, solid-liquid and liquid-gas interface, respectively and θ is the contact angle of the liquid with respect to the solid substrate surface.

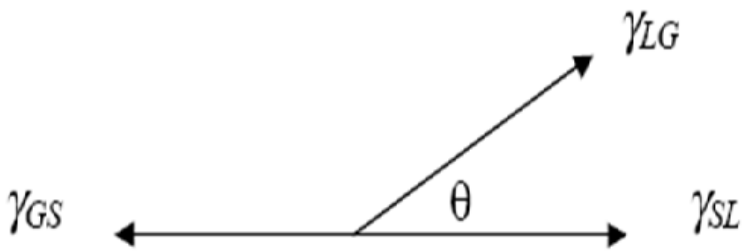

Figure 3-11. Contact angle and surface tension.

The wetting characteristic of the surface can be generally described as; θ = 0 complete wetting, 0 < θ < 90: partial wetting, and θ > 90: non-wetting where θ is the contact angle. So the contact angle is a very useful inverse measure of wettability, as a smaller contact angle implies smaller surface tension, but higher surface wettability [97]. However surfaces in many cases are far from this ideal situation and contact between liquid droplets and solids is controlled by adhesive, capillary and other forces, the balance of which determines the regime of wetting [98]. Thus Wenzel's model dealing with a homogeneous wetting regime and Cassie-Baxter's model dealing with a heterogeneous regime were introduced for rough and porous surfaces, respectively [99, 100]. The Wenzel model reveals the whole sample to be wetted such that the droplet is in complete contact with the surface. Conversely, the Cassie-Baxter model reveals the droplet to rest on the roughened surface forming air-gaps between the droplet and the surface. The schematic explanation of each model including its mixture model is shown in Figure 3-12.

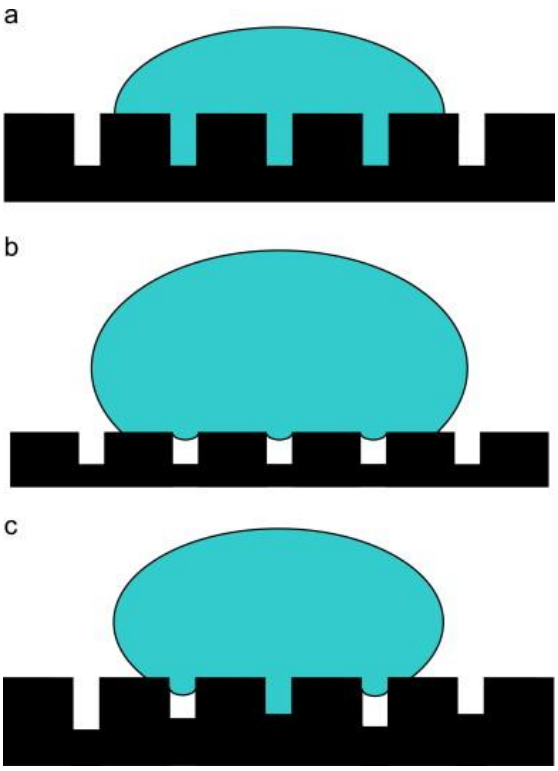

Figure 3-12. Schematic illustration of (a) Wenzel, (b) Cassie-Baxter, and (c) Mixed model [101].

The measured wetting angle is shown in Figure 3-13. The measurement of contact angle was repeated 10 times per each substrate type. Contrast to the wetting angle of as deposited Al/Al_2O_3 nanowires, the substrates with channels show very hydrophobic wetting behavior. The highest wetting angle (122°) is shown on the substrate with the 50 µm periodic channels at parallel direction. Actually this wetting behavior does not agree with Wenzel model in which the contact angle should decrease with increasing surface roughness for initially hydrophilic materials. It seems that water drop on the DLW patterned surfaces is governed by Cassie-Baxter or mixed model.

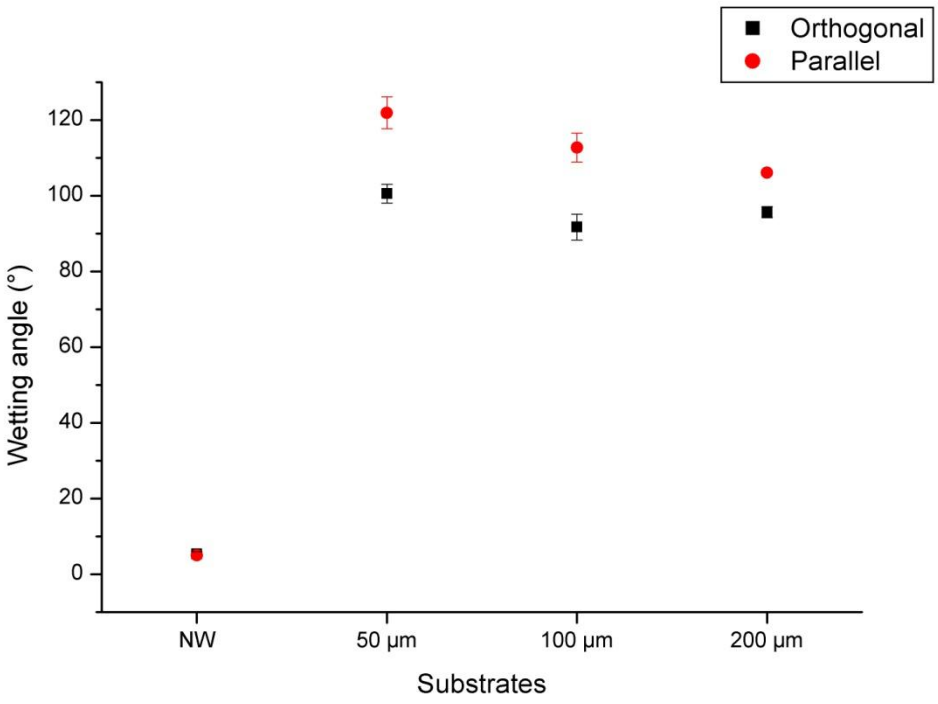

Figure 3-13. Water contact angle of as deposited and DLW patterned Al/Al_2O_3 nanowires. 50 µm, 100 µm and 200 µm in X axis represent the spacing of the channels created by laser on Al/Al_2O_3 nanowires layer.

As shown in Figure 3-9, it is believed that the linear channels on the substrates give rise to anisotropic wetting properties, which lead to different spreading behavior of water droplet in orthogonal and in parallel directions because the edges of the channels may provide a location for the pinning of the liquid-solid-vapor interfaces as shown in various reports [102-104]. Recently Hans et al. showed a mechanism of a perpendicular contact-line pinning on a sharp edge of periodically created linear structures [105]. It can be an explanation how an increase in contact angle was observed on the laser patterned substrates. When water droplet is prohibited to spread in orthogonal direction, subsequently it spread in parallel where it may penetrate into the channels and Al/Al_2O_3 nanowires layer. Thus the latter result in an equilibrium shape of the droplet on the surface which is ellipsoid. In this context the morphology of linear structure plays a significant role in establishing the anisotropy of the surface wetting.

Keep this in mind, the pinning effect on patterned substrate was estimated. Simply the amount (volume or mass) of the water droplet on the substrate was increased by a manual control. Figure 3-14 shows the water droplet behavior on the substrate having the channels at the period of 50 µm. Wetting angle was measured in parallel

direction where pinning effect is observed. As it can be seen, the first stage of the water contact is shown on the top of the image and then following images show how water droplet behave at an increased water amount. The blue dotted line 1 and 2 reveal the contact area of the water droplet on the substrate surface. While the amount of the water was increasing, contact area was kept constant. It gives higher wetting angle than small droplet. On the other hand, the contact area of the water droplet was increased when the amount of the water reached certain value as indicated by blue dotted line 3. In this case, water droplet cross the channels and the wetting angle was decreased. It means conversely, that more channels prohibit more the wettability due to a larger energy barrier along the orthogonal direction to the channels. In this context it is clear that how the substrate with 50 µm periodicity in channels repetition (highest channel density) shows more hydrophobic behavior than the other prepared samples. Likewise the substrate with 100 µm periodic channels showed more hydrophobicity than substrate with 200 µm periodic channels which has the minimum channel density.

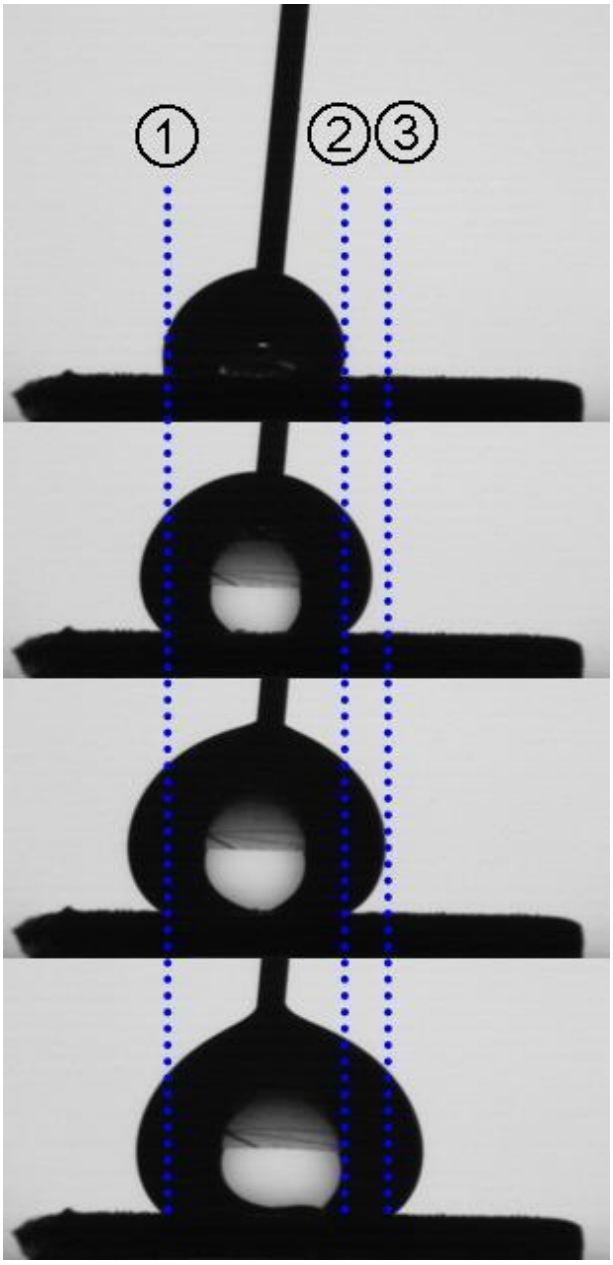

Figure 3-14. Wetting behavior of a water droplet steadily increasing in volume on patterned substrate. Blue dotted lines 1, 2 and 3 exhibit the edge of the water droplet on the surface.

Many reports showed that anisotropic wetting can be observed by chemical gradients alternating hydrophilic and hydrophobic stripes with dimensions in the low-micrometer range [102]. Also super hydrophobic surface from hydrophilic surface was introduced by combination pattern with hydrophobic coatings such as silane or fluorinated agent [106-108]. In contrast to those reports, increased wetting angle of Al/Al_2O_3 nanowires layer was observed by only altering the surfaces topography without using any chemical modifications.

3.3 Characterization of structures produced by Laser Interference Patterning (LIP)

Al/Al_2O_3 nanowires were deposited on glass substrates by CVD of a single source precursor (SSP) $[^tBuOAlH_2]_2$ at elevated temperatures. Round shaped borosilicate glass slides (diameter of 12 mm, Carl Roth, Germany) were used as substrates. The surfaces of Al/Al_2O_3 nanowires irradiated with constructive interference of laser beams undergo melting and subsequently re-solidification as schematically shown in Figure 3-15. As one can depict from the schematic drawing, Al/Al_2O_3 nanowires have an oxide shell (grey color) and an Al core (yellow color). Following the selective heat treatment, Al core seem to melt. The Al_2O_3 shell is then cracked due to the internal pressure caused by phase transformation of Al core (solid to liquid). Subsequently oxygen diffuses into the nanowires resulting of oxidation of Al core which is transformed to Al_2O_3. This reaction is highly exothermic and remarkable as described in chapter 3.1. In both cases outer surface chemistry seems to stay identical. Contrast to the modulated Yb-laser, Laser Interference Patterning (LIP) was carried out with a very short time pulse rate of 10 ns. It makes slowness of heat transfer in a certain volume of material thus only upper region of deposited nanowires were mostly modified. It leads nano/micro porous layer while the Yb-laser created flat cast layer on the substrates.

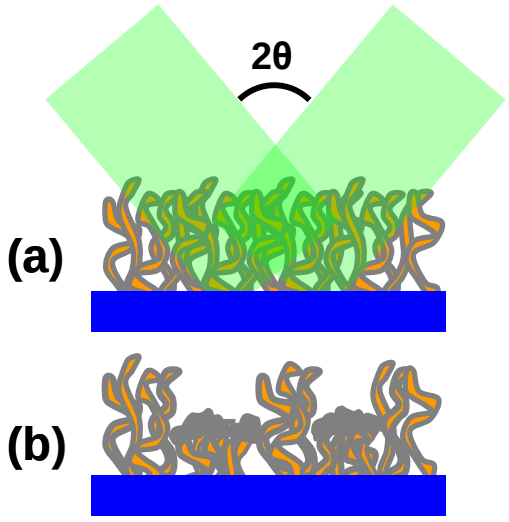

Figure 3-15. Illustration of LIP process on deposited Al/Al_2O_3 nanowires.

As shown in Figure 3-16 (a), biphasic core/shell Al/Al_2O_3 nanowires exhibit a chaotic nature. Figure 3-16 (b) shows SEM image of patterned nanowires at incidence angle of 3.8°.which creates 2 µm periodic linear patterns. In Figure 3-15 (b) it is clearer since non altered nanowires were still seen in the beneath of porous re-solidified layer. At regions subjected to a non-constructive interference, hill-like structures composed of globular and wire-like structures were observed. When the high energy laser pulse heats nanowires locally, it seems that a high lateral temperature gradient forms and this induces also a gradient of surface tension. It is known that such a high gradient forces movement of the molten particles to the periphery of the non-exposed (less heated) areas [109]. This leads to the formation of nano-porous and globular particles due to a fast re-solidification with minimized surface energy at the boundary of the solid material.

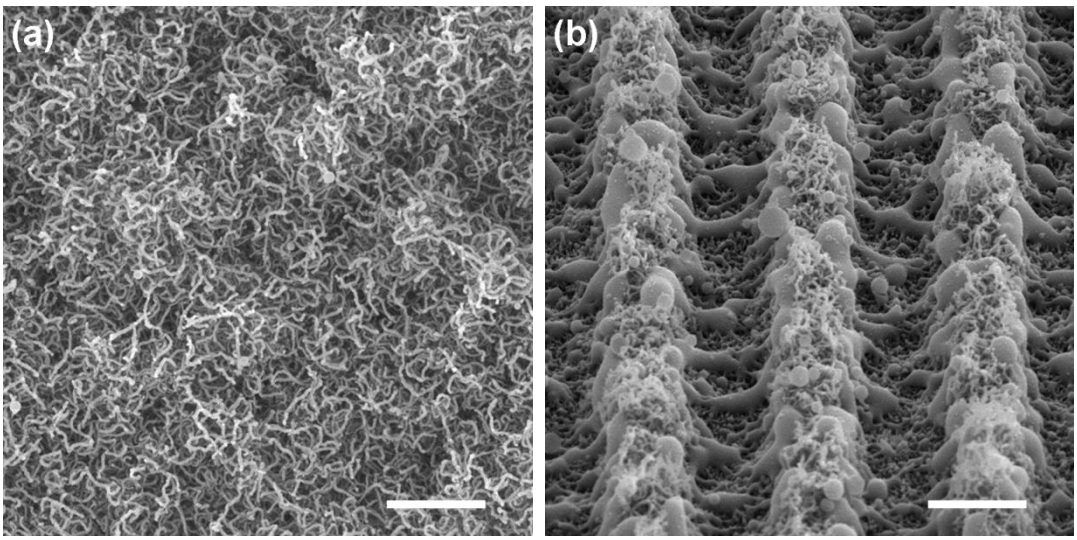

Figure 3-16. SEM images of Al/Al_2O_3 nanowires (a) before LIP and (b) after LIP (Scale bar is 1µm).

Contrast to the DLW treated substrates, LIP patterned substrates show rainbow colors under the sun light (Figure 3-17). This is because of the light diffraction from the periodic patterns which acts as a diffraction grating[110]. In general, diffraction gratings split the monochromatic light such as laser beam into several beams which are called diffraction orders indicated as “m”. This light separation is related to the incoming and diffracted angle of the light from the periodic patterns and it can be expressed as: “$m\lambda = d(\sin\alpha + \sin\beta)$”, where λ is the wavelength of incident light, d is the spacing of the grating (in this case, periodicity), α is the incident light angle, and β is the angle of the diffracted light. Especially, these periodic structures separate the

wavelengths of a broadband light source. As it can be seen in Figure 3-17, when the incidence angle keep identical, diffraction angle will be varied according to the wavelength of the incoming light. Therefore, broadband light sources such as sun light is separated by the periodically patterned surfaces and it can be easily seen at a visual wavelength by human eyes.

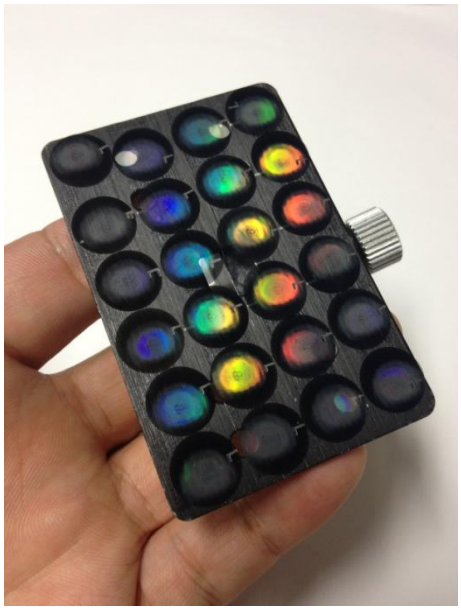

Figure 3-17. Light reflection on LIP modified surfaces.

Prior to cell culture experiments, four different linear patterns with periodicity of 1 µm, 2 µm, 4 µm and 8 µm were prepared by simply altering the incidence angle of laser beams at 15.2º, 7.6º, 3.8º and 1.9º, respectively. Figure 3-18 shows the SEM images of the patterned Al/Al_2O_3 nanowires at different incidence angles of laser beams. At higher magnification Images were obtained from LIP treated substrates at tilt angle of 52° as shown in Figure 3-19. Porous re-solidified zone by LIP and Al/Al_2O_3 nanowires can be clearly seen.

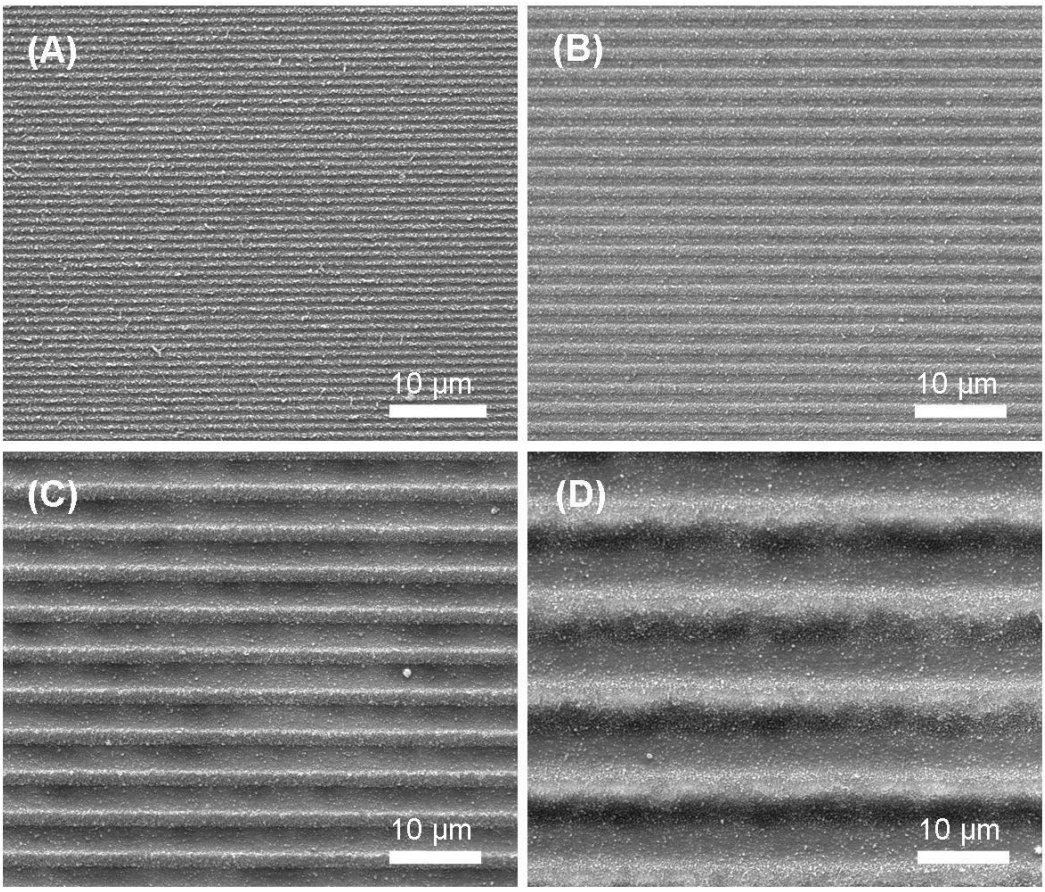

Figure 3-18. Low magnification SEM images of the substrates treated by LIP at period of (A) 1µm, (B) 2µm, (C) 4µm, and (D) 8µm.

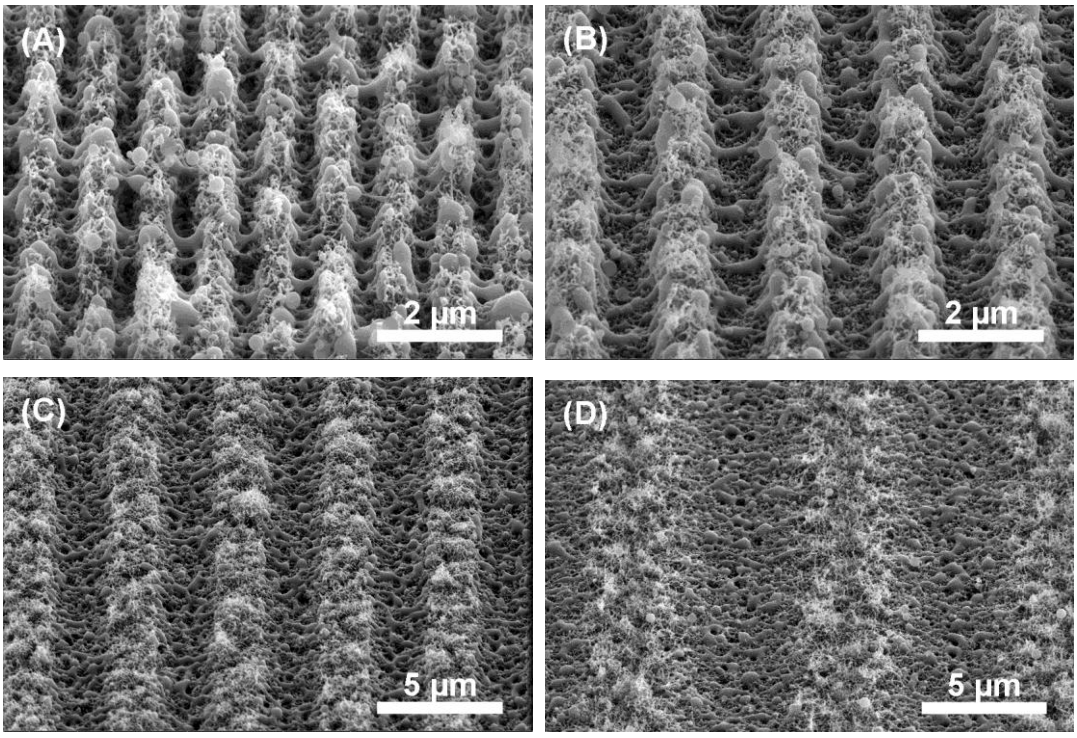

Figure 3-19. High magnification SEM images of the substrates treated by LIP at period of (A) 1µm, (B) 2µm, (C) 4µm, and (D) 8µm. Images were obtained from the substrates tilt at 52°.

In order to measure the depth of the channel induced by LIP, the substrates were prepared by focused ion beam cutting which gives direct observation of the structures at cross view. The depth of these structures was in a range of Ca. 300-650 nm. As it can be seen in Figure 3-19 (A) and 3-20 (A), (at the periodicity of 1 µm), the channels were not clearly separated from each other and they show irregular depth profiles. The depth of the channels of the substrates with larger periodicity shows similar scale in Figure 3-19 (B), (C) and (D). This deviation at a narrow periodicity can occur due to the chaotic nature of Al/Al_2O_3 nanowires since such multi-component and randomly distributed structures are known to exhibit some non-linear optical effects and also irregular thermal conductivity.

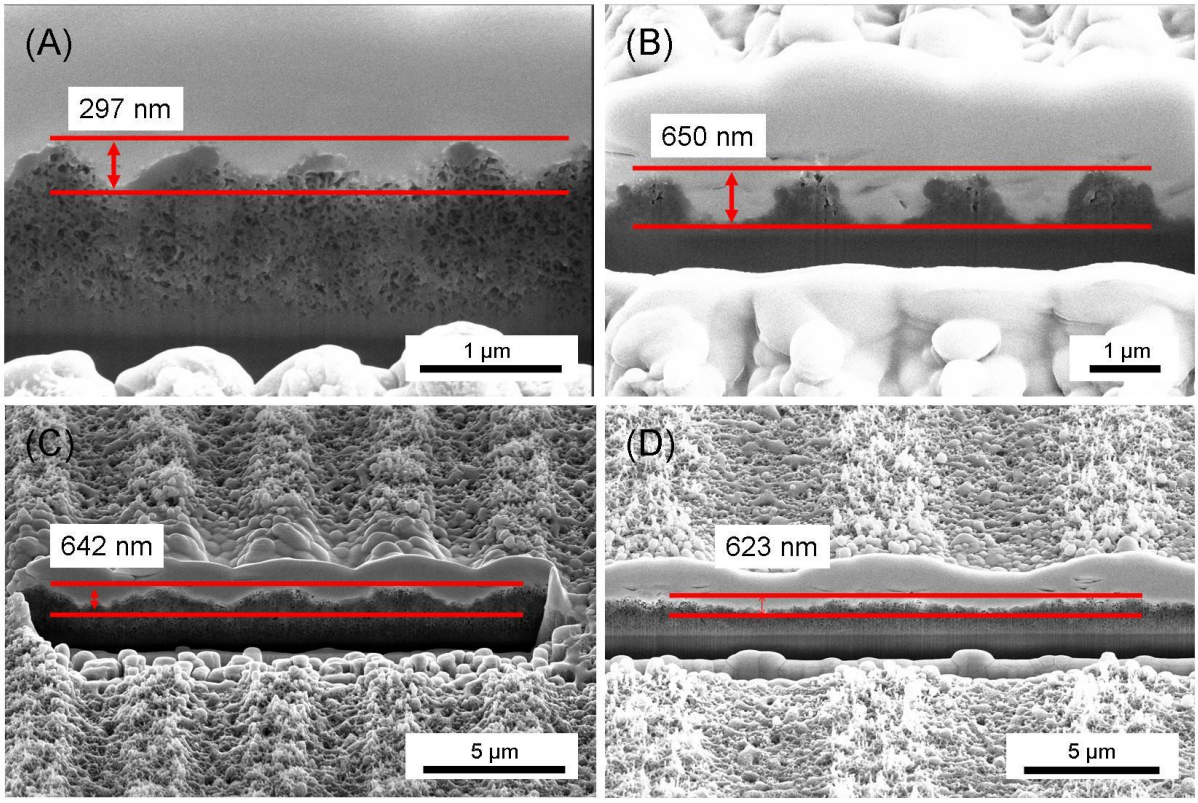

Figure 3-20. Cross section of the substrates treated by LIP at period of (A) 1µm, (B) 2µm, (C) 4µm, and (D) 8µm.

3.4 Wetting behavior of the LIP treated substrates

As shown in Figure 3-21, while as-deposited Al/Al_2O_3 nanowires layer shows quite hydrophilic nature, after LIP a more hydrophobic behavior was observed. Water contact angle was measured 10 times per each type of the samples. Bhushan et al. showed such an increase in the wetting angle on micro patterned surfaces composed of nano-fibers [111]. More similarly Yang et al. showed that laser interference induced periodic patterns alter the surface contact angle enormously from hydrophilic to hydrophobic [112]. In addition an anisotropic wetting was also observed on patterned nanowires. Similarly to the DLW treated substrates, water droplets exhibit an elongated shape parallel to laser induced channels. This is because a water droplet is blocked by discontinuous structure of Al/Al_2O_3 nanowires layer in orthogonal direction and the momentum of the water droplet is then consumed in parallel direction. It is assumed again that the increase of the contact angle might be due the hierarchical structures composed of micro and nano scale features and pinning effect is also encountered.

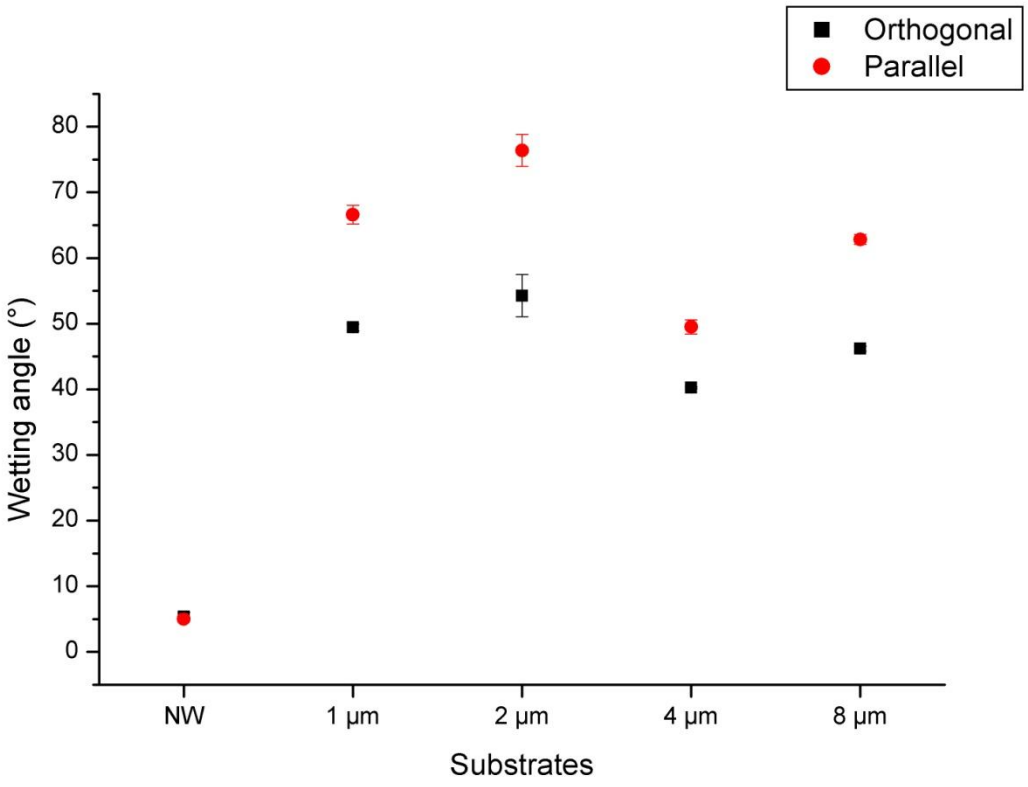

Figure 3-21. Water contact angle of as deposited and LIP treated Al/Al_2O_3 nanowires. 1µm, 2µm, 4µm and 8 µm of X-axis represent the periodicity of the laser induced channels.

3.5 Surface chemical analysis of LIP treated substrates with XPS

To examine surface chemical nature of the substrates, XPS was used. XPS spectra of as-deposited and LIP treated Al/Al_2O_3 nanowires show similar results as shown in Figure 3-22. The species of aluminum, carbon and oxygen can be seen clearly in full spectra of all substrates. Given in the reference [113], the binding energies at 531.6 eV, 72.65 eV and 74.7 eV represent for O 1s, Al^0, and Al^{3+}, respectively. The peak of Al 2p from as deposited Al/Al_2O_3 nanowires was 74.2 eV, which corresponded to the Al^{3+} state. After the LIL treatment, Al 2p at 75 ± 0.6 eV was observed which also indicates clearly the oxidized Al state, Al_2O_3. In bulk aluminum it could be possible to detect two aluminum peaks at Al 2p from metallic aluminum (Al^0) and aluminum oxide (Al^{3+}). The present carbon seems to be accumulated from the system (ex. Oil from the pump or sealing oil from the vacuum chamber).

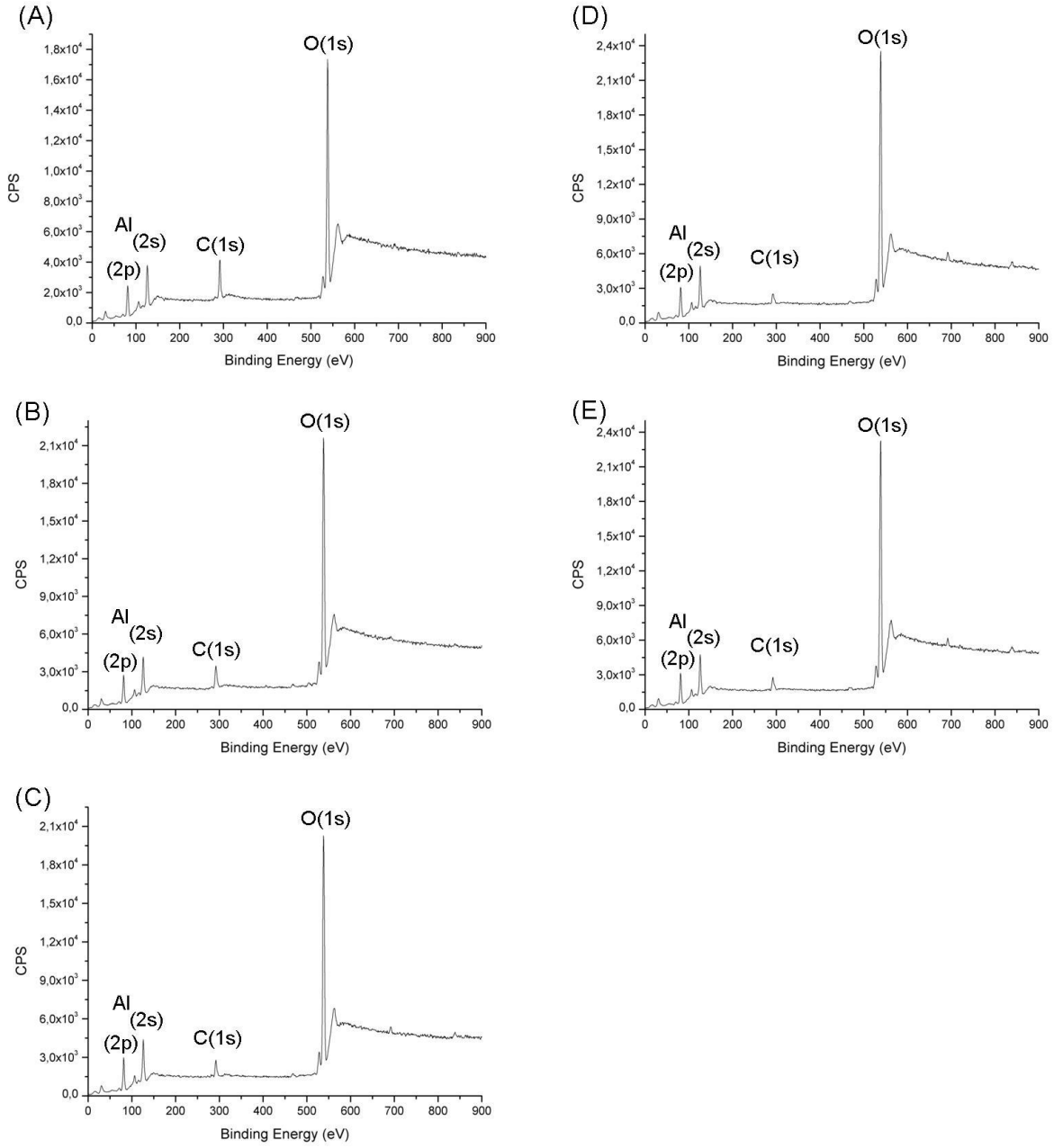

Figure 3-22. XPS spectra of (A) as deposited and LIP treated Al/Al_2O_3 nanowires at period of (B) 1 µm, (C) 2 µm, (D) 4 µm and (E) 8 µm.

The measured surface chemical composition of the substrates was summarized in Table 3. As it can be seen, the oxygen was slightly increased due to the oxidation of Al core exposed to the air since LIP treatment was carried out at ambient condition. Furthermore the carbon content was decreased significantly by LIP treatment. It indicates that detected carbon was contamination from the outside. Therefore two-beam LIP provided linear periodic patterns on the Al/Al_2O_3 nanowires and XPS investigation showed that as-deposited and LIP treated Al/Al_2O_3 nanowires exhibit identical chemical state of the surfaces. It is believed that the core-shell Al/Al_2O_3 nanowires act as a self-healing material. Following the laser treatment Al core seems to melt and oxidize. In this context, as-deposited and laser treated surfaces exhibit always the same outer chemical state, Al_2O_3. Such surfaces are ideal for studying the direct topography effect on cell-surface interaction independent from the surface chemistry because the initial stage of cellular responses on surfaces is governed by surface chemistry [114].

Table 3. Surface chemical composition of the substrates by XPS

Substrate	Al (at.%)	O (at.%)	C (at.%)	Atomic ratio Al:O
Al/Al_2O_3 nanowires	21.4 ± 0.2	59.3 ± 0.4	19.3 ± 0.1	2.8
LIP period of 1 µm	21 ± 0.2	62.7 ± 0.5	16.3 ± 0.4	3.0
LIP period of 2 µm	25 ± 0.4	63.7 ± 1.1	11.3 ± 0.2	2.6
LIP period of 4 µm	23.6 ± 0.4	65.6 ± 1.2	10.8 ± 0.2	2.8
LIP period of 8 µm	22.9 ± 0.3	67 ± 0.9	10.1 ± 0.1	2.9

On the other hand, there was no relevant factor with increased wetting angle of the substrates and it did not show a clear tendency. Moreover as shown in Table 4, the effect of surface oxygen content and the roughness are not conclusive and it seems that the induced topographical patterns (nano-micro features) can be the dominating factor in this instance. It should also be noted that the XPS data showed no other elements present before or after the laser treatment, except aluminium and oxygen which are the main constituents of Al/Al_2O_3 nanowires.

Table 4. Mean roughness, oxygen content and water contact angle

Substrate	Ra (nm)	O (at.%)	Water contact angle (degree)		Δ°
			Orthogonal	Parallel	
Al/Al_2O_3 nanowires	48	59. 3	5.4 ± 0.6	5.1 ± 0.3	-
LIP period of 1 µm	73	62.7	49.4 ± 0.5	66.6 ± 1.4	17
LIP period of 2 µm	167	63.7	54.3 ± 3.2	76.4 ± 2.4	22
LIP period of 4 µm	186	65.6	40.2 ± 0.2	49.5 ± 1.1	9
LIP period of 8 µm	224	67	46.2 ± 0.4	62.8 ± 0.7	17

* Δ° represents the difference of water contact angle between the angles measured orthogonal and parallel to the line pattern.

4. Neuron cells behavior on LIP treated substrates

Prior to the cell culture experiment, all substrates were sterilized with 70 % isopropyl alcohol for 10 min and washed three times with distilled (DI) water. Following drying step, these substrates were stored in 24 cell culture well for following cell culture experiment. Dorsal root ganglia (DRG) were isolated from newborn Sprague Dawley rats between postnatal day 1 and 5 (P1-P5) and prepared following all regulations of local animal welfare. One DRG per each substrate was seeded and incubated at 37°C at an atmosphere of 4 % CO_2 (CO_2-Incubator MCO-17AIC, Sanyo) in 30 µL of the culture medium for 4h to support attachment. It was avoided to use any additional specific coatings (laminin, fibronectin and etc.) in order to observe the direct effect of the surface topography upon the cellular adhesion. After attachment, the well was filled with additional 500 µl culture medium. The space between the wells was filled with 10 mL DI water to maintain humidity and thermal conductivity. Non-treated Al/Al_2O_3 nanowires were used as control since glass cover slips showed no attachment of DRGs.

Immunohistochemical staining for microscopic analsys

After six days, culture medium was removed and washed with phosphate buffered saline (PBS) then DRGs on the substrates were fixed with 4 % formaldehyde (FA solution dissolved in PBS) for 12 min and washed three times with PBS. Afterwards they were incubated with 4',6-diamidino-2-phenylindole (DAPI) and Anti-Tubulin beta III (Millipore MAB1637) combined with goat-anti-mouse 488 (Invitrogen, A11029) to stain for cell nuclei and for axons, respectively. Glial cells were identified by S100 staining. The samples were evaluated using a fluorescence microscope (Observer Z1, Carl Zeiss). In order to analyze the angle of cell nuclei an image processing software "ImageJ" (US National Institute of Health) was used.

5. Results and discussions

In contrast to current literature, substrates were not pre-coated with any organic substances which may affect cell behavior such as adhesion or proliferation [18, 20]. Interestingly, DRGs exhibited an increased attachment on patterned and even on non-treated nanowires while no attachment of DRGs was observed on glass substrates. This is a clear evidence for a specific topography effect upon the cells. It has been shown that inorganic surfaces may imitate nanoscale biological topographies [115, 116]. In this regard, it is assumed that the Al/Al_2O_3 nanowires represent a new material combination for cultivation of DRGs without need of any chemical treatment, which mostly affects the cell behavior. It is known that the outgrowing axons are influenced by the migrating schwann cells and glial cells [117, 118] as well as by specific molecules such as Laminin [119] or Neuronal Growth Factor (NGF) [120] and/or even their topography on engineered surfaces [121]. Therefore similar disposal of cell nuclei and fibers of DRGs on different patterned Al/Al_2O_3 nanowires is an indication of the direct effect of the topography on the cellular behavior. As it can be seen in Figure 5-1, there are axonal alignments of DRG on all LIP treated substrates while DRG shows radial distribution on as deposited Al/Al_2O_3 nanowires in Figure 5-2. It reveals that such patterns seem to have an enhanced affect to axons to be elongated along the parallel direction of the patterns.

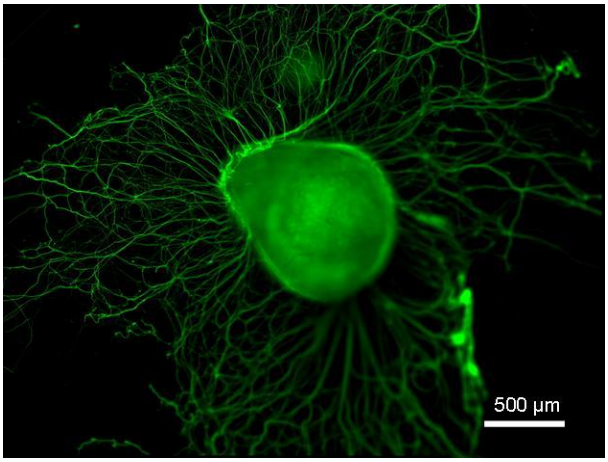

Figure 5-1. Anti-Tubulin beta III stained DRG cell on as deposited Al/Al_2O_3 nanowires.

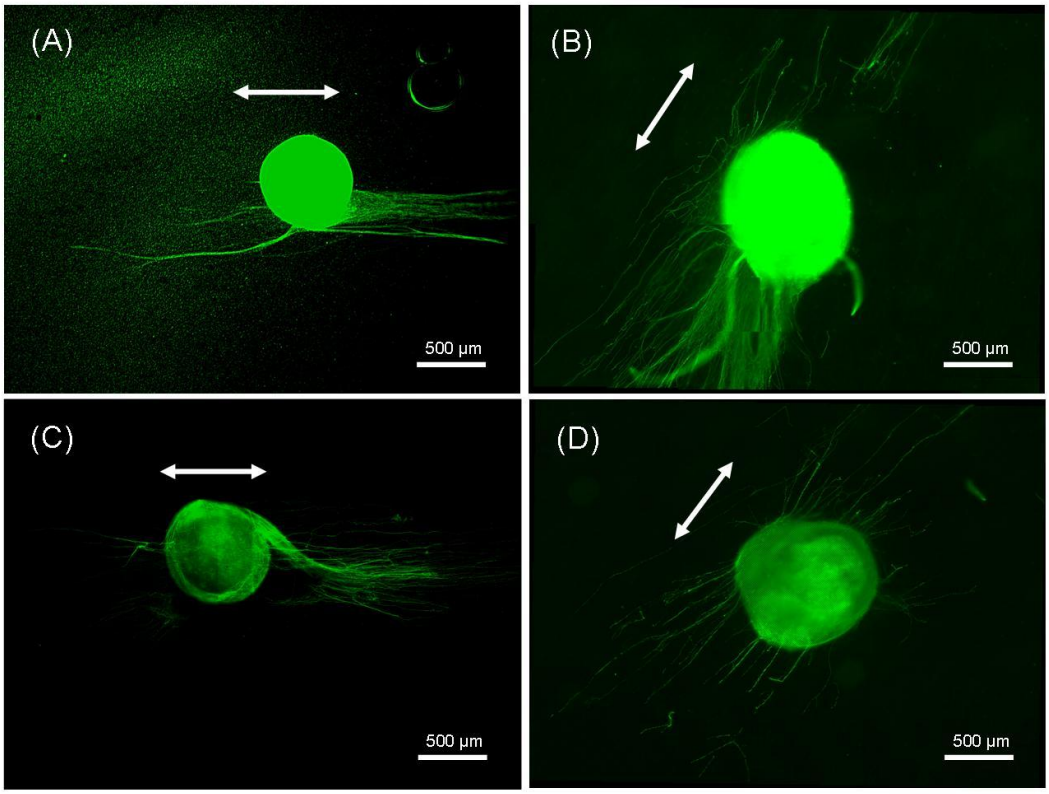

Figure 5-2. Anti-Tubulin beta III stained DRGs on LIP treated surfaces with period of (A) 1 µm, (B) 2 µm, (C) 4 µm and (D) 8 µm. Arrow indicates the parallel direction of the patterns.

However this does not give a direct answer how the axonal guiding progress is working, but it may reasonable to suppose that the cellular mechanisms underlying axonal guidance are comparable to those responsible for guidance of immigrated cells from DRGs. It is known that glial cells are the most abundant cell types in the central nervous system [122]. They provide support and protection for neurons. They are thus known as the supporting cells of the nervous system. The main functions of glial cells are: to surround neurons, hold them in place and to supply nutrients and oxygen to neurons. In this context, glial cells were investigated in order to quantify the enhancement of the neurite guidance of DRGs since they could indicate the contact guidance of neural axons. As an example Figure 5-3 shows DAPI stained immigrated glial cells from DRG on the substrates. It can be seen clearly that cells were randomly distributed on non LIP treated surface (Figure 5-3(a)) while they were aligned along the parallel direction to the linear patterns (Figure 5-3 (b)). The angle of cell direction on the substrate was measured as shown in Figure 5-4. It shows the represent angle of cell nuclei on the surfaces. 90 degree represent that cells are

totally parallel to the linear patterns while 0 degree represent that cells are totally perpendicular to the linear patterns.

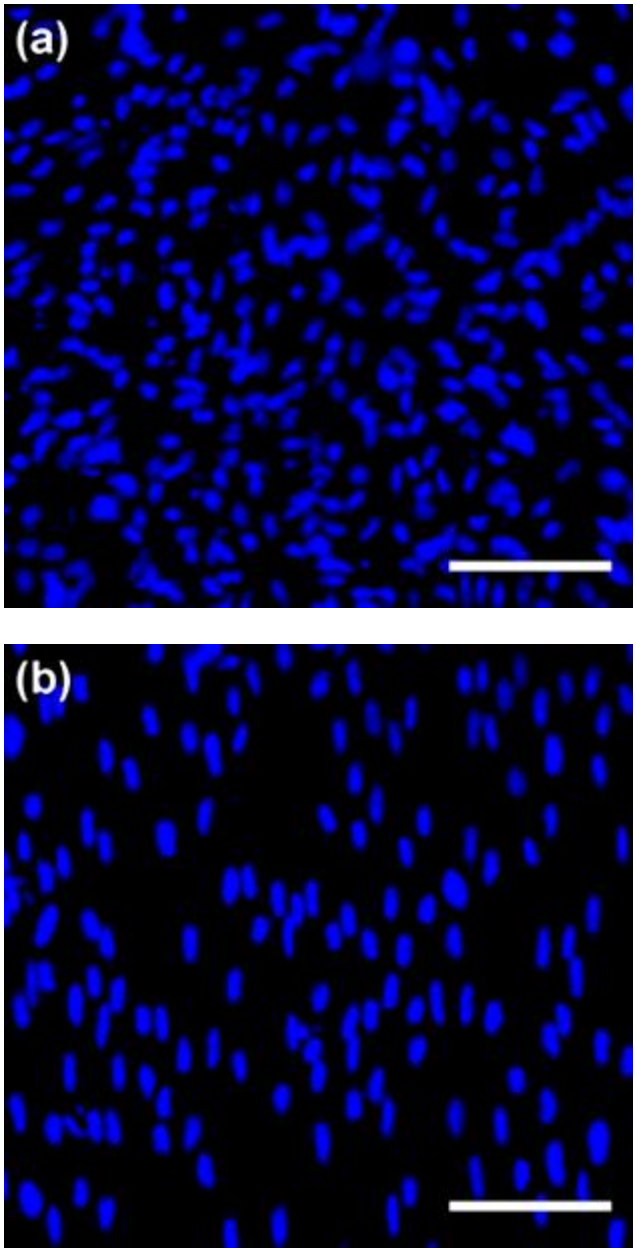

Figure 5-3. Fluorescence image of DAPI stained immigrated cells from a DRG (a) on as-deposited and (b) patterned Al/Al_2O_3 nanowires at period of 2 μm (scale bar: 100 μm).

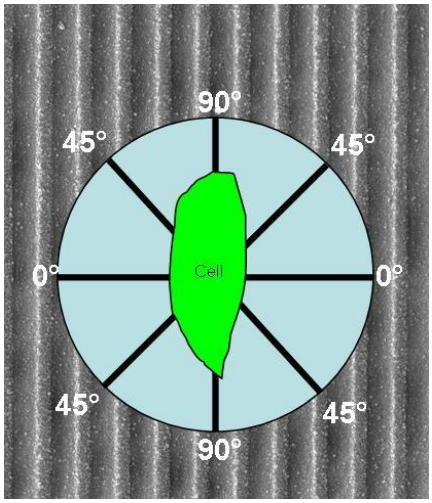

Figure 5-4. Illustration of the cell angle measurement.

The data presented in Figure 5-5 confirm the visual observation of the angle in a range of 85-95° (90° means a perfect alignment to the parallel direction of the patterns) of outgrown cell nuclei attached and elongated on the as-deposited and patterned Al/Al_2O_3 nanowires. The percentage value was obtained in comparison to total cell numbers on each substrate. Especially 2 µm periodic patterns showed highest cell alignment rate in a range of 85-95° with 36.72% ± 1.1 in comparison to other substrates; non treated Al/Al_2O_3 nanowires (8.21% ± 0.04), period pattern of 4 µm (32.92% ± 1,81), period pattern of 8 µm (27.45% ± 0.8), and period pattern of 1 µm (22.63% ± 0.13), respectively.

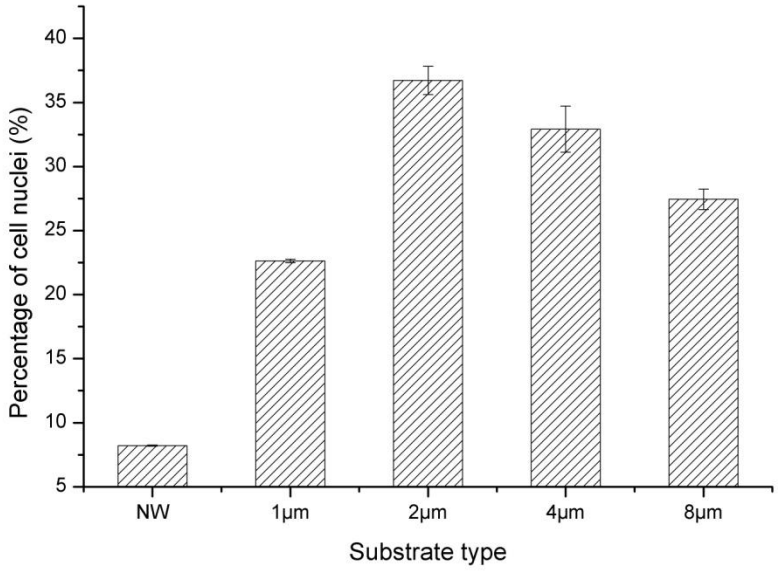

Figure 5-5. Percentage of aligned cell nuclei in a range of 85-95° on as deposited and LIP treated nanowires.

Figure 5-6 shows that axons follow the glial cells and arrange parallel to the linear patterns created by LIP. Arrows in Figure 5-6 (B) and (D) shows the parallel direction of patterns. More detailed observation is shown in Figure 5-7. Fluorescence pictures as well as the results of cell nuclei alignment reveal clearly that neuronal axons are closely orientated to aligned glial cells.

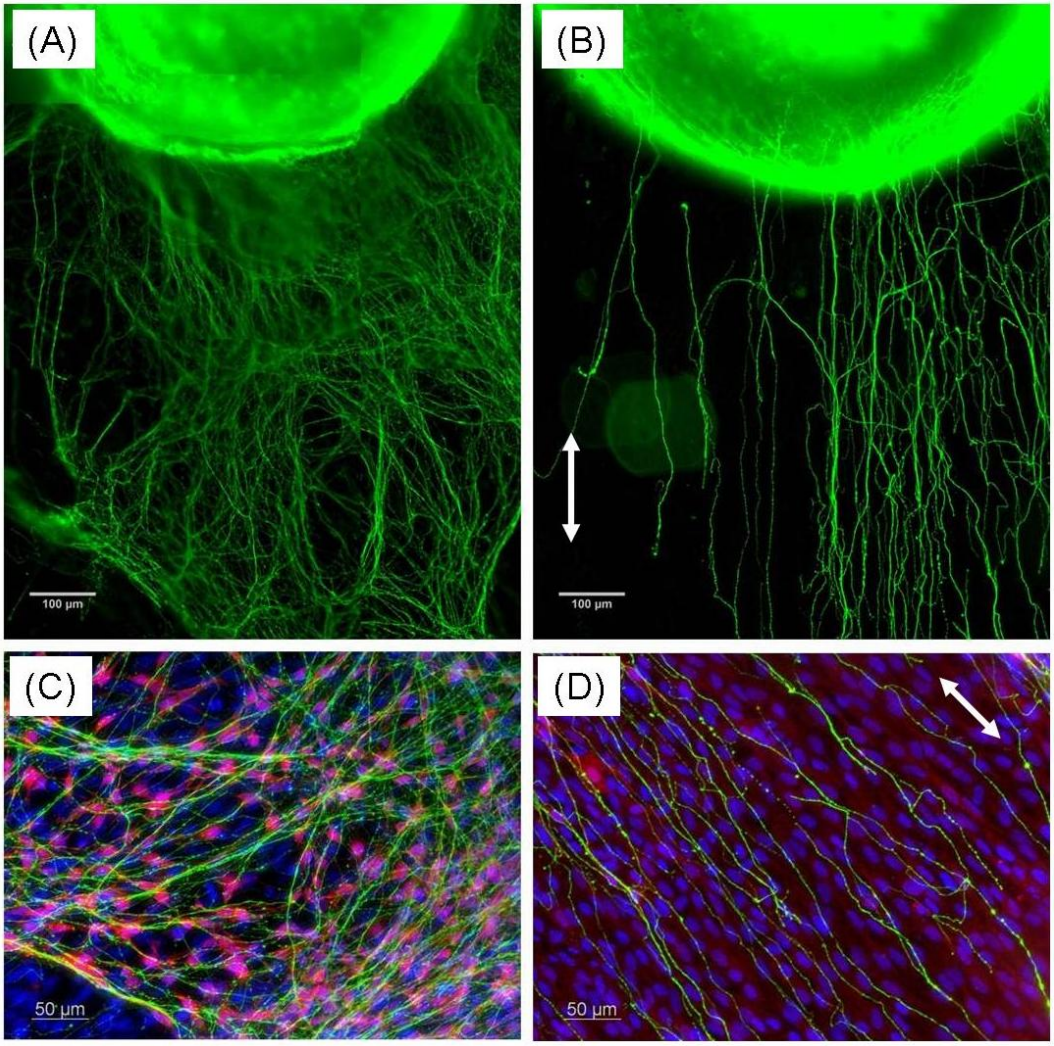

Figure 5-6. (A) and (C) Random growth of neurites on as-deposited nanowires. (B) and (D) Aligned growth of neurites on patterned nanowires. Glial cells (stained with S100 (red) protein) similarly exhibit (C) random growth on non-treated nanowires and (D) aligned growth on laser patterned nanowires. (Blue: DAPI stained cell nuclei, Green: Anti-Tubulin beta III stained axons and Red: S100 staining).

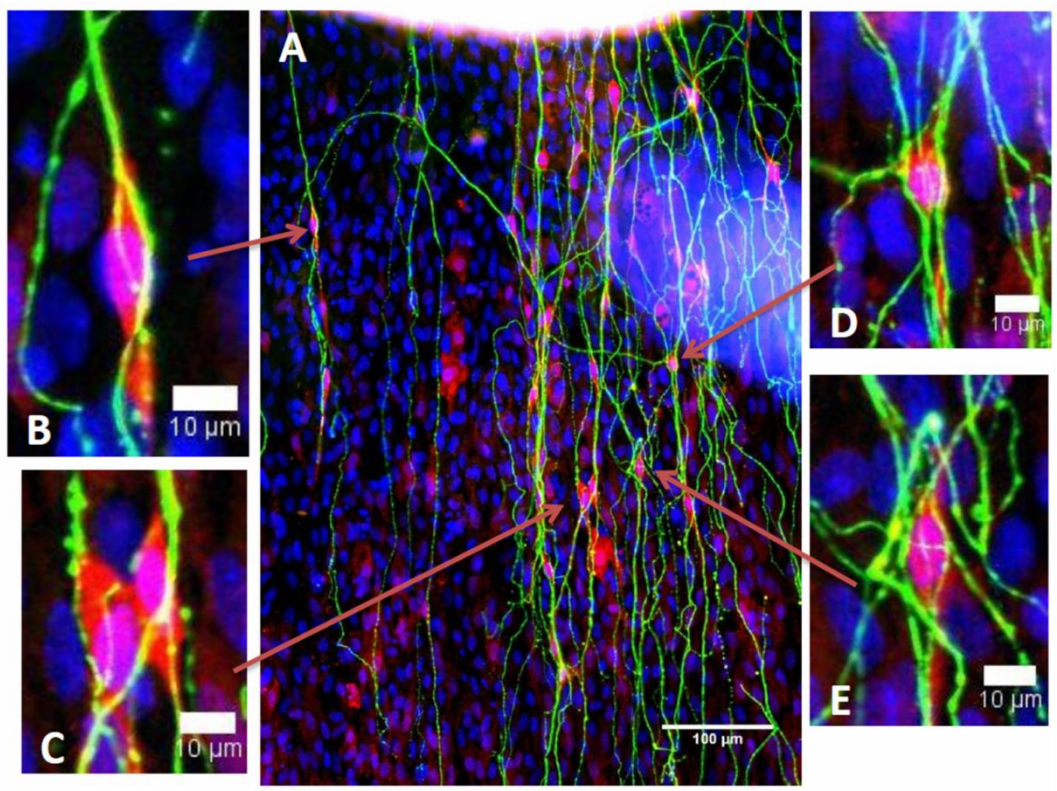

Figure 5-7. Fluorescence images of immigrated cells of DRG on 2µm patterned substrate with DAPI (blue) for cell nuclei, anti-S100 (red) for glial cells and anti-tubulin beta III (green) for axons; (A) overview (B-E) magnified regions marked with arrow in overview.

LIP demonstrates a novel patterning approach of biphasic Al/Al_2O_3 nanowires. The periodic energy distribution provides a selective melting and re-solidification of biphasic Al/Al_2O_3 nanowires and oxidation of Al core to Al_2O_3 due to a crack formation of Al_2O_3 shell [93]. This ensures that in every case an identical outer surface contacts with cells. This study on DRGs thus shows the direct effect of the topography on the enhanced cellular adhesion and directional neurite outgrowth.

Of course anisotropic wetting behavior may play a role on the cell response since more hydrophilic behavior is observed in parallel direction to the periodic patterns. Similarly Leclair et al. showed neural cell alignment at the surface with anisotropic wettability. They showed that the glass windows promoted cell adhesion, whereas the surrounding fluoropolymer displays a cell-repelling character [123]. However, a question still remains whether cell react due to physical and/or chemical properties.

Obviously, the size of periodic patterns plays a major role for the alignment. The 2 µm periodic patterns allow the optimal alignment of cells. Furthermore enhanced attachment of DRGs on all substrates was observed in contrary to non-adhering behavior observed on standard glasses. Further investigations will be necessary to explore the reasons for this specific behavior. Especially the analysis of focal adhesion points might lead to more detailed information. Maybe the most interesting finding is the fact, that the sole topography of the Al/Al_2O_3 nanowires leads to an increased attachment of the DRGs, which is usually achieved when specific gels are used. This property allows the investigation of the direct influence of signaling or trophic molecules upon the dorsal root neurons (by eliminating any side-effects which may be induced by the extra cellular matrix (ECM) gels such as matrigel [124]. Most probably, this surface modification approach can also be interesting for studying other primary neuronal systems to be applied in various medical applications.

6. HOB and NHDF cells behavior on DLW treated substrates

Prior to the cell culture experiment, all substrates were sterilized with 70% ethanol for 20 minutes and washed three times with phosphate buffered saline (PBS). Human osteoblasts (HOB, Promocell, Heidelberg, Germany) were incubated and cultured in Dubelcco´s modified eagle medium (DMEM, PAA, Pasching, Austria), supplemented with 15 % fetal calf serum (FCS, PAA) and 1 % penicillin/streptomycin (P/S) in a standard incubator (37 °C, 5% CO_2 , 95 % humidity). Similarly, normal human dermal fibroblast (NHDF, Promocell, Heidelberg, Germany) were cultured with Q333 (PAA, Pasching, Austria) as a complete medium for fibroblasts. It is supplemented with selected serum components and growth factors. HOB were seeded at a density of 100 cells/mm^2 and NHDF at a density of 63 cells/mm^2 on the substrates, respectively. The incubation time was 2 days for both cell types.

6.1 Immunohistochemical staining for microscopic analsys

After two culture days, the cells were washed with PBS one time after removing the medium at 37°C. Afterwards HOB and NHDF were incubated at 37°C for 30 min with CellTracker^{TM} Green 5-chloromethylfluorescencein diacetate (CMFDA, Invitrogen) for the cell body. Subsequently they were rinsed 2 times with PBS and fresh culture medium was added for the second incubation at 37°C for 30 min. The fixation was done by incubation in ice cold methanol (-20°C) for at least 10 min. Cell nuclei of HOB and NHDF were counterstained by 4',6-diamidino-2-phenylindole (DAPI, Vectashield, Vector Laboratories). The substrates were dried with air and fixed on standard microscopic slides for the microscopic analysis. An Axioskop microscope (Carl Zeiss, Jena, Germany) was used for the microscopic analysis.

6.2 Fixation for SEM analysis

Cultured cells (HOB and NHDF) on the samples were fixed with 2 % glutardialdehyde in 0.15 M cacodylate buffer at RT (room temperature) for 1 h (2 times 30 min). After

fixation the samples were incubated in osmium tetroxide (1 % in 0.2 cacodylate buffer) for 1h in the dark at RT to increase the contrast. Afterwards, the substrates were washed 3 times with DI water and then dehydrated using ethanol (2 times for 5 min at 30 %, 50 %, 70 %, 80 %, 90 % and 2 times for 10 min at 100 %) under movement at 4°C. The samples were dried by Critical-Point-Drying (Polaron CPD 7501, Quorom Technologies) after dehydratation procedure and they were sputtered with gold-palladium (Polaron, Sputte rCoater). The SEM analysis was carried out using a FEI XL 30 ESEM FEG SEM device (Hilsboro).

7. Results and discussions

Figure 7-1 shows fluorescence images of human osteoblast cells (HOB) and normal human dermal fibroblasts (NHDF) cells on as deposited Al/Al_2O_3 nanowires. As it can be seen, NHDF cells were barely observed on Al/Al_2O_3 nanowires while HOB cells covered well the surface. HOB exhibited a normal well-spread morphology whereas NHDF were very small with an untypical cell-nucleus ration. The overall number of NHDF was clearly reduced. It shows obviously converse behavior of both cell types on identical surface.

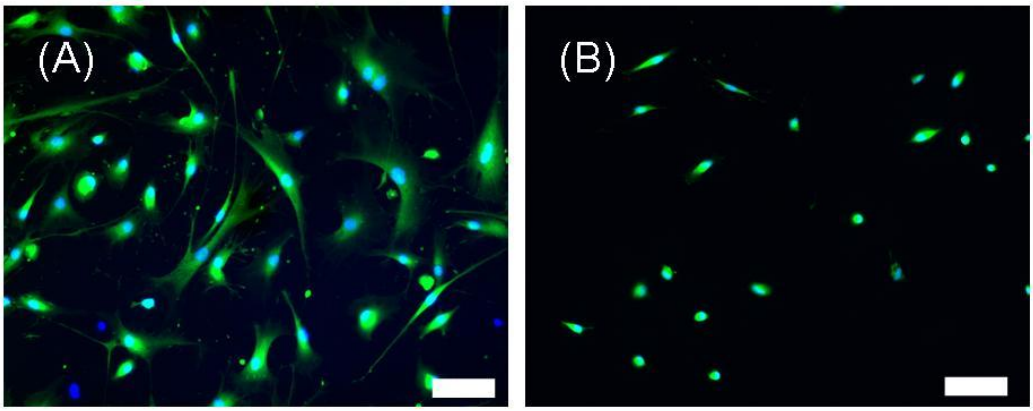

Figure 7-1. Fluorescence images of (A) HOB and (B) NHDF on Al/Al_2O_3 nanowires, respectively. The cell body was stained with CMFDA in green and the nuclei were counterstained with DAPI. Scale bar is 100 µm.

For more detailed investigation, SEM images were taken. It gives more information how those cells behave on prepared substrates. Indeed both cells were preferred to outgrow on flat stainless steel (STS316L) surface (Figure 7-2 (A) and (C)). They were well spread and flattened, indicative of good adhesion but on Al/Al_2O_3 nanowires they show clearly selective outgrowth. Especially NHDF exhibit a smaller number of cells with a smaller cell size, indicative of poor adhesion although HOB is not flattened as before.

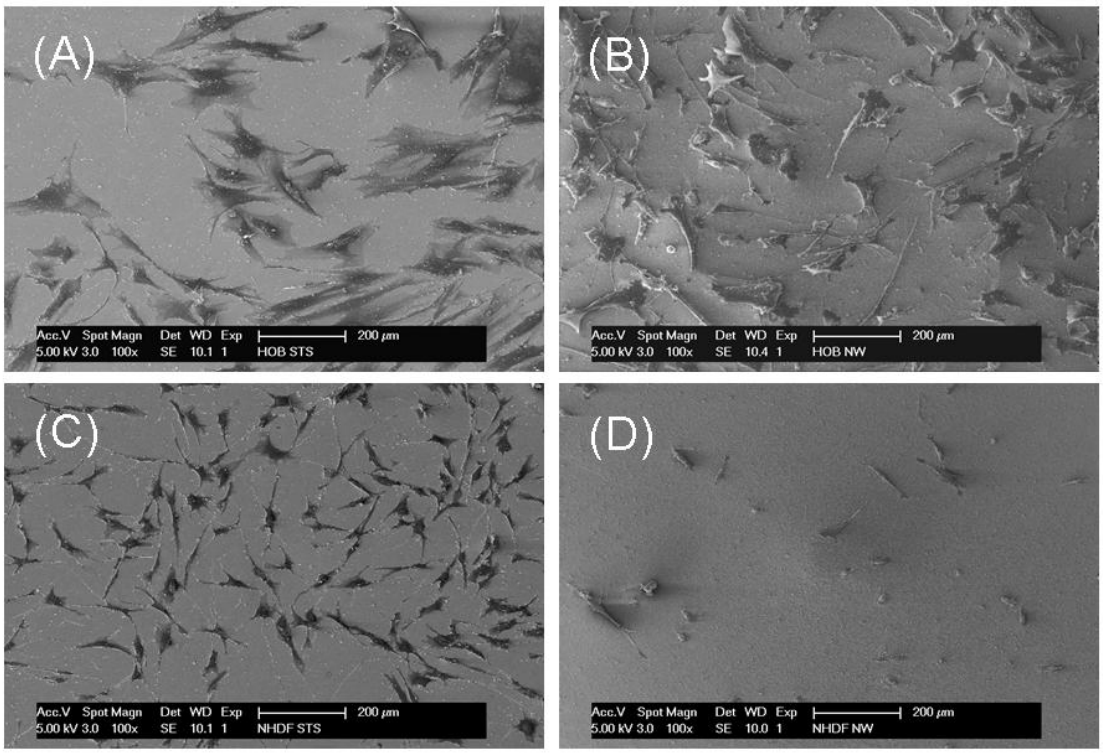

Figure 7-2. HOB (A and B) and NHDF (C and D) cultured on stainless steel (STS316L) and Al/Al_2O_3 nanowires, respectively.

In magnified SEM images (Figure 7-3), cell morphology can be distinguished clearly. While both cells on smooth STS316L surfaces show well spread and flattened with dense and longer filopodia, indication of cell-cell interaction as well as cell-surface interaction, HOB and NHDF were shown much shorter length of the filopodia extension on Al/Al_2O_3 nanowires. Although the filofodia extension of both cell types was reduced on Al/Al_2O_3 nanowires, HOB can adhere on Al/Al_2O_3 nanowires as similar as on STS316L. Such flattened cell morphologies of both cell types were previously reported by use of smooth surfaces compare to alumina. Malik et al. showed a morphology change of osteoblasts on well polished alumina and polystyrene surfaces which are biocompatible materials [125]. The osteoblasts cultured on both surfaces showed completely spread and flattened morphology independent of material types. In a similar way, Marchi et al. cultured fibroblast on as sintered and polished alumina which had different roughness [126]. The fibroblasts were well attached and spread on polished surfaces as similar to Figure 7-3 (C). However highest adhesion of fibroblasts was observed on well polished alumina surface while lowest adhesion was shown on as sintered alumina surfaces. It may demonstrate that common cell morphology is governed by material surface. NHDF is favor of smooth surface compared to HOB. In other word NHDF is more sensitive to rougher

surfaces in terms of cell surface interaction as they showed significant morphology change and smaller number of cells.

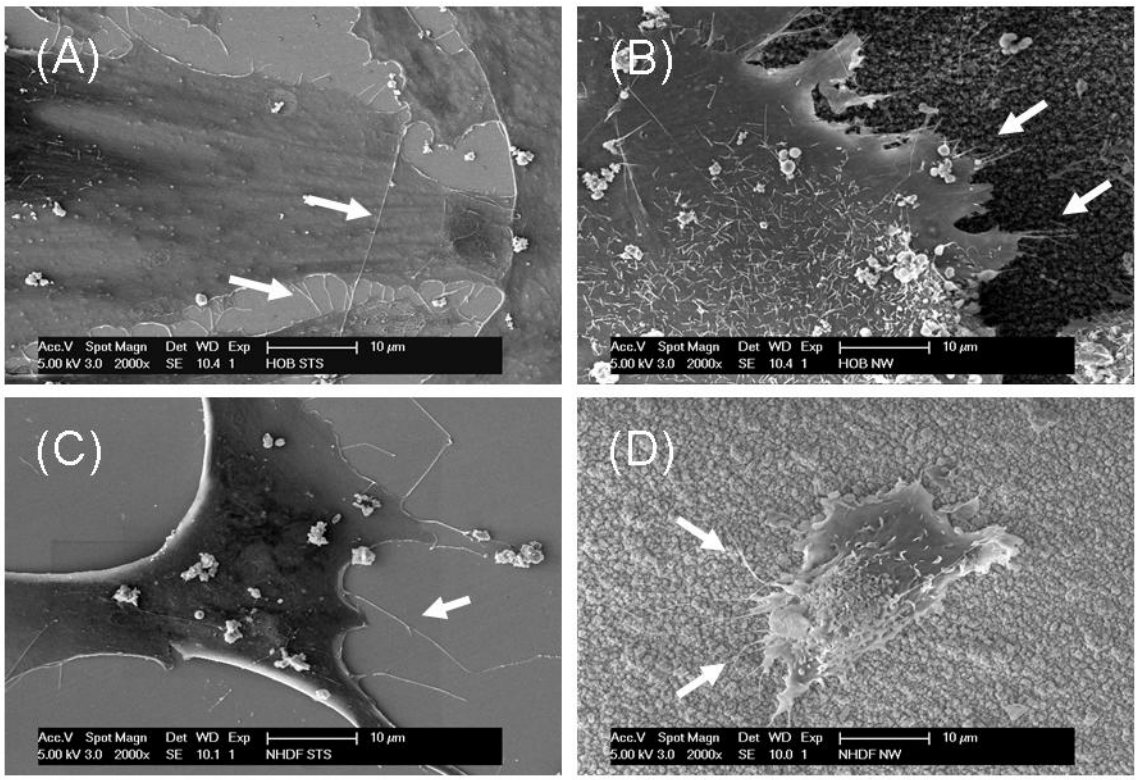

Figure 7-3. Morphology of HOB (A and B) and NHDF (C and D) cultured on stainless steel (STS316L) and Al/Al_2O_3 nanowires, respectively. Arrows indicate filopodia.

Consequently those cells were cultured on DLW patterned substrates at period of 50 µm, 100 µm and 200 µm. Figure 7-4 shows the fluorescence images of HOB and NHDF recorded at the culture periods of 2 days. It can be seen that NHDF shows morphology of linear elongation on all substrates. HOB shows similar elongation only on the substrates with 50 µm periodic channels and more cells were observed than NHDF. As compared to the insets which represent the direction of the channels, elongated NHDF showed its lateral distance similar with the distance of the channels.

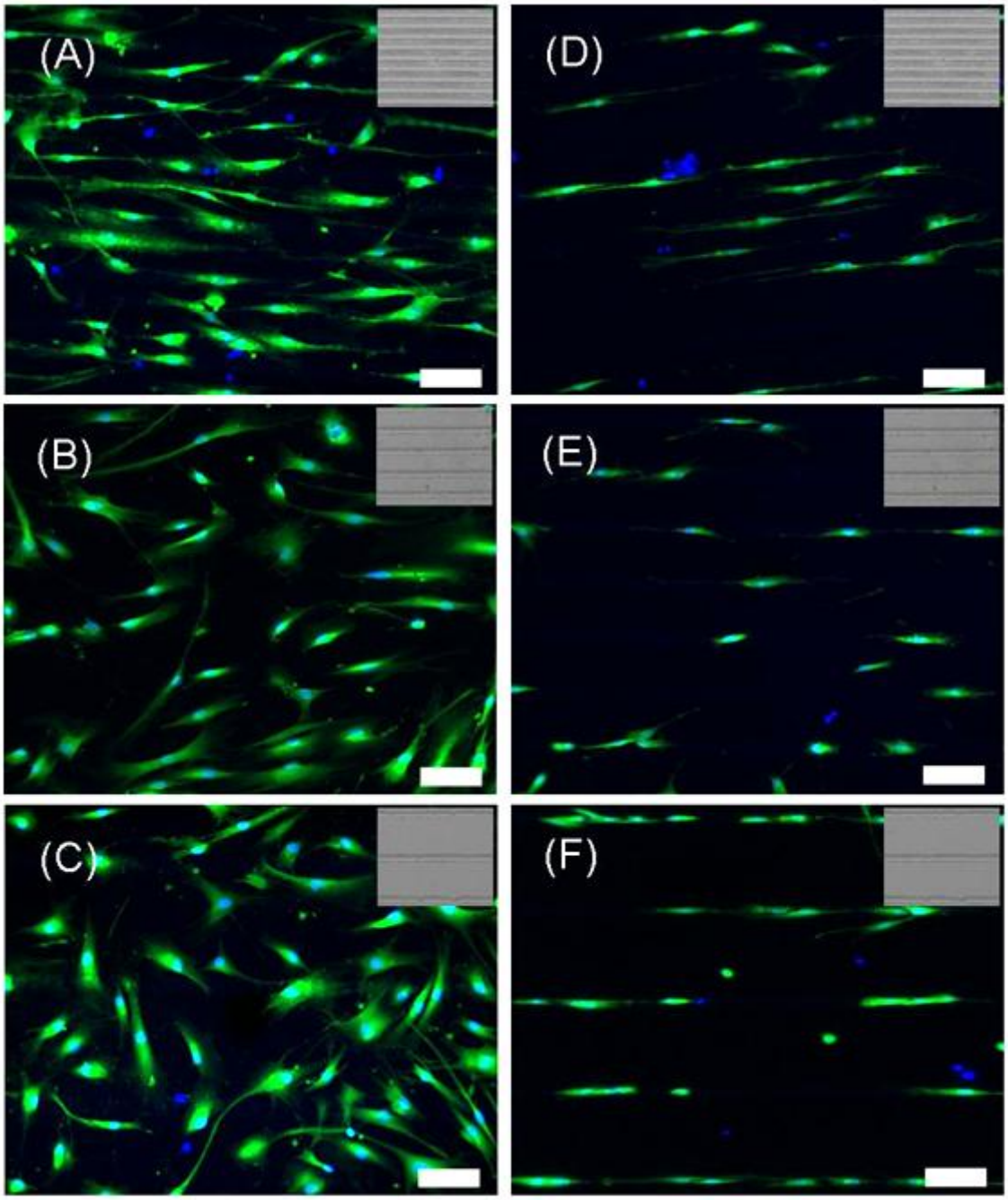

Figure 7-4. Fluorescence images (same staining as in figure1) of HOB (A, B and C) and NHDF (D, E and F) on DLW patterned substrates at period of 50 µm, 100 µm and 200 µm, respectively. Inset of each image represents the patterned substrate. Green and blue indicate stained cell body and cell nuclei, respectively. Scale bar is 100 µm.

The SEM images were used for cell morphology analysis as summarized in Figure 7-5 for NHDF and in Figure 7-6 for HOB cultured on patterned substrates. In the case of NHDF, the cell elongation increased as indicated by arrows in Figure 7-5 (A), (B) and (C). In addition filopodia extended mostly within the channels and edge without going to the Al/Al_2O_3 nanowires, as indicated by arrows in the Figure 7-5 (D), (E) and (F). Moreover NHDF was well spread and flattened on the channels similar to them on smooth surfaces, as seen on the STS316L. The cell protrusions extended in parallel direction to the channels remained longer than those in orthogonal direction to the channels. It seems that cells use filopodia for spatial sensing in their movement around the environment as it was frequently observed that the filopodia extended along the channels. Filopodia is a cellular tool to explore the environment. NHDF and HOB are migrating cells. Before they migrate, they explore the environment with the filopodia. If the environment is good, the cell migrates. Otherwise the filopodia are retracted [127]. Thus NHDF elongated and aligned along the channels not spread on the Al/Al_2O_3 nanowires as indicated by the red arrow in Figure 7-5 (F) since NHDF showed bad adhesion the Al/Al_2O_3 nanowires as shown in Figure 7-2 (D).

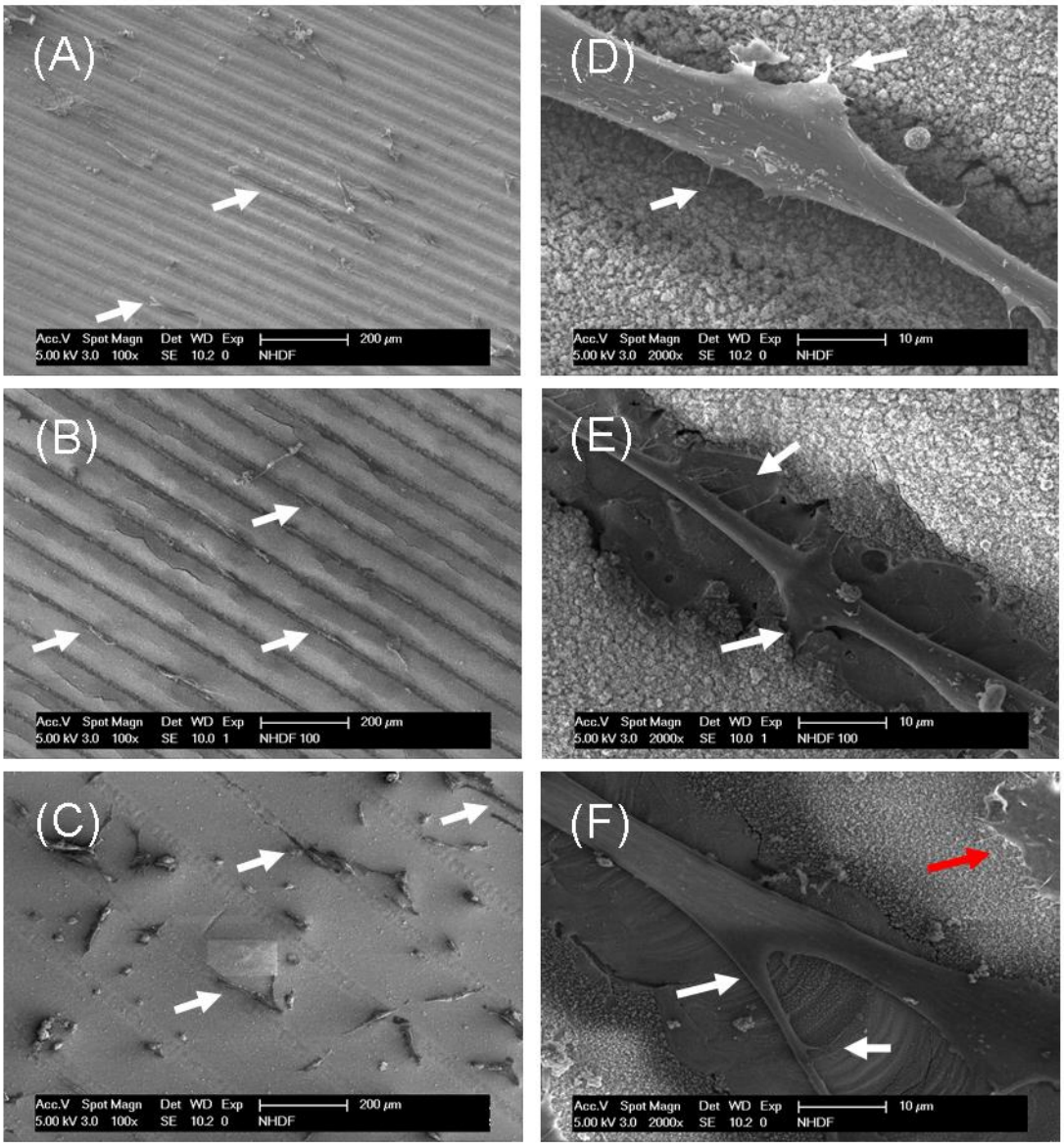

Figure 7-5. SEM images of NHDF cultured on DLW patterned substrates at period of 50 µm (A and D), 100 µm (B and E) and 200 µm (C and F). Arrows in A, B and C indicate aligned cells on the channels. White arrows show filopodia extension in D, E and F and red arrow in F indicates a cell on non treated Al/Al_2O_3 nanowires.

Contrast to NHDF, HOB shows better adhesion property on both as-deposited (Figure 7-2 (B)) and patterned Al/Al_2O_3 nanowires (Figure 7-6 (A), (B) and (C)) than NHDF. The higher degree of cell alignment was shown on patterned substrates at period of 50 µm (Figure 7-6 (A)). Indeed HOB was frequently observed to cross over to the surface in Figure 7-6 (B) and (C). On the other hand, the cells on Al/Al_2O_3 nanowires show elongated morphology (red arrows in Figure 7-6 (A), (B) and (C)) when they were near to the neighboring cells which were adhered on the channels (white arrows in Figure 7-6 (A), (B) and (C)), and then aligned also in the parallel

direction. It can be seen clearly in Figure 7-6 (A) and it may explain why cells show better elongation and alignment on narrow patterned substrate rather than larger periodic patterned substrate. The cells on the channels mostly show cylindrical morphology with less filopodia. However some filopodia extended to the edge rather than the surface of the channel, as indicated by arrows in the Figures 7-6 (E). In this case cells were shown flattend as similar as NHDF. It indicates clearly filopodia extension is the most predominant key to define cell morphologies.

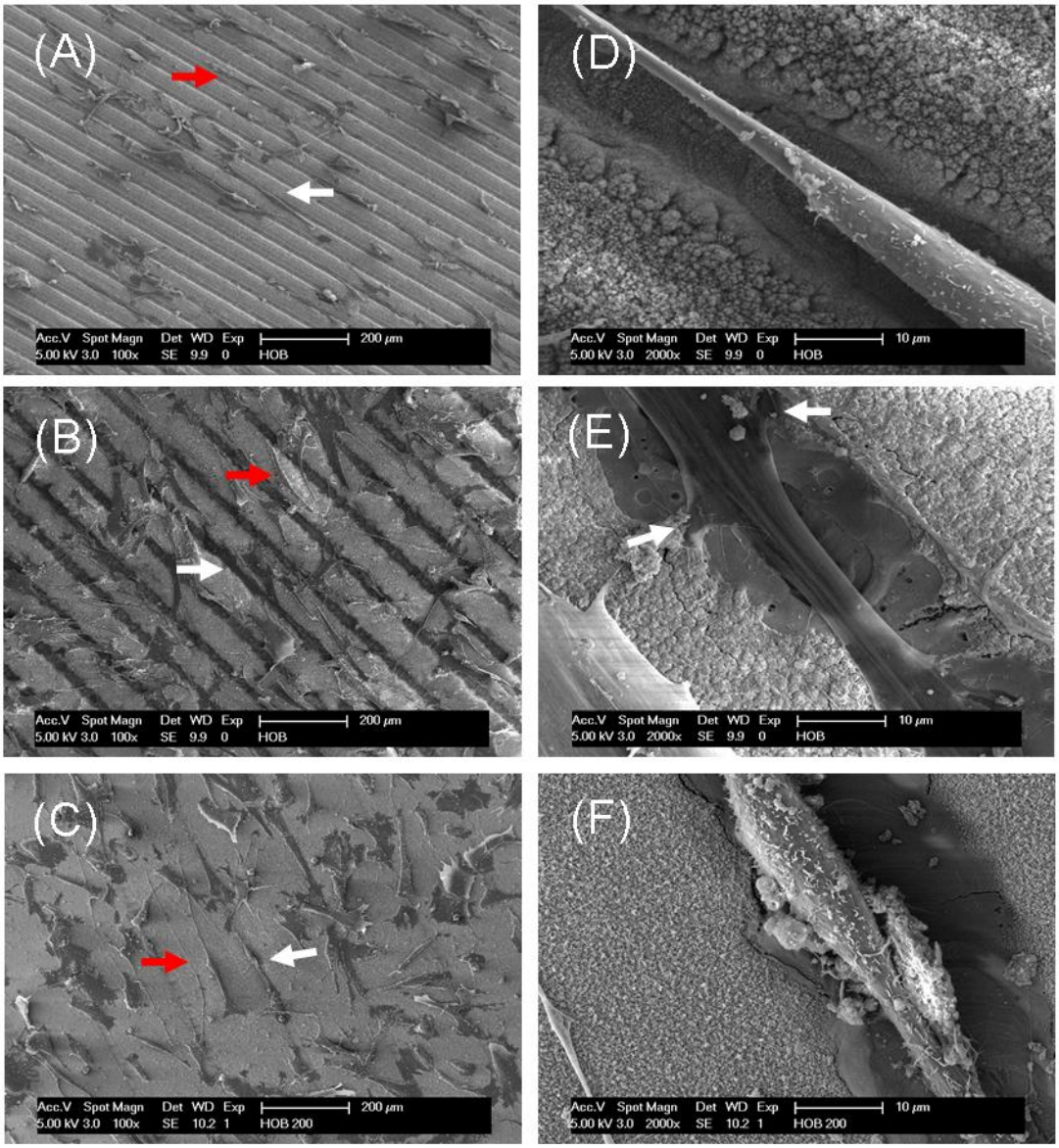

Figure 7-6. SEM images of HOB cultured on DLW patterned substrates at period of 50 µm (A and D), 100 µm (B and E) and 200 µm (C and F). White arrows indicate cell on the channel and red arrows show cell on non treated Al/Al_2O_3 nanowires in A, B and C. Arrows in E show filopodia extension to the edge of the channel.

In conclusion, HOB and NHDF showed converse reaction on Al/Al_2O_3 nanowires although physical and chemical properties were identical. Both cell types showed flattened morphology on smooth surfaces. NHDF were more sensitive, whereas HOB were still able to adhere on Al/Al_2O_3 nanowires. For the investigation of cell guidance, as summarized in Figure 7-7, NHDF exhibited an enhanced elongation and a higher degree of alignment on all patterned substrates although the cell number was significantly decreased. The improvement of the NHDF adhesion and alignment were most prominent on laser induced channels since they do not adhere well on Al/Al_2O_3 nanowires.

HOB showed better cell elongation on the substrates with 50 µm periodic channels. On the other hand, HOB were not performing same elongation and alignment behavior on both 100 µm and 200 µm period as shown in Figure 7-7 (B) and (C). This phenomenon could be explained by highlighting the difference of size between cells and structures. It is known that the size of HOB ranges between 10 to 30 µm in diameter [128]. The distances between the produced channels were in the range of 50 µm, 100µm and 200µm. The width of the laser created channel was around 20 µm in all substrates. In the case of 50 µm periodicity, cells have higher tendency to contact with the channels compared to other substrates. Therefore more cell alignment could be observed.

In contrast, HOB are exposed more to Al/Al_2O_3 nanowires than to the channels in the case of 100 and 200 µm periodicity. Therefore cell alignment is less observed since good adhesion and proliferation of HOB on Al/Al_2O_3 nanowires was shown before. It could be concluded that the HOB cell alignment is reversibly proportional to the periodic channel distance. It decreases while the distance of the channels on the substrate increases.

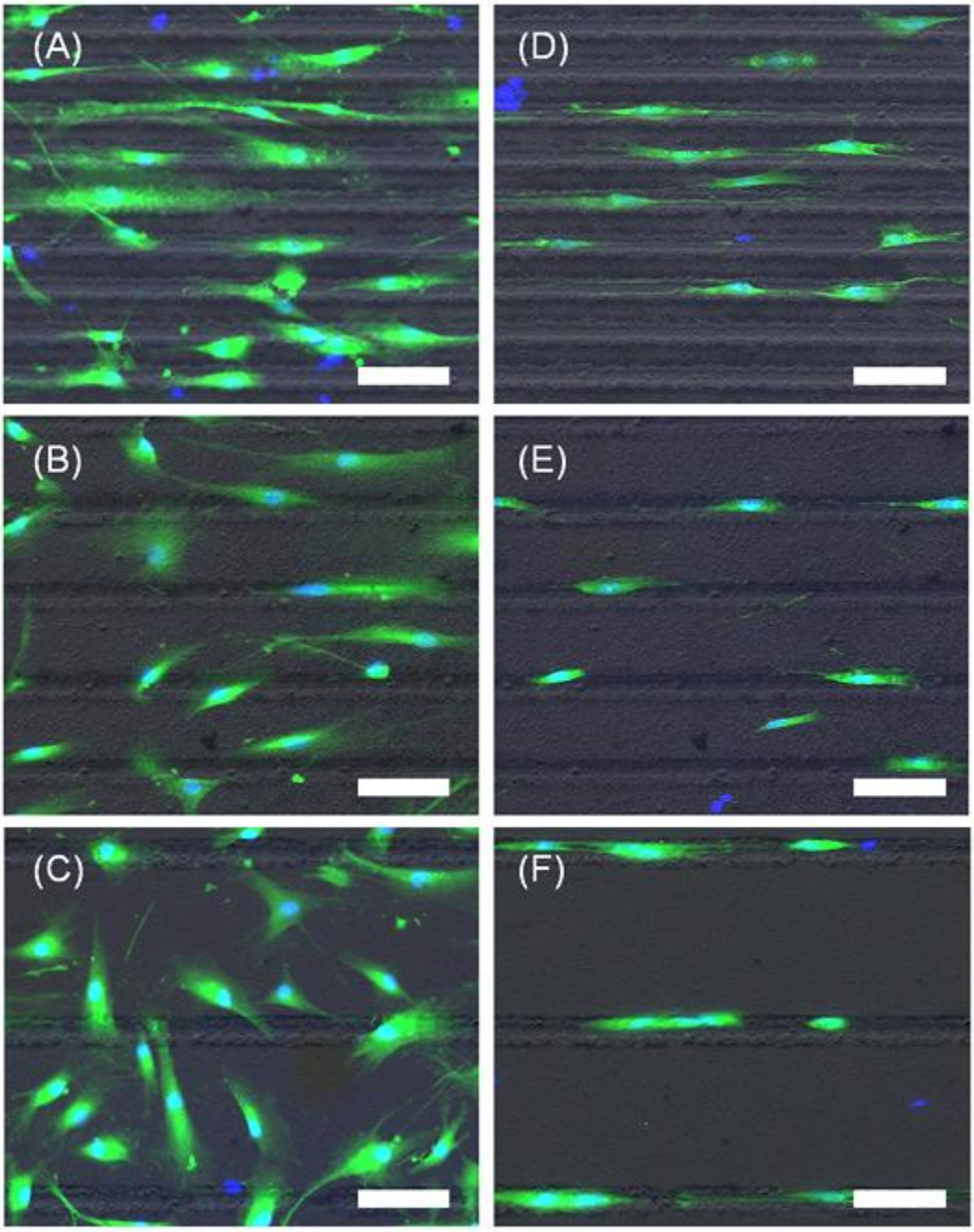

Figure 7-7. Fluorescence images overlapped on SEM figures of HOB (A, B and C) and NHDF (D, E and F) on DLW patterned substrates at period of 50 µm, 100 µm and 200 µm, respectively. Scale bars represent 100 µm.

8. Future aspect

As a preliminary study, single neuron cells (PC12) were cultured on DLW patterned substrates. PC12 cells were incubated in RPMI-Medium (Sigma-Aldrich) with 10% (Fetal Calf Serum) FCS and 100ng/mL (Neuronal Growth Factor) NGF for 14 days, medium was changed every day. 20,000 cells per substrate were seeded. For scanning electron microscopy analysis, the samples were fixed with 4 % formaldehyde (FA) + 1 % Glutaraldehyd in phosphate buffered saline (PBS) for two hours, washed three times with PBS and dehydrated with an increasing alcohol concentration (50 %, 70 %, 80 %, 90 %, 2x 100 %). The cell culture wells were flooded with Hexamethyldisilazane (HMDS, Sigma-Aldrich, 379212) for 5 min and kept under the exhaust hood for out-gasing and dried in one day. The samples were then coated with gold-palladium (Polaron, Sputter Coater) for following SEM analysis.

The PC12 neuron cells were adhered only on the channels and axons were connected to other neuron cells (cell-cell interaction) as shown in Figure 8-1. PC12 cells were approximately rounded while human osteoblast cells (HOB) and normal human dermal fibroblasts (NHDF) were either elongated or aligned on the channels. It gives another idea concerning topography effect of the surfaces in terms of geometry. It means that cell alignment might be affected geographically due to the depth of the channel regardless of surface roughness.

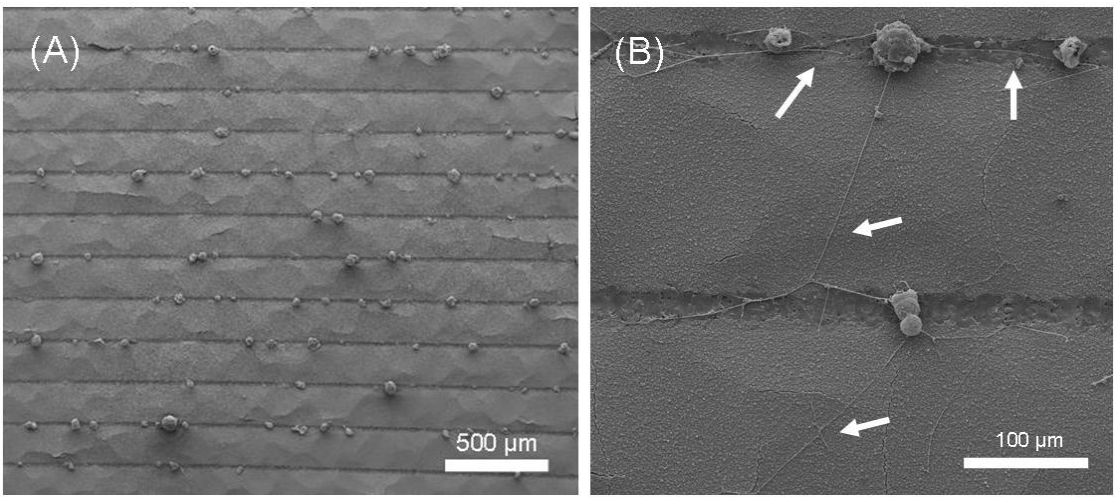

Figure 8-1. Single neuronal cells on DLW treated substrate. (A) Overview and (B) magnified region of interest. Arrows indicate axonal extension.

In contrast, when HOB and NHDF were cultured on LIP treated substrates (Figure 8-2), any alignment of cells was observed following the patterns in comparison to previous results of DRGs where a strong alignment of neural fibers and glial cells was observed on LIP treated Al/Al_2O_3 nanowires (see Figure 5-7). There was a direct elongation of cells which were perfectly aligned along the linear patterns induced by LIP treatment of Al/Al_2O_3 nanowires. It reveals clearly that as cellular responses to physical cues may vary based on the cell type. Since these experiments show early stage of cell surface interaction, a longer cell culture period and co-culture systems with various cells will be desired for further investigations.

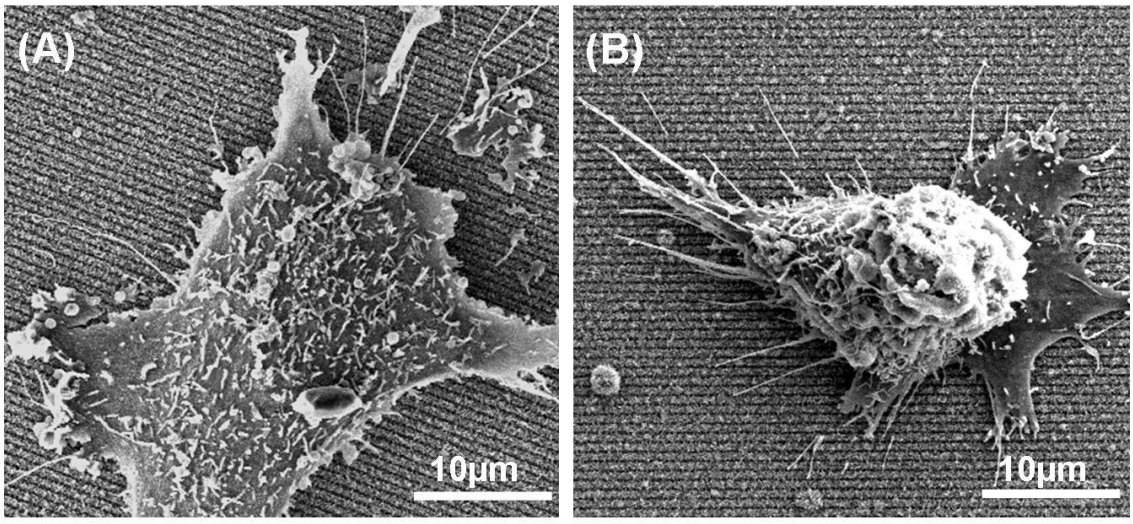

Figure 8-2. HOB and NHDF on LIP treated substrate. (A) HOB and (B) NHDF.

9. Conclusions

In Part 1, chemical vapor deposition (CVD) of the single source precursor $[^tBuOAlH_2]_2$ were performed in parabolic flights which induce gravity (G) variation from 0.04 to 1.8 G. Two temperature ranges (at 400°C and at 600°C) were applied during the parabolic flights while other deposition parameters were kept constant. In general, only spherical nanoparticles were observed at 400°C and the formation of core/shell nanowires was observed at 600°C on the substrate surface. It reveals that there is no gravity impact on the chemical reaction compare to previous experiments on earth condition. On the other hand, the growth of both spherical particles and nanowires from micro to hyper gravity showed clearly different morphologies. The spherical particles showed regular distribution and nanowires were grown linearly without bundle formation at micro gravity condition. At increased gravity levels, the nanoparticles formed large clusters in a fractal manner and the nanowires showed bundle formation due to a dominant gravity force over the thermal creep.

In Part 2, Al/Al_2O_3 nanowires were deposited on glass and metal substrates by CVD of a single source precursor (SSP) $[^tBuOAlH_2]_2$. Moreover, methods for creating nano/micro structures by direct laser writing (DLW) and laser interference patterning (LIP) and applications related to cell surface interaction are introduced with a wide range of cell types while keeping the identical surface chemical state. The water contact angle on the laser treated surfaces was increased by only altering the surfaces topography without any chemical modification and also static anisotropic wetting behavior on linear periodic patterned surfaces was observed.

In contrast to current literature, substrates were not pre-coated with any organic substances. This is an ideal way to study the direct effect of the topography on cellular behavior. Axons and glial cells of dorsal root ganglia (DRG) neurons grew along the direction of LIP treated Al/Al_2O_3 nanowires while they showed random outgrowth on non-patterned Al/Al_2O_3 nanowires. Especially 2µm periodic patterns showed highest cell alignment rate. Human osteoblast cells (HOB) and normal human dermal fibroblasts (NHDF) showed a controverse behavior on Al/Al_2O_3 nanowires. NHDF exhibited an enhanced elongation and a higher degree of alignment on all DLW patterned substrates. The improvement of the cell adhesion and alignment were most prominent on laser induced channels for both cell types.

Contrast to NHDF, HOB shows better adhesion property on both as-deposited and patterned Al/Al_2O_3 nanowires than NHDF. The higher degree of cell alignment was shown on patterned substrates at period of 50 μm. Nevertheless HOB did not well spread on Al/Al_2O_3 nanowires, they showed similar cell density comparable to the result on smooth surfaces. Since this experiment shows early stage of cell surface interaction, further investigation is needed. Regardless of general behavior of each cell, DLW induced channel lead cell guidance on the channels while LIP treated surfaces affected mostly neuronal fibers and glial cells. These results demonstrate that the topography effect on the cell guidance and the cell adhesion is independent from the surface chemistry. Cell adhesion, orientation and migration were strongly influenced not only by surface topographies in the micrometer and nanometer range but also cell type dependent. It can be suggested that multiscale texturing of surfaces will provide predominant impact on the growth and adhesion of cells on surfaces for implants application or other medical devices.

References

1. Wagner, R. S.; Ellis, W. C. *Applied Physics Letters* **1964,** 4, (5), 89-90.
2. Dick, K. A.; Deppert, K.; Larsson, M. W.; Martensson, T.; Seifert, W.; Wallenberg, L. R.; Samuelson, L. *Nat Mater* **2004,** 3, (6), 380-384.
3. Fan, Z.; Lu, J. G. *Journal of Nanoscience and Nanotechnology* **2005,** 5, (10), 1561-1573.
4. Morales, A. M.; Lieber, C. M. *Science* **1998,** 279, (5348), 208-211.
5. Mohammad, S. N. *Journal of Applied Physics* **2011,** 110, (8), 084310-34.
6. Nyce, T. A.; Rosenberger, F. *Fluid dynamics and lowgravity effects of chemical vapor deposition* NASA-CR-187419, NAS 1.26:187419 NASA: **1990**; p 33.
7. Charter D. Stinespringa; Kolba, C. E.; Annena, K. D. In *Theoretical Studies of Gravitational Effects in Chemical Vapor Deposition*, MRS Fall Meeting, 1986; Doremus, R. H.; Nordine, P. C., Eds. **1986**.
8. Veith, M.; Faber, S.; Hempelmann, R.; Janssen, S.; Prewo, J.; Eckerlebe, H. *Journal of Materials Science* **1996,** 31, (8), 2009-2017.
9. Veith, M.; Sow, E.; Werner, U.; Petersen, C.; Aktas, O. C. *European Journal of Inorganic Chemistry* **2008,** 2008, (33), 5181-5184.
10. Dong, W.; Zhang, T.; Epstein, J.; Cooney, L.; Wang, H.; Li, Y.; Jiang, Y.-B.; Cogbill, A.; Varadan, V.; Tian, Z. R. *Chemistry of Materials* **2007,** 19, (18), 4454-4459.
11. Kim, W.; Ng, J. K.; Kunitake, M. E.; Conklin, B. R.; Yang, P. *Journal of the American Chemical Society* **2007,** 129, (23), 7228-7229.
12. Ellingsen, J. E.; Lyngstadaas, S. P., *Bio-Implant Interface: Improving Biomaterials and Tissue Reactions*. Taylor & Francis: **2003**.
13. Khang, D.; Lu, J.; Yao, C.; Haberstroh, K. M.; Webster, T. J. *Biomaterials* **2008,** 29, (8), 970-983.
14. Deng, F.; Zhang, W.; Zhang, P.; Liu, C.; Ling, J. *Materials Science and Engineering: C* **2010,** 30, (1), 141-147.
15. Gittens, R. A.; Olivares-Navarrete, R.; McLachlan, T.; Cai, Y.; Hyzy, S. L.; Schneider, J. M.; Schwartz, Z.; Sandhage, K. H.; Boyan, B. D. *Biomaterials* **2012,** 33, (35), 8986-8994.
16. Choi, C.-H.; Hagvall, S. H.; Wu, B. M.; Dunn, J. C. Y.; Beygui, R. E.; Kim, C.-J. *Biomaterials* **2007,** 28, (9), 1672-1679.

17. Carlos Nelson, E., Factors Affecting the Success of Dental Implants. In *Implant Dentistry - A Rapidly Evolving Practice*, Turkyilmaz, I., Ed. InTech: **2011**; pp 319-364.
18. Curtis, A.; Wilkinson, C. *Biomaterials* **1997,** 18, (24), 1573-1583.
19. Park, J. K.; Kim, Y.-J.; Yeom, J.; Jeon, J. H.; Yi, G.-C.; Je, J. H.; Hahn, S. K. *Advanced Materials* **2010,** 22, (43), 4857-4861.
20. Spatz, J. P.; Geiger, B. *Methods in Cell Biology* **2007,** 83, 89-111.
21. Balandin, V. Y.; Aleksandrov, L. N.; Dvurechenskii, A. V.; Kulyasova, O. A. *physica status solidi (a)* **1994,** 142, (1), 99-105.
22. Nebel, C. E.; Christiansen, S.; Strunk, H. P.; Dahlheimer, B.; Karrer, U.; Stutzmann, M. *physica status solidi (a)* **1998,** 166, (2), 667-674.
23. Rodriguez, A.; Olaizola, S. M.; Ayerdi, I., *Laser Interference Lithography for Micro- And Nano-Fabrication*. VDM Publishing: **2011**.
24. Petersen, C. Mikro- und nanostrukturierte Schichten mittels Gasphasenabscheidung von $[H_2AlO^tBu]_2$ für den Einsatz in der Nanobiotechnologie. Saarländische Universitäts- und Landesbibliothek, Saarbrücken, **2007**.
25. Veith, M.; Petersen, C.; Aktas, O. C.; Metzger, W.; Oberringer, M.; Pohlemann, T.; Müller, M.; Gerbes, S. *Materials Letters* **2008,** 62, (23), 3842-3845.
26. Aktas, O. C. Functional applications of Al/Al_2O_3 nanowires : laser assisted alpha Al_2O_3 synthesis and fabrication of micro-/nanostructured surfaces for cell compatibility studies. PhD, Saarländische Universitäts- und Landesbibliothek, Saarbrücken, **2009**.
27. Veith, M.; Aktas, O. C.; Metzger, W.; Sossong, D.; Wazir, H. U.; Grobelsek, I.; Pütz, N.; Wennemuth, G.; Pohlemann, T.; Oberringer, M. *Biofabrication* **2010,** 2, (3), 035001-10.
28. Veith, M.; Aktas, O. C.; Lee, J.; Miró, M. M.; Akkan, C. K., Biphasic Nano-Materials and Applications in Life Sciences: 1D Al/Al_2O_3 Nanostructures for Improved Neuron Cell Culturing. In *Nanostructured Materials and Systems*, John Wiley & Sons, Inc.: **2010**; pp 117-121.
29. Aktas, O. C.; Sander, M.; Miró, M. M.; Lee, J.; Akkan, C. K.; Smail, H.; Ott, A.; Veith, M. *Applied Surface Science* **2011,** 257, (8), 3489-3494.
30. Aktas, C.; Haidar, A.; Miró, M. M.; Dörrschuck, E.; Lee, J.; Veith, M.; Khaliq, H. A. *Advanced Materials Research* **2011,** 324, 105-108.

31. Aktas, C.; Dörrschuck, E.; Schuh, C.; Miró, M. M.; Lee, J.; Pütz, N.; Wennemuth, G.; Metzger, W.; Oberringer, M.; Veith, M.; Abdul-Khaliq, H. *Materials Science and Engineering: C* **2012,** 32, (5), 1017-1024.

32. Veith, M.; Lee, J.; Miro, M. M.; Akkan, C. K.; Dufloux, C.; Aktas, O. C. *Chemical Society Reviews* **2012,** 41, (15), 5117-5130.

33. Biela, S. A.; Su, Y.; Spatz, J. P.; Kemkemer, R. *Acta Biomaterialia* **2009,** 5, (7), 2460-2466.

34. Alford, J. M.; Mason, G. R.; Feikema, D. A. *Review of Scientific Instruments* **2006,** 77, (7), 074101-11.

35. Jensen, K. F.; Einset, E. O.; Fotiadis, D. I. *Annual Review of Fluid Mechanics* **1991,** 23, (1), 197-232.

36. Wang, Z. M., *One-Dimensional Nanostructures*. Springer New York: 2008.

37. Xia, Y.; Yang, P.; Sun, Y.; Wu, Y.; Mayers, B.; Gates, B.; Yin, Y.; Kim, F.; Yan, H. *Advanced Materials* **2003,** 15, (5), 353-389.

38. Zhai, T.; Yao, J., *One-Dimensional Nanostructures: Principles and Applications*. Wiley: **2012**.

39. Vasita, R.; Katti, D. S. *International Journal of Nanomedicine* **2006,** 1, (1), 15-30.

40. Pierson, H. O., *Handbook of Chemical Vapor Deposition, 2nd Edition: Principles, Technology and Applications*. Elsevier Science: **1999**.

41. Park, J. H.; Sudarshan, T. S., *Chemical Vapor Deposition*. A S M International: **2001**.

42. Lee, S. T.; Zhang, Y. F.; Wang, N.; Tang, Y. H.; Bello, I.; Lee, C. S.; Chung, Y. W. *Journal of Materials Research* **1999,** 14, (12), 4503-4507.

43. Zhao, Q.; Xu, X.; Zhang, H.; Chen, Y.; Xu, J.; Yu, D. *Applied Physics A* **2004,** 79, (7), 1721-1724.

44. Sow, E. A. Importance of CVD-process parameters for the synthesis of novel Al/Al_2O_3 and Ga/Ga_2O_3 composite nanostructures. Saarländische Universitäts- und Landesbibliothek, Saarbrücken, **2008**.

45. Veith, M. *Journal of the Chemical Society, Dalton Transactions* **2002**, (12), 2405-2412.

46. M. Veith; S. Kneip; S. Faber; E. Fritscher. *Materials science forum* **1998,** 269-272, 303-306.

47. Nöth, H.; Suchy, H. *Zeitschrift für anorganische und allgemeine Chemie* **1968,** 358, (1-2), 44-66.

48. Faber, S. F. K. Herstellung von Metall-Metalloxid-Kompositen über "Metal Organic Chemical Vapour Deposition" unter Verwendung neuartiger Precursoren. Saarländische Universitäts- und Landesbibliothek, Saarbrücken, **1996**.

49. Veith, M.; Andres, K.; Faber, S.; Blin, J.; Zimmer, M.; Wolf, Y.; Schnöckel, H.; Köppe, R.; de Masi, R.; Hüfner, S. *European Journal of Inorganic Chemistry* **2003,** 2003, (24), 4387-4393.

50. Petersen, C.; Lasagni, A.; Holzapfel, C.; Daniel, C.; Mücklich, F.; Veith, M. *Applied Surface Science* **2007,** 253, (19), 8022-8027.

51. Veith, M.; Andres, K.; Petersen, C.; Daniel, C.; Holzapfel, C.; Mücklich, F. *Advanced Engineering Materials* **2005,** 7, (1-2), 27-30.

52. Yao, Y.; Li, F.; Lee, S.-T. *Chemical Physics Letters* **2005,** 406, (4-6), 381-385.

53. Zhang, Y. F.; Tang, Y. H.; Lam, C.; Wang, N.; Lee, C. S.; Bello, I.; Lee, S. T. *Journal of Crystal Growth* **2000,** 212, (1-2), 115-118.

54. Kuan Yew, C.; Yi Ling, C., *Advances of SiOx and Si/SiOx Core-Shell Nanowires*. InTech: **2010**.

55. Pan, Z. W.; Dai, Z. R.; Xu, L.; Lee, S. T.; Wang, Z. L. *The Journal of Physical Chemistry B* **2001,** 105, (13), 2507-2514.

56. Yao, J. H.; Elder, K. R.; Guo, H.; Grant, M. *Physical ReviewB* **1993,** 47, (21), 14110-14125.

57. Qi, W. H.; Wang, M. P. *Materials Chemistry and Physics* **2004,** 88, (2-3), 280-284.

58. Ekinci, Y.; Solak, H. H.; Loffler, J. F. *Journal of Applied Physics* **2008,** 104, (8), 083107-6.

59. German-Aerospace-Center The DLR Parabolic Flights. http://www.dlr.de/Portaldata/28/Resources/dokumente/rw/Broschuere_Parabelflug_hires.pdf

60. Barzic, G. L. Parabolic flight manoeuvres. http://www.dlr.de/en/DesktopDefault.aspx/tabid-734/1210_read-3259/gallery-1/gallery_read-Image.1.526

61. Veith, M.; Kneip, S. J.; Jungmann, A.; Hüfner, S. *Zeitschrift für anorganische und allgemeine Chemie* **1997,** 623, (10), 1507-1517.

62. NASA. A candle flame on earth and onboard the space shuttle. http://microgravity.grc.nasa.gov/combustion/cfm/usml-1_results.htm

63. Zuo, R.; Wang, W. *Journal of Crystal Growth* **2002,** 236, (4), 695-710.

64. Reynolds, O. *Philosophical Transactions of the Royal Society of London* **1879,** 170, 727-845.

65. Rosner, D. E. *Physics of Fluids A: Fluid Dynamics* **1989,** 1, (11), 1761-1763.

66. Sone, Y. *Physics of Fluids A: Fluid Dynamics* **1991,** 3, (5), 997-998.

67. Schwabe, M.; Hou, L.-J.; Zhdanov, S.; Ivlev, A. V.; Thomas, H. M.; Morfill, G. E. *NewJournal of Physics* **2011,** 13, (8), 083034.

68. Gokoglu, S. A. *Chemical vapor deposition modeling: An assessment of current status*; NASA-CR-185301, E-5792, NAS 1.26:185301; NASA: **1991**; p 11.

69. Luo, W.; Su, K.; Li, K.; Liao, G.; Hu, N.; Jia, M. *The Journal of Chemical Physics* **2012,** 136, (23), 234704-6.

70. León, C. A.; Mendoza-Suarez, G.; Drew, R. L. *Journal of Materials Science* **2006,** 41, (16), 5081-5087.

71. Nagai, H.; Nakata, Y.; Tsurue, T.; Suzuki, M.; Okutani, T. *Materials Science and Engineering: A* **1998,** 248, (1-2), 206-211.

72. Hecht, J., *Laser pioneers*. Academic Press: New York, **1992**.

73. Steen, w. M.; Mazumder, J., *Laser Material Processing*. 4 ed.; Springer-Verlag: London, **2010**.

74. Litherland, B. http://www.fabricatingandmetalworking.com/2012/09/tips-for-successful-laser-marking-in-job-shops/

75. Huang, M.; Zhao, F.; Cheng, Y.; Xu, N.; Xu, Z. *Opt. Express* **2008,** 16, (23), 19354-19365.

76. Serafetinides, A. A.; Spyratou, E.; Makropoulou, M. *Proc. SPIE 7747, 16th International School on Quantum Electronics: Laser Physics and Applications* **2011**, 77470V.

77. Pauleau, Y.; European Materials Research, S., *Materials Surface Processing by Directed Energy Techniques*. 1 ed.; Elsevier: **2006**.

78. Hu, H.; Yu, J.; Zhang, L.; Zhang, A.; Li, Y.; Jiang, Y.; Yang, E. *Opt. Express* **2007,** 15, (14), 8931-8937.

79. Arnold, G.; Russer, P.; Petermann, K.; Kressel, H., Modulation of laser diodes, Semiconductor Devices for Optical Communication. In *Topics in Applied Physics*, Springer Berlin / Heidelberg: **1982**; Vol. 39, pp 213-242.

80. Hohlfeld, J.; Wellershoff, S. S.; Güdde, J.; Conrad, U.; Jähnke, V.; Matthias, E. *Chemical Physics* **2000,** 251, (1-3), 237-258.
81. Zhang, Y.; Chen, J. K. *Journal of Applied Physics* **2008,** 104, (5), 054910-9.
82. Gachot; C; Hans; M; Catrin; R; Schmid; U; Mücklich; F, *Tuned Wettability of Material Surfaces for tribological Applications in miniaturized Systems by Laser Interference Metallurgy*. Society of Photo-Optical Instrumentation Engineers: Bellingham, WA, ETATS-UNIS, **2009**; Vol. 7362, p 1-9.
83. Bragg, W. L. *Proceedings of the Cambridge Philosophical Society* **1913,** 17, 43-57.
84. Chris, B. S. a. A. B. a. E. M. *Measurement Science and Technology* **2001,** 12, (11), 1784-1794.
85. Mäder, M.; Höche, T.; Rauschenbach, B. *physica status solidi (a)* **2012,** 209, (11), 2208-2211.
86. Koch, J.; Korte, F.; Bauer, T.; Fallnich, C.; Ostendorf, A.; Chichkov, B. N. *Applied Physics A: Materials Science & Processing* **2005,** 81, (2), 325-328.
87. Kuznetsov, A. I.; Koch, J.; Chichkov, B. N. *Opt. Express* **2009,** 17, (21), 18820-18825.
88. Sefiane, K., Self-induced thermocapillary flows in systems undergoing heat and mass transfer. In *Surface Tension-Driven Flows and Applications* 1ed.; Savino, R., Ed. Research Signpost: Kerala, **2006**; pp 171-201.
89. Dahotre, N. B.; Paital, S. R.; Samant, A. N.; Daniel, C. *Philosophical Transactions of the Royal Society A: Mathematical, Physical and Engineering Sciences* **2010,** 368, (1917), 1863-1889.
90. Singh, S.; Argument, M.; Tsui, Y. Y.; Fedosejevs, R. *Journal of Applied Physics* **2005,** 98, (11), 113520-7.
91. Gachot, C.; Catrin, R.; Lasagni, A.; Schmid, U.; Mücklich, F. *Applied Surface Science* **2009,** 255, (10), 5626-5632.
92. Sugioka, K.; Meunier, M.; Piqueī, A.; Brown, M.; Arnold, C., Fundamentals of Laser-Material Interaction and Application to Multiscale Surface Modification. In *Laser Precision Microfabrication*, Springer Berlin Heidelberg: **2010**; Vol. 135, pp 91-120.
93. Veith, M., Precursorchemistry with Metalalkoxides and their Use for Nano-Scaled Materials. In *Progress in Physical Chemistry*, Oldenbourg Verlag: **2008**; Vol. 2, pp 63-81.

94. Aktas, C.; Lee, J.; Miró, M. M.; Barnoush, A.; Veith, M. *Applied Surface Science* **in press,** http://dx.doi.org/10.1016/j.apsusc.2012.10.123.

95. Rai, A.; Park, K.; Zhou, L.; Zachariah, M. R. *Combustion Theory and Modelling* **2006,** 10, (5), 843-859.

96. Young, T. *Philosophical Transactions of the Royal Society of London* **1805,** 95, 65-87.

97. Aguilar-Santillan, J. *Journal of Nanomaterials* **2008,** 2008, 1-12.

98. Tsekov, R.; Grozev, N. A.; Delcheva, I. V.; Ivanov, I. T.; Balashev, K.; Karakashev, S. I. *The Journal of Physical Chemistry B* **2012,** 116, (44), 13248-13253.

99. Wenzel, R. N. *Industrial & Engineering Chemistry* **1936,** 28, (8), 988-994.

100. Cassie, A. B. D.; Baxter, S. *Transactions of the Faraday Society* **1944,** 40, 546-551.

101. Waugh, D. G.; Lawrence, J. *Optics and Lasers in Engineering* **2010,** 48, (6), 707-715.

102. Kooij, E. S.; Jansen, H. P.; Bliznyuk, O.; Poelsema, B.; Zandvliet, H. J. W. *Colloids and Surfaces A: Physicochemical and Engineering Aspects* **2012,** 413, 328-333.

103. Neuhaus, S.; Spencer, N. D.; Padeste, C. *ACS Applied Materials & Interfaces* **2012,** 4, (1), 123-130.

104. Rahman, M. A.; Jacobi, A. M. *International Journal of Heat and Mass Transfer* **2012,** 55, (5-6), 1596-1605.

105. Hans, M.; Müller, F.; Grandthyll, S.; Hüfner, S.; Mücklich, F. *Applied Surface Science* **2012,** 263, 416-422.

106. Fürstner, R.; Barthlott, W.; Neinhuis, C.; Walzel, P. *Langmuir* **2005,** 21, (3), 956-961.

107. Gao, L.; McCarthy, T. J. *Journal of the American Chemical Society* **2006,** 128, (28), 9052-9053.

108. Scheen, G.; Ziouche, K.; Bougrioua, Z.; Godts, P.; Leclercq, D.; Lasri, T. *Langmuir* **2011,** 27, (10), 6490-6495.

109. Mäder, M.; Perlt, S.; Höche, T.; Hilmer, H.; Grundmann, M.; Rauschenbach, B. *Nanotechnology* **2010,** 21, (17), 175304-5.

110. Loewen, E. G.; Popov, E., *Diffraction Gratings and Applications*. CRC press, Taylor & Francis: **1997**.

111. Bhushan, B. *Beilstein Journal of Nanotechnology* **2011,** 2, 66-84.

112. Yang, Y.-L.; Hsu, C.-C.; Chang, T.-L.; Kuo, L.-S.; Chen, P.-H. *Applied Surface Science* **2010,** 256, (11), 3683-3687.
113. Wagner, C. D.; Muilenberg, G. E., *Handbook of x-ray photoelectron spectroscopy: a reference book of standard data for use in x-ray photoelectron spectroscopy*. Physical Electronics Division, Perkin-Elmer Corp.: **1979**.
114. Anselme, K.; Ponche, A.; Bigerelle, M. *Proceedings of the Institution of Mechanical Engineers, Part H: Journal of Engineering in Medicine* **2010,** 224, (12), 1487-1507.
115. Flemming, R. G.; Murphy, C. J.; Abrams, G. A.; Goodman, S. L.; Nealey, P. F. *Biomaterials* **1999,** 20, (6), 573-588.
116. Bettinger, C. J.; Langer, R.; Borenstein, J. T. *Angewandte Chemie International Edition* **2009,** 48, (30), 5406-5415.
117. Thompson, D.; Buettner, H. *Annals of Biomedical Engineering* **2006,** 34, (1), 161-168.
118. Biran, R.; Noble, M. D.; Tresco, P. A. *Experimental Neurology* **2003,** 184, (1), 141-152.
119. Kim, Y.-t.; Haftel, V. K.; Kumar, S.; Bellamkonda, R. V. *Biomaterials* **2008,** 29, (21), 3117-3127.
120. Vetter, I.; Pujic, Z.; Goodhill, G. J. *Journal of Neurotrauma* **2010,** 27, (8), 1379-1386.
121. Kofron, C.; Liu, Y.-T.; López-Fagundo, C.; Mitchel, J.; Hoffman-Kim, D. *Annals of Biomedical Engineering* **2010,** 38, (6), 2210-2225.
122. Götz, M.; Hartfuss, E.; Malatesta, P. *Brain Research Bulletin* **2002,** 57, (6), 777-788.
123. Leclair, A. M.; Ferguson, S. S. G.; Lagugné-Labarthet, F. *Biomaterials* **2011,** 32, (5), 1351-1360.
124. Johansson, F.; Carlberg, P.; Danielsen, N.; Montelius, L.; Kanje, M. *Biomaterials* **2006,** 27, (8), 1251-1258.
125. Malik, M. A.; Puleo, D. A.; Bizios, R.; Doremus, R. H. *Biomaterials* **1992,** 13, (2), 123-128.
126. Marchi, J.; Delfino, C. S.; Bressiani, J. C.; Bressiani, A. H. A.; Marques, M. M. *International Journal of Applied Ceramic Technology* **2010,** 7, (2), 139-147.
127. Fujita, S.; Ohshima, M.; Iwata, H. *Journal of The Royal Society Interface* **2009,** 6, (3), 269-277.

128. Freitas, R. A., *Nanomedicine*. Landes Bioscience: **1999**.

List of figures

PART 1

PART 2

List of tables

PART 2